Application-oriented optimization of robot elastostatic calibration : implementation on hexapod positioning systems

Vinayak Jagannathrao Kalas

THÈSE POUR OBTENIR LE GRADE DE DOCTEUR DE L'UNIVERSITE DE MONTPELLIER

En Systèmes Automatiques et Micro-électroniques

École doctorale : Information, Structures, Systèmes

Unité de recherche : LIRMM

Application-oriented optimization of robot elastostatic calibration: implementation on hexapod positioning systems

Présentée par Vinayak Jagannathrao KALAS

Le 18 Septembre 2020

Sous la direction de François PIERROT

Devant le jury composé de

Stéphane CARO	Directeur de Recherche	LS2N, Nantes, France	Rapporteur
Pierre RENAUD	Professeur	ICube, Strasbourg, France	Rapporteur
Gabriel ABBA	Professeur	LCFC, Metz, France	Président du jury
François PIERROT	Directeur de Recherche	LIRMM, Montpellier, France	Directeur de thèse
Olivier COMPANY	Maître de Conférences	LIRMM, Montpellier, France	Co-encadrant
Sébastien KRUT	Chargé de Recherche	LIRMM, Montpellier, France	Co-encadrant
Alain VISSIÈRE	Ingénieur de Recherche	LCM (LNE Cnam), Paris, France	Co-encadrant
Thierry ROUX	Directeur Technique	Symétrie, Nîmes, France	Invité

UNIVERSITÉ DE MONTPELLIER

Contents

List of Figures

List of Tables

List of Symbols

η	Velocity vector of the end-effector/platform
τ	Vector containing forces along actuators of a robot when a force/moment F is applied at the end-effector/platform
μ_i	Singular values of $\widetilde{A_M}$
μ_{min}	Minimum singular value of $\widetilde{\widetilde{A_M}}$
μ_{max}	Maximum singular value of $\widetilde{\widetilde{A_M}}$
${}^{Du}\sigma_{\widetilde{\varepsilon}_{\Delta X_M}}$	Standard deviation of elements of ${}^{Du}\widetilde{\varepsilon}_{\Delta X_M}$
${}^{Du}\varepsilon_{\Delta X_M}$	Vector containing the errors in measured deflections (ΔX_M) due to uncertainty of the measurement system
${}^{FE}\varepsilon_{\Delta X_M}$	Vector containing the errors in measured deflections (ΔX_M) due to $\varepsilon_{\Delta F_M}$
${}^{Du}\varepsilon_c$	Errors in estimated stiffness parameters due to errors in measurements deflections ${}^{Du}\varepsilon_{\Delta X_M}$
${}^{FE}\varepsilon_c$	Errors in estimated stiffness parameters due to errors in applied forces/-moments during stiffness identification $\varepsilon_{\Delta F_M}$
${}^{Du}\widetilde{\varepsilon}_{\Delta X_M}$	${}^{Du}\varepsilon_{\Delta X_M}$ scaled using G
${}^{Du}\varepsilon_{\Delta X_C}$	Component of error in predicted deflection $\widehat{\Delta X_C}$ as a result of ${}^{Du}\varepsilon_c$

${}^{FE}\mathcal{E}_{\Delta X_C}$	Component of error in predicted deflection $\widehat{\Delta X_C}$ as a result of ${}^{FE}\mathcal{E}_c$
$\mathcal{E}_{\Delta F_M}$	Errors in applied forces/moments during stiffness identification
${}^{DU}\mathcal{E}_{X_A}$	Errors in pose attained after compensation as a consequence of errors in measured deflections during stiffness identification
${}^{FE}\mathcal{E}_{X_A}$	Errors in pose attained after compensation as a consequence of errors in forces/moments applied during stiffness identification
${}^{FE,t}\mathcal{E}_{X_A}$	Translational components of ${}^{FE}\mathcal{E}_{X_A}$
${}^{FE,r}\mathcal{E}_{X_A}$	Rotational components of ${}^{FE}\mathcal{E}_{X_A}$
${}^{DU}\mathcal{E}_{X_C}$	Component of error in predicted *command pose* ($\widehat{X_C}$) as a consequence of errors in measured deflections during stiffness identification
${}^{FE}\mathcal{E}_{X_C}$	Component of error in predicted *command pose* ($\widehat{X_C}$) as a consequence of errors in forces/moments applied during stiffness identification
${}^{DU,t}\mathcal{E}_{X_A}$	Vector containing the translational components of ${}^{DU}\mathcal{E}_{X_A}$
${}^{DU,r}\mathcal{E}_{X_A}$	Vector containing the rotational components of ${}^{DU}\mathcal{E}_{X_A}$
A	Also called *observation matrix*, it is a function of ΔF, J & $\check{J}$ and relates ΔX & c
A_D	Matrix A formulated using the set of poses (X_D) and forces/moments (ΔF_D) at which best positioning performance is desired
${}^{r}A_D$	Rows of A_D corresponding to the rotational elements of ΔX_D
${}^{t}A_D$	Rows of A_D corresponding to the translational elements of ΔX_D
A_M	Observation matrix (A) corresponding to ΔF_M and X_M
$\widetilde{A_M}$	Matrix A_M scaled using matrices G and H
${}^{as}A_M$	Matrix A_M formulated using pose X_M and the assumed differential force vector applied at the platform (${}^{as}\Delta F_M$) during stiffness identification
c	Vector containing inverses of k_i
$\check{c}$	Estimated stiffness parameters that are corrupted by ${}^{DU}\mathcal{E}_c$
$\widehat{c}$	Estimated stiffness parameters that are corrupted by ${}^{DU}\mathcal{E}_c$ & ${}^{FE}\mathcal{E}_c$
D	Matrix which is function of J, $\check{J}$ and K
${}^{ap}D$	Matrix which is function of J, $\check{J}$ and ${}^{ap}K$
F^{in}	Initial load vector applied at the end-effector/platform of a robot during stiffness identification

${}^{as}F^{in}$	Initial load vector assumed to have been applied at the end-effector/platform of a robot during stiffness identification
${}^{ac}F^{in}$	Initial load vector actually applied at the end-effector/platform of a robot during stiffness identification
F^{fi}	Final load vector applied at the end-effector/platform of a robot during stiffness identification
${}^{as}F^{fi}$	Final load vector assumed to have been applied at the end-effector/platform of a robot during stiffness identification
${}^{ac}F^{fi}$	Final load vector actually applied at the end-effector/platform of a robot during stiffness identification
ΔF	Difference between the initial and final load vectors applied at the end-effector/platform of the robot during stiffness identification
ΔF_D	Forces/moments with which best positioning performance is desired at X_D
ΔF_M	Difference between the initial and final load vectors applied at the end-effector/platform of the robot during stiffness identification with the end-effector/platform at pose X_M
${}^{as}\Delta F_M$	Difference between the initial and final load vectors assumed to have been applied at the end-effector/platform of the robot during stiffness identification
${}^{ac}\Delta F_M$	Difference between the initial and final load vectors actually applied at the end-effector/platform of the robot during stiffness identification
G	Task variable scaling matrix
G_U	Task variable scaling matrix when elements of ${}^{DU}\mathcal{E}_{\Delta X_M}$ are independent but don't have identical distribution (different standard deviations)
G_C	Task variable scaling matrix when elements of ${}^{DU}\mathcal{E}_{\Delta X_M}$ are not independent
H	Parameter scaling matrix
J	Jacobian matrix
$\check{J}$	Matrix relating Δq and ΔX

k_i	Stiffness along i^{th} actuator of a robot
K	A diagonal matrix containing the stiffness along robot's actuators (k_i) along its diagonal
${}^{ap}K$	A diagonal matrix containing the approximate values of stiffnesses along robot's actuators along its diagonal
K_C	Cartesian stiffness matrix
q	Vector containing actuator positions/lengths
Δq	Vector containing differentials of actuator positions/lengths
U	Matrix containing scaling factors that scale ${}^{Du}\sigma^2_{\widetilde{\varepsilon}_{\Delta X_M}}$ to respective elements of $Cov({}^{Du}\varepsilon_{X_A})$
X^{in}	Pose vector of a robot's end-effector/platform when the load vector applied on it is F^{in}
X^{fi}	Pose vector of a robot's end-effector/platform when the load vector applied on it is F^{fi}
X_A	Pose attained by a robot after elastostatic error compensation when there are no errors in identified parameters
$\widehat{X_A}$	Pose attained by a robot after elastostatic error compensation when there are errors in identified parameters
X_C	Pose vector that is entered into the controller of a robot that doesn't have the compliance error model embedded in it (*command pose*)
$\widehat{X_C}$	Predicted *command pose* with error
X_D	Pose at which best positioning is desired
X_M	Pose vector of a robot's end-effector/platform at a pose where stiffness identification is performed
ΔX	Deflection of a robot's end-effector/platform due to a change in load ΔF on it
ΔX_C	Deflection at pose X_C due to a load ΔF_D
$\widehat{\Delta X_C}$	Predicted deflection with error at pose $\widehat{X_C}$ and load F_D
ΔX_M	Deflection measured at pose X_M under the influence of force/moment applied ΔF_M

$\widehat{\Delta X_M}$	Deflections measured during stiffness identification and corrupted by ${}^{DU}\varepsilon_{\Delta X_M}$ & ${}^{FE}\varepsilon_{\Delta X_M}$
${}^{ac}\Delta X_C$	Actual deflection of the end-effector/platform at the pose $\widehat{X_C}$ as a result of actual stiffness parameters (c) and applied load ΔF_D
ΔX_D	Deflection at pose X_D due to an applied load ΔF_D
$\Delta X_D{}^t$	Vector containing translational elements of ΔX_D
$\Delta X_D{}^r$	Vector containing rotational elements of ΔX_D
Z	Matrix containing scaling factors that scale $\varepsilon_{\Delta F_M}$ to ${}^{FE}\varepsilon_{X_A}$
${}^tZ$	Rows of Z corresponding to ${}^{FE,t}\varepsilon_{X_A}$
${}^rZ$	Rows of Z corresponding to ${}^{FE,r}\varepsilon_{X_A}$

Acknowledgements

The work presented in this thesis would not have been possible without the support of many people, whom I would like to thank here.

Firstly, I would like to express my gratitude to François Pierrot, my thesis director, for all his help during the course of this research. More importantly, he deserves special praise for inspiring engineers and researchers like me to strive for excellent research.

My sincere thanks also goes to Sébastien Krut, firstly, for giving me the opportunity to work on this project and secondly, for encouraging and aptly advising me to perform high-quality research. His valuable advices have shaped the course of this work to a great extent.

I would like to express my deepest gratitude to Olivier Company for being a wonderful guide and for being there whenever I needed him the most. His ability to have a good helicopter view of the problem at hand and his vast knowledge in robotics have been instrumental in shaping the course of this work.

I would also like to thank Alain Vissière for his help throughout the course of this research. I thank him for introducing me to the work of POSILAB, for his active involvement in this work and for helping me in the process of writing papers and this thesis.

I would like to thank Thierry Roux, Pierre Noiré and Olivier Lapierre from Symétrie for their continuous support in the past three years. They have been incredibly helpful and their profound knowledge of hexapods has been instrumental in sculpting this work.

A special thanks goes to other colleagues from Symétrie who have been very helpful for this research with their knowledge about hexapods and by doing everything necessary to ensure that I could have ample "play time" with their hexapods.

I would also like to thank the reporters of this thesis, Stéphane Caro and Pierre Renaud, for taking time to read this thesis despite their extremely busy schedules.

I would like to thank all (past and present) colleagues from LIRMM for the stimulating discussions and for maintaining an exceptional atmosphere for performing research. In particular, Marc Gouttefarde deserves special praise for sharing his knowledge about the world of research.

Lastly, I would like to thank Agence Nationale de la Recherche (ANR) for funding this work.

Vinayak Kalas
Montpellier, April 2020

General introduction

Context

The work presented in this thesis was carried out within the framework of POSILAB project. This project was carried out in a joint laboratory, POSILAB, between an academic laboratory called LIRMM (*Laboratoire d'Informatique, de Robotique et de Microélectronique de Montpellier*) and a private enterprise named Symétrie. LIRMM is a multi-partner multi-disciplinary research institution which conducts research in computer science, microelectronics and robotics. The DEXTER team within LIRMM is involved in the POSILAB project and this team specializes in, among other things, development of robotic manipulators, especially, parallel robots (example: hexapods). Symétrie is an enterprise that specializes in hexapods for precise-positioning and motion applications. This project was funded by French National Research Agency (ANR). The main aim of this project was to find innovative solutions to achieve better positioning performance, than what is currently possible, with high-precision hexapod positioning systems.

Hexapods (see figure 1), commonly known as Gough–Stewart platforms, are parallel robots with six actuated legs. Parallel robots have multiple serial chains connecting the base to the end-effector/platform. In contrast, serial robots have a single chain connecting the base to the end-effector/platform (see Figure 2). The first hexapods were developed

in 1950's and 1960's. Notably, the first known hexapods were developed by V. E. Gough for testing tyres and D. Stewart for flight simulation [Stewart, 1965] (see figure 3). Hence, the name Gough–Stewart platform. Today, they are extensively used for two main class of applications: high-precision 6-DOF positioning (see figure 4) and 6-DOF motion generation (see figure 5). Hexapods are attractive for high-precision positioning applications due to their high stiffness [1] and due to the fact that they are statically determinate or isostatic structures. The advantage of hexapod being statically determinate is that the platform is not susceptible [2] to unwanted internal stresses that deform the platform.

Figure 1: A hexapod

1. This is a general advantage of parallel robots over their serial counterparts.

2. Consider a septapod (hexapod with one extra leg). This robot is statically indeterminate. Assuming that only position control is used, the platform will be subjected to (even if it is minimal) internal stresses. This is because there are more legs constraining the platform than that are absolutely required. Consequently, the constraining legs fight with each other and induce stresses in the hexapod and its platform, unless the legs are machined and controlled extremely precisely. Furthermore, temperature changes can worsen the internal stresses in the structure [Soemers, 2011]. These internal stresses can deform the structure and these are not easily predictable (since static equilibrium equations can't be solved), thereby making them unattractive for high-precision positioning applications.

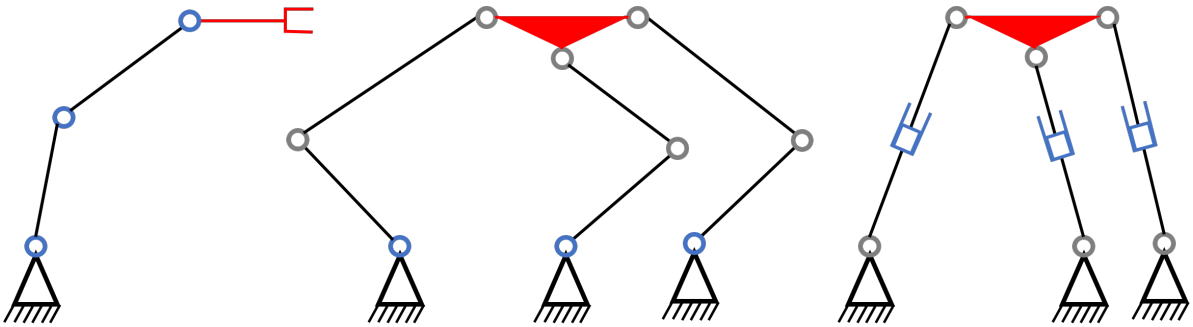

Figure 2: Serial robots (leftmost) connect the base to the end-effector/platform (red) using single chain with all actuators (blue) in series, as opposed to parallel robots (second and third robots)

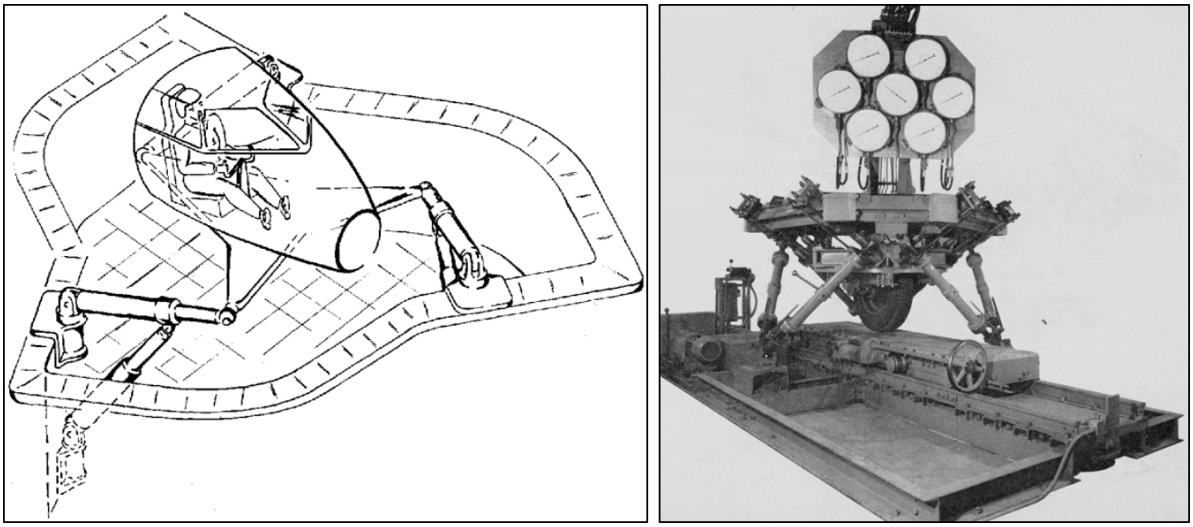

Figure 3: Figures showing the first designs of hexapod proposed by D. Stewart (left) and V. E. Gough (right) [Stewart, 1965]

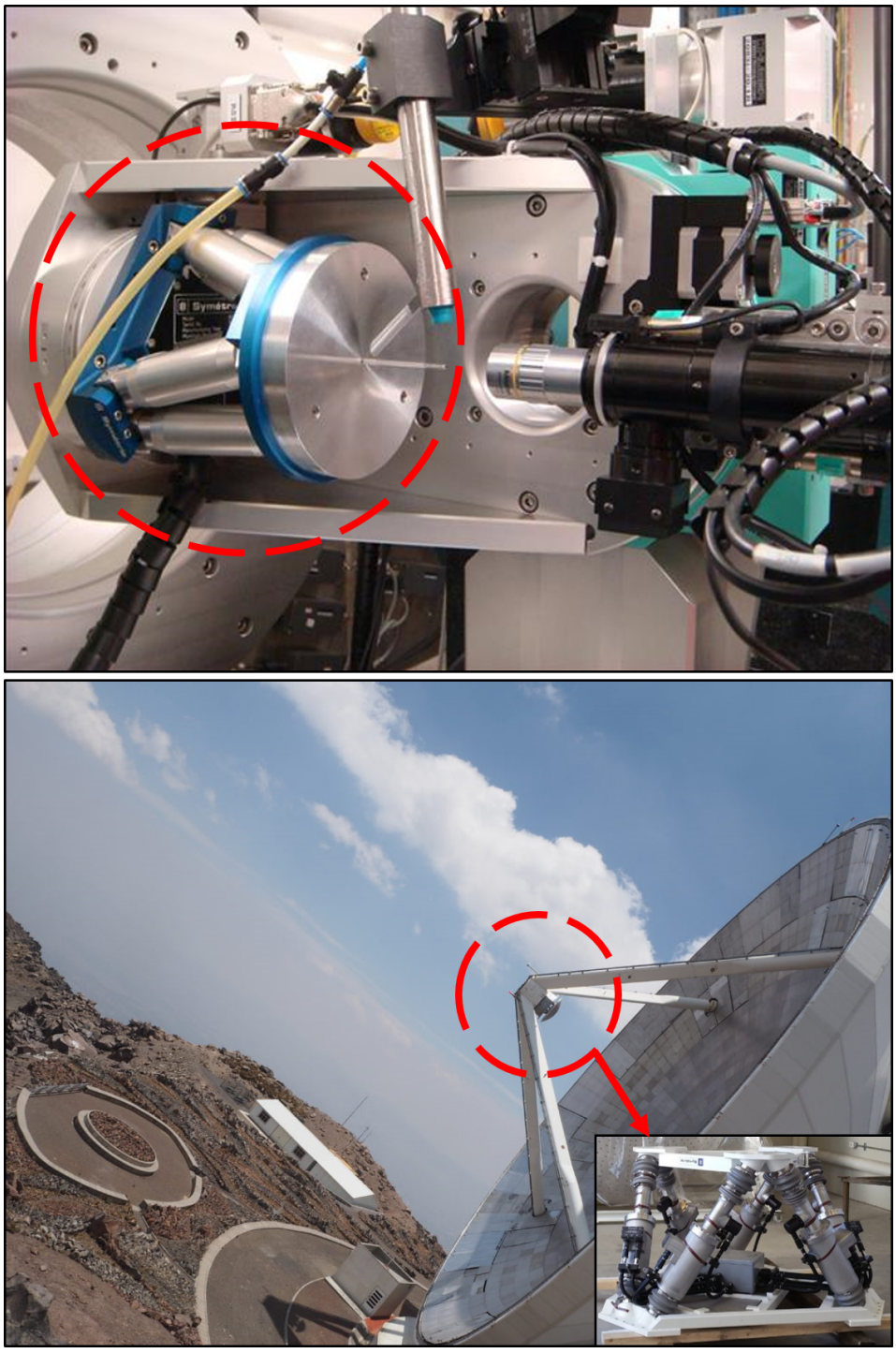

Figure 4: Figures showing hexapods used for high-precision 6-DOF positioning applications such as for positioning samples in synchrotrons [Symétrie, c] (top) and for positioning mirrors in telescopes [Symétrie, e] (bottom)

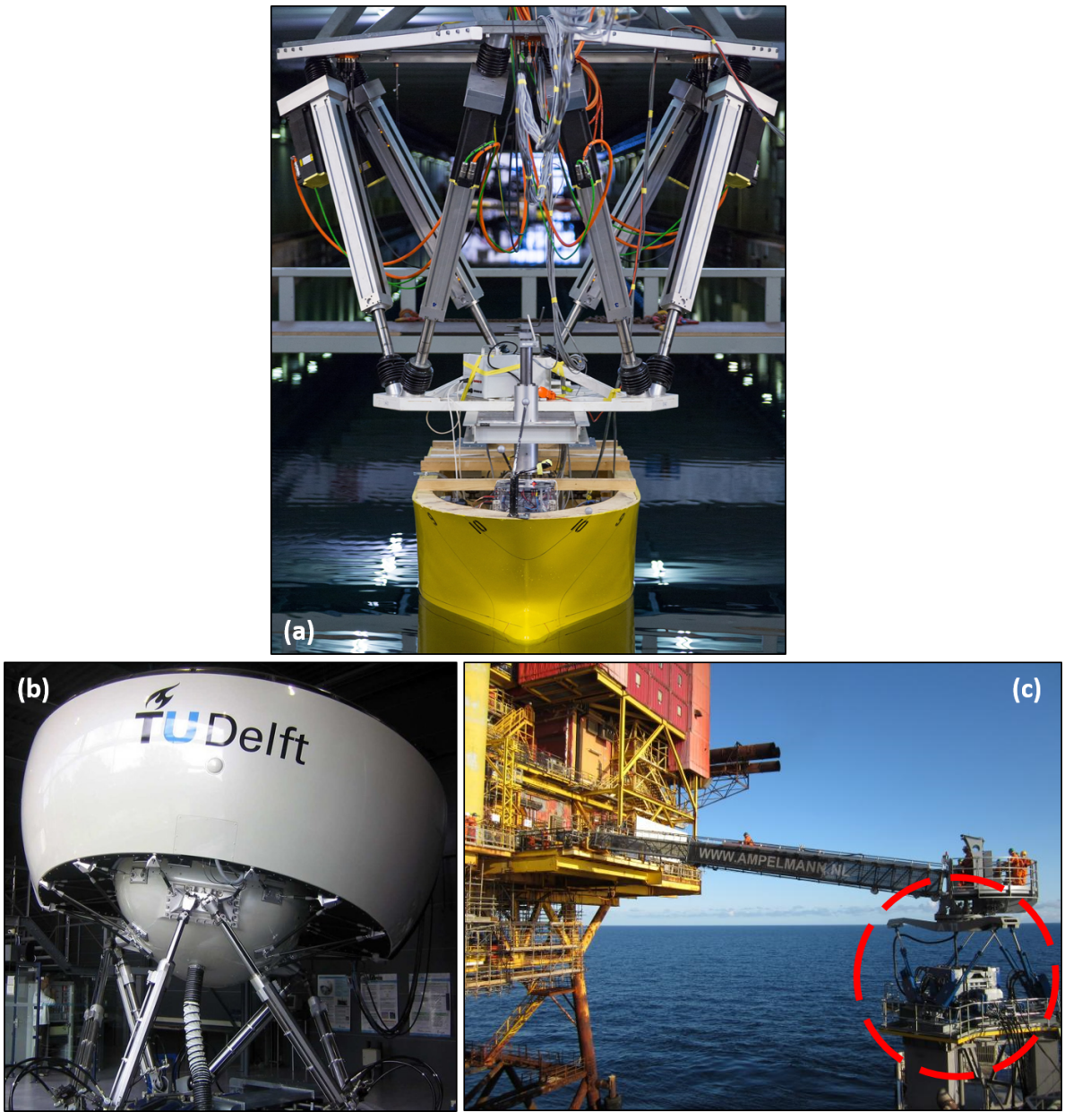

Figure 5: Figures showing hexapods used for 6-DOF motion applications such as for: (a) moving ship models (& other components) in wave basins [Symétrie, b], (b) flight simulation [TUDelft], and (c) offshore platform stabilization [Gangan]

Motivation

A robot's static positioning performance is affected by many factors such as geometric, errors, thermal deflections, friction, compliance of robot's components, etc. Depending on the application at hand and the components used in a robot, some of these factors dominate positioning errors over others. Symétrie's positioning hexapods are designed to achieve high repeatability. Various techniques – such as geometric calibration – are used to ensure high accuracy too (see figure 6 for difference between repeatability and accuracy of positioning). However, as new challenging applications emerge, problems that could be neglected before must be taken into consideration. One such problem is the deflection of the hexapod when a heavy load is placed on the platform. The accuracy of these hexapods deteriorate when heavy payload is mounted on their platforms, as a result of compliance of their components. Consequently, Symétrie was interested in understanding the influence of compliance of hexapod's components on its accuracy when a heavy payload is mounted on its platform. Subsequently, the goal was to improve the accuracy of hexapods with heavy payload mounted on their platforms. This was important because a growing number of their clients have been demanding for positioning with high payload and high accuracy.

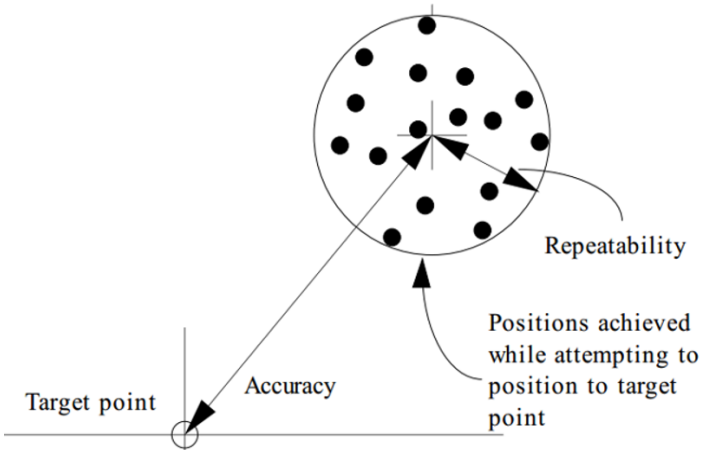

Figure 6: Illustration of repeatability and accuracy of positioning [Slocum, 1992]

Accuracy of loaded robots can be increased in two ways. The robot can be designed

to be more stiff[3] or the errors in positioning due to payload on the platform can be compensated for by prescribing extra displacements in actuators. The former option is not attractive as it is expensive to achieve this and deflections can't be completely eliminated. Robot calibration is a concept that deals with compensating for robot's positioning errors due to various factors. Robot elastostatic calibration [Dumas, 2011; Wu, 2014] deals with compensating for positioning errors of loaded robots due to compliance of their components. The general[4] manner of performing robot elastostatic calibration involves (in the order mentioned): (a) modelling stiffness of the robot using a parametric model, (b) measuring deflections of the robot when known loads are applied, (c) identifying/estimating the parameters of the stiffness model, and (d) compensating for the positioning errors of the loaded robot. It is known that in this elastostatic calibration method, the choice of end-effector/platform poses (position and orientation) and forces/moments used for performing the deflection measurements affects the quality of estimated parameters [Dumas, 2011; Wu, 2014]. This, in turn, influences the quality of compensation. In the literature, best poses and forces/moments were chosen for stiffness identification using criteria which minimized the influence of deflection measurement uncertainty[5] on stiffness identification. Many such criteria exist and they can be broadly classified into the ones that minimize parameter errors and the ones that minimize pose error after compensation, for a given uncertainty of deflection measurement.

For applications concerning many of Symétrie's customers and for many other robotic positioning applications, precise positioning is often required only at some predetermined poses in the workspace, along predetermined axes and with a predetermined payload. It is, therefore, important to have criterion for selecting poses and forces/moments for stiffness identification that can maximize positioning accuracy after compensation under the given conditions. Furthermore, preliminary study[6] revealed that realistic differences between forces/moments actually applied during stiffness identification experiment and those assumed to have been applied can have considerable impact on compensation qual-

3. Using stiffer materials and/or designing a stiffer geometry.

4. Other methods also exist for performing robot elastostatic calibration. However, this method is more common and advantageous due to reasons explained in section 1.1.2.

5. Uncertainty of deflection measurements exists as a consequence of uncertainty of pose measurement instrument used for performing deflection measurements.

6. Presented later in this thesis.

ity. Hence, the criterion for selecting poses and forces/moments for stiffness identification must also minimize the influence of this error on compensation quality.

The criteria present in the literature for selecting best poses and forces/moments for stiffness identification can't ensure best possible positioning performance at predetermined poses, along predetermined axes and with predetermined forces/moments on end-effector/platform. Furthermore, these criteria do not minimize the influence of errors in forces/moments applied during stiffness identification on compensation quality. Hence, new criteria had to be developed to satisfy the requirements stated above.

Thesis goals

In the view of above mentioned requirements, the following goals were defined for this thesis:

- ***Thesis goal 1***: Development of new criterion or set of criteria for selection of poses and forces/moments for stiffness identification which:
  - *Sub-goal 1*: minimize the influence of deflection measurement uncertainty and errors in forces/moments applied during stiffness identification experiment on compensation quality.
  - *Sub-goal 2*: maximize positioning accuracy after compensation at predetermined pose(s), along predetermined axe(s) of end-effector/platform and with predetermined force(s) & moment(s) applied to the end-effector/platform.
- ***Thesis goal 2***: Implementing elastostatic calibration of a high-precision hexapod positioning system and using the developed criterion/criteria for optimizing its stiffness identification.

Thesis outline

To address the above defined goals of this thesis, the contents of this thesis are organized as follows:

Chapter 1 introduces the state of the art of robot elastostatic calibration and its optimization. It presents the concept of robot elastostatic calibration and type of robot elastostatic calibration chosen to accomplish the goals of this thesis. The necessary mathematical background of elastostatic calibration and its optimization is also presented. This chapter concludes with the presentation of existing criteria for stiffness identification optimization, their limitations and subsequent requirements from new criterion/criteria to be developed.

Chapter 2 presents the framework to formulate stiffness identification optimization criterion/criteria that counters the limitations of the existing criteria for the same. The necessary mathematical formulations of the said framework are derived and the ways to use them are discussed.

Chapter 3 is devoted to validation of efficacy of the presented stiffness identification optimization framework using simulated elastostatic calibrations of a bipod. These simulation studies were performed on a bipod to facilitate ease of analysis of results as this mechanism is simple.

Chapter 4 documents the experimental studies on elastostatic calibration of a high-precision positioning hexapod. The presented studies validate the efficacies of elastostatic calibration of hexapods and the stiffness identification optimization framework presented in chapter 2.

Finally, the *conclusions* of this thesis are presented which highlights the main contributions of this thesis and presents some recommendations for future work.

CHAPTER

1 State of the art and background of robot elastostatic calibration and its optimization

Contents

Chapter Abstract

This chapter presents the state of the art of robot elastostatic calibration and its optimization. The concept of robot elastostatic calibration, the need for it and the different types of it are presented first. The elastostatic calibration framework necessary to achieve the aim of this thesis is then presented, followed by the necessary mathematical framework for this. The concept of stiffness identification optimization is presented along with the existing criteria for achieving the same. Finally, limitations of the existing stiffness identification optimization criteria and subsequent requirements from new criteria to be developed are presented.

1.1 Introduction to robot elastostatic calibration

1.1.1 Need for robot elastostatic calibration

The static positioning performance of a robotic manipulator is deteriorated due to a number of factors. Some of the major factors include geometric errors, thermal deflections of robot's components, compliance of robot's components, friction between mating components of the robot, clearance in joints and play/backlash in gears, ball screws, etc. Different factors, from the ones listed, dominate the total positioning error depending on the robot, the control method and the application. In order to achieve good positioning performance, these errors are kept minimal (relative to required positioning accuracy and repeatability) by using high-quality mechanical components. Alternatively or additionally, appropriate compensation techniques are used to minimize or eliminate the influence of these error sources on the robot's positioning performance.

The concept of *robot calibration* deals with compensation for robot's positioning error due to different errors [Roth et al., 1987]. Different types of robot calibrations seek to minimize the influence of different types of errors on the static positioning performance of a robot: geometric calibration [Hayati et al., 1988] to minimize the influence of geometric errors, elastostatic calibration [Gong et al., 2000; Dumas, 2011] to minimize the influence of compliance errors, thermal calibration [Gong et al., 2000] to minimize the influence of thermal errors, and so on.

Robot geometric calibration is a widely studied and applied concept. However, robot elastostatic calibration has only recently garnered serious attention. Robot elastostatic calibration becomes necessary for robots that are used for applications that require high-accuracy positioning in the presence of heavy loads at the end-effector/platform. One application where the need for this has been demonstrated is high-accuracy machining [Dumas, 2011]. In these high-accuracy machining applications, machining forces induce considerable deformations within the robot that reduce the accuracy of the end-effector to unacceptable levels [Wu, 2014]. This in turn affects the quality of the machined product. Similarly, for other high-accuracy positioning applications, positioning accuracy can deteriorate to unacceptable levels when relatively heavy loads are applied on the robot.

In the context of high-precision positioning hexapods, figure 1.1 illustrates the problem of accuracy deterioration due to compliance of robot's components and the required solution. A hexapod which is designed for and is capable of accurate positioning, without heavy load mounted on the platform, will deliver less positioning accuracy when a heavy load is placed on it. This decrement in accuracy increases with increase in applied load. Furthermore, the resulting accuracy deterioration is dependent on the hexapod design, configuration/pose of the robot and the nature & magnitude of applied forces/moments.

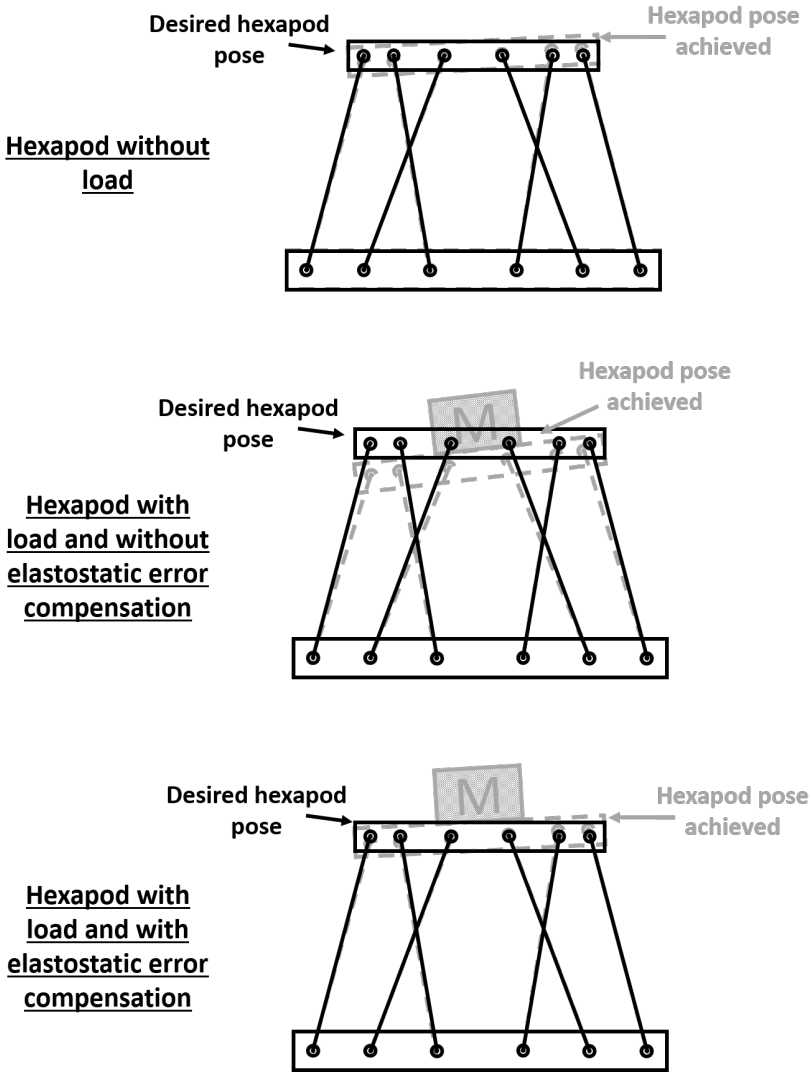

Figure 1.1: Phenomenon of accuracy deterioration of a hexapod positioning system with mounted payload and the required solution

In order to investigate this problem, a preliminary test was performed on a high-precision hexapod positioning system from Symétrie. The repeatability of this hexapod is ± 0.75 μm along translational coordinates and ± 3.25 μrad along rotational coordinates. More details about this product can't be disclosed due to confidentiality reasons. In this test, the deflection of the hexapod's platform due to mounting of load was measured. The hexapod was loaded using a series of weights with the platform in zero pose[1]. These weights were placed in a manner that made sure that the force applied was (approximately) purely along the Z-axis of the platform. The 6-DOF pose of the platform was measured[2] with different (and no) weights placed on the platform. These measurements were in turn used to calculate the 6-DOF deflections of the robot's platform. Figure 1.2 shows the test setup used in this test. The loads applied during this test were below the maximum allowable payload of this system. Figure 1.3 shows the results of this test. As can be seen from these results, mounted weights cause considerable deflections (relative to the repeatability) of the hexapod's platform. For example, a mass of 26.5 kg ($\approx$260 N) mounted on the platform causes deflections of upto 11 μm in translations and 21 μrad in rotations. These deflections will also degrade the accuracy of this hexapod by the same amounts. Hence, there is considerable room for improvement of this hexapod's positioning accuracy when payload is mounted on its platform.

1. For Symétrie's hexapods, pose (position & orientation) of the platform is defined using a coordinate frame fixed at the center of the platform (platform frame). The pose of the platform with the hexapod in any arbitrary configuration is defined with respect to the platform frame that exists when all of the hexapod's legs are locked at the center of their strokes. Zero pose is the pose of the platform in which all the six pose parameters (defining the 3 translations & 3 rotations) are zero. All of the hexapod's legs are locked at the center of their strokes in zero pose.
2. Pose measurement performed using method described in Appendix A.

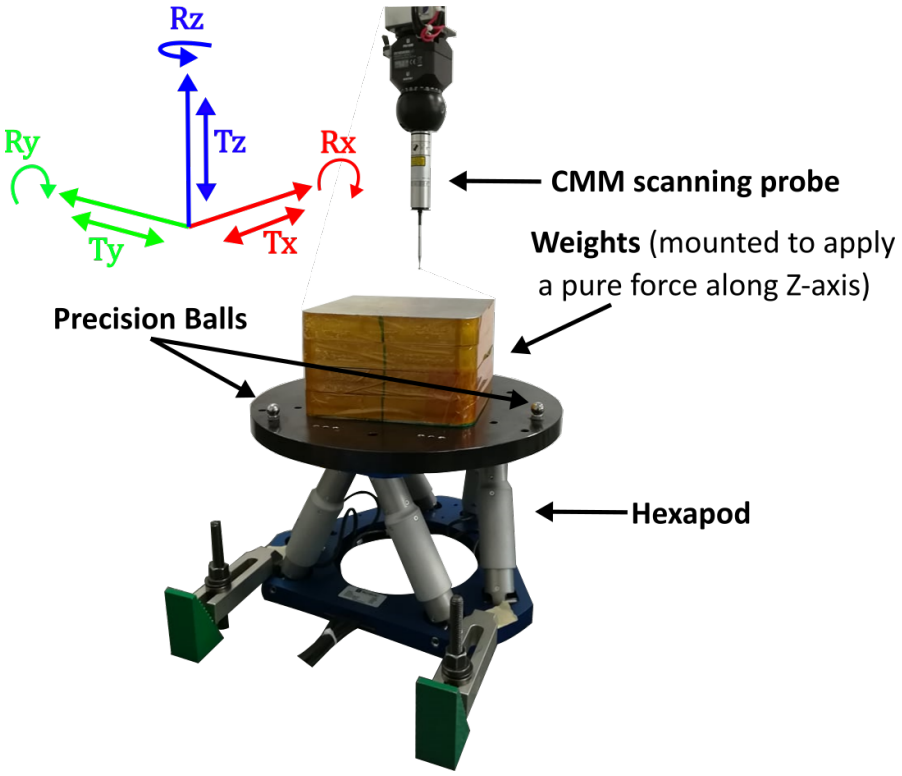

Figure 1.2: Setup to measure the deflection of the platform of a high-precision hexapod positioning system due to load mounted on it's platform

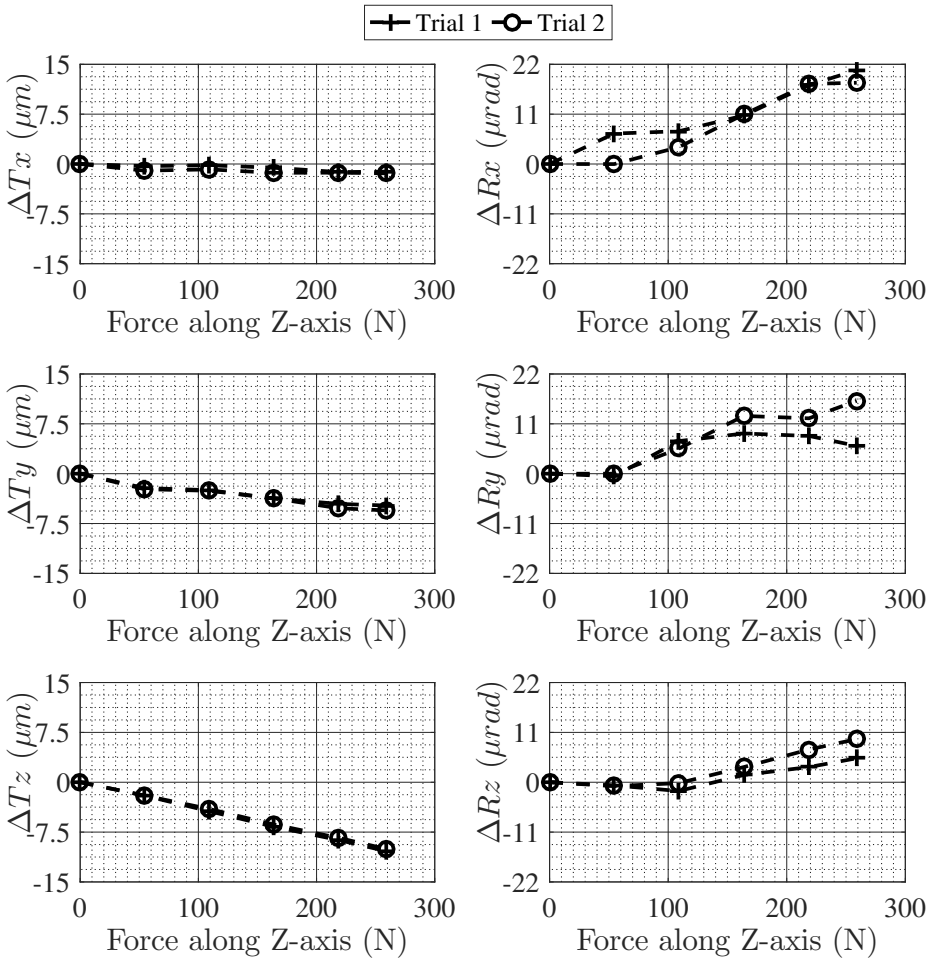

Figure 1.3: Measured 6-DOF deflections of the platform of the hexapod under study (see figure 1.2) due to applied loads

1.1.2 Different approaches to robot elastostatic calibration

Figure 1.4 shows the classification of approaches to robot elastostatic calibration. As also mentioned earlier, robot elastostatic calibration is one of the many different types of calibrations that can be performed on a robot. At a broader level, elastostatic calibration approaches can be classified into: (a) *parametric elastostatic calibration* , and (b) *non-parametric elastostatic calibration*. This classification nomenclature (parametric and non-parametric) also exists for robot geometric calibration [Chen-Gang et al., 2014]. Following this classification, parametric elastostatic calibration can be further classified into two types: one that employs *experimental parameter identification* and the other that employs *analytical parameter identification*.

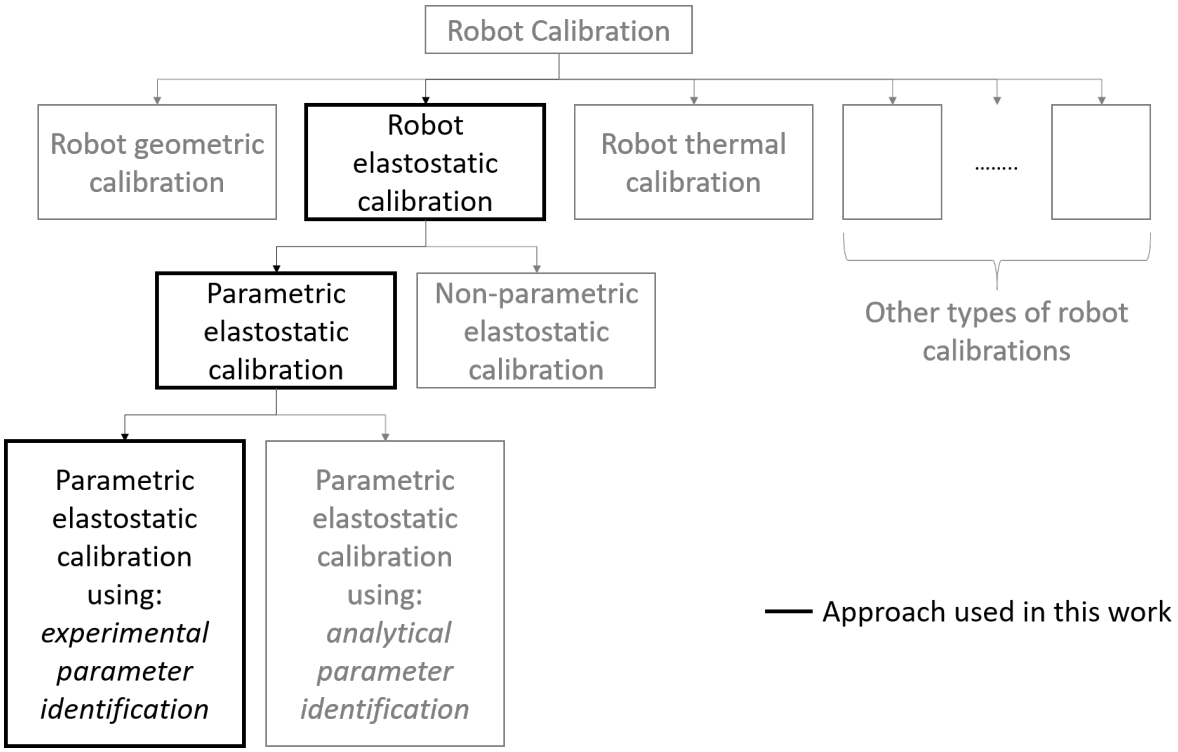

Figure 1.4: Classification of robot calibration approaches

The distinction between parametric and non-parametric elastostatic calibration approaches is based on the use of parametric model (or not thereof) to predict and correct the pose error due to compliance of a loaded robot. The parametric model referred to

here relates the pose error of the end-effector/platform to the load applied on it, for any given configuration of the robot, either by means of: (a) stiffness parameters [Zhou and Kang, 2015; Dumas, 2011; Wu, 2014; Kammerer and Perrot, 2012; Khalil and Besnard, 2002; Lightcap et al., 2008; Abele et al., 2007; Gong et al., 2000], or (b) geometric parameters dependent on load and robot's configuration [Meggiolaro et al., 2005; Chalfoun et al., 2007]. Therefore, in the parametric approach to elastostatic calibration, a parametric model is used to predict and correct the pose error due to applied load at the end-effector/platform. Non-parametric elastostatic calibration, on the other hand, doesn't use parametric relationships to compensate for pose error due to applied load. This could be achieved using: (a) measured relationships between the platform pose errors and joint variables when the platform is subjected to load(s) [3] [Shamma and Whitney, 1987], or (b) compensation of pose error by measuring it in real-time. Most of the work present in the literature on robot elastostatic calibration is based on the parametric approach. However, non-parametric approaches to robot elastostatic calibration have found their use in some companies.

Non-parametric elastostatic calibrations have been used by some companies to improve the accuracy of their loaded robots because they can be very easy to implement when: (a) the requirements are not very challenging (for example: high accuracy at some selected poses), or (b) budget allows use of expensive sensors. When an application doesn't allow this leniency, non-parametric elastostatic calibration isn't a very attractive option. This is because the mentioned non-parametric elastostatic calibration approaches (listed before) have disadvantages such as: (a) large number of measurements required to achieve compensation in rather small workspace volume, or (b) necessity of extra sensors. The parametric approach, on the other hand, do not pose these problems. The identified parameters can be used to predict and correct pose error of a loaded robot throughout its workspace without any extra sensors. Within the parametric approach, using stiffness parameter model is better than using load and configuration dependent geometric parameters. This is because the identification of load and configuration dependent geometric parameters requires large number of measurements as compared to the ones required for identification of stiffness parameters.

3. These relationships can be measured at discrete pose(s) in the workspace with certain load(s) applied to the platform, in order to compensate at those pose(s) and load(s). Furthermore, polynomial interpolation can be used to predict these relationships for positioning at different poses and using different loads.

Efficient parametric elastostatic calibration needs the chosen parametric (stiffness) model to make accurate predictions. This requires accurate estimation of stiffness parameters. Stiffness parameter estimation has been approached in the literature along the following directions: (a) experimental estimation of stiffness model parameters [Dumas, 2011; Wu, 2014; Abele et al., 2007; Carbone and Ceccarelli, 2006; Alici and Shirinzadeh, 2005; Bonnemains et al., 2009; Zhou and Kang, 2015; Chalfoun et al., 2007; Meggiolaro et al., 2005; Kammerer and Perrot, 2012; Lightcap et al., 2008; Ruggeri et al., 2009; Gong et al., 2000], and (b) analytical estimation of stiffness model parameters [Majou et al., 2007; Clinton et al., 1997; Li et al., 2002; Deblaise et al., 2006; Chen and Lan, 2008; Rebeck and Zhang, 1999; Klimchik et al., 2013]. Analytical estimation of stiffness parameters, as the name suggests, relies on analytically estimating the stiffness of components of the robot (such as using FEM). These analytically estimated stiffness of components are then used to estimate the stiffness parameters of the chosen stiffness model. In contrast, experimental estimation of stiffness parameters involves their estimation by means of measurements carried out in suitably designed experiments.

Analytical estimation of stiffness parameters can be more computationally expensive, more time consuming and more complicated as compared to their experimental estimation. Also, analytical estimation needs to be performed again when any small design change is implemented on the robot. Furthermore, it is known from experience that two robots with same design and components exhibit different stiffnesses at the end-effector/platform to a level that is unacceptable for applications such as precise positioning. This behavior can be difficult or impossible to capture using an analytical estimation approach since the reasons for this behavior are not understood. This behavior can, however, be captured using the experimental estimation approach.

For the application in focus in this thesis, precise elastostatic error compensation is desired throughout the workspace of the robot at low cost. From the characteristics of available approaches to elastostatic calibration presented above, parametric elastostatic calibration using experimental stiffness parameter identification seems ideal for our application. Hence, this approach was chosen.

1.1.3 Stiffness modelling

As mentioned in section 1.1.2, parametric elastostatic calibration using stiffness parameters is desired. This type of model relates the deflection of the platform/end-effector to the load applied on it. This model can then be used to predict and correct the pose error due to load applied on the platform/end-effector. The modelling technique differs based on the type of robot under consideration. The modelling technique needs to take into account if: (a) the robot is over-constrained or not, (b) the compliance of links are negligible or not, etc., and (c) the arms/links of the robot are heavy enough to cause considerable deflections of robot's components or not [Klimchik et al., 2014]. Pashkevich et al. [Pashkevich et al., 2011] and Klimchik et al. [Klimchik et al., 2014] have presented good overview of all the stiffness modelling methods available for all sorts of robotic manipulators. It must be noted here that robot of interest in this thesis, hexapod, is not over-constrained. Furthermore, the hexapods studied in this project had light (not heavy) legs. Therefore, the modelling approaches relevant only to such robots will be discussed. Stiffness modelling of such robotic manipulators can be classified based on two characteristics: parametric model being used and stiffness mapping method.

Based on parametric model being used, stiffness modelling approaches can be can be classified into the ones based on: (a) finite element analysis (FEA) [Corradini et al., 2003; Nagai and Liu, 2007; Bouzgarrou et al., 2004; Deblaise et al., 2006], (b) matrix structural analysis (MSA) [Deblaise et al., 2006; Li et al., 2002], and (c) virtual joint modelling (VJM) [Klimchik et al., 2013] or lumped stiffness modelling. FEA based modelling uses the classical finite element theory to discretize the components of the robot and evaluate the stiffness at the end-effector/platform using computed stiffnesses of the discrete components. The stiffnesses of these discrete elements are computed by making use of the known material properties of the components of robots. This computation is executed completely analytically (on the computer) and no experiments are involved. This method is very computationally expensive and time consuming. MSA is based on the idea similar to FEA but considers larger elements (trusses, beams, etc). This reduces the computation effort and time as compared to FEA. VJM or lumped stiffness modelling is based on extension of the conventional rigid model of the robot by considering virtual springs to describe elastic

deformations of links, joint and actuators. The number of parameters is largely reduced in comparison to FEA and MSA in this method. The stiffness parameters need to be analytically computed in FEA and MSA whereas VJM allows for experimental stiffness parameter identification. Many versions of the VJM modelling technique can be found in literature and they differ in modelling assumptions. One of the simplest versions of VJM is where each actuated joint is replaced by virtual spring [Gosselin, 1990]. This is used when the compliance of parts other than the actuated joints are negligible. This modelling technique is very simple and largely reduces complications in an experimental parameter identification framework. Such a modelling technique has also been used successfully for elastostatic calibration of serial robots for precise machining [Wu, 2014].

Stiffness mapping deals with mapping the influence of stiffness parameters of a robot to the stiffness experienced at the end-effector/platform. Based on stiffness mapping method, two types of stiffness modelling techniques exist: one based on conservative stiffness mapping and the other based on non-conservative stiffness mapping. When the end-effector/platform of a robot is loaded, the configuration of the robot changes and consequently, the stiffness experienced at the end-effector/platform changes. Conservative stiffness mapping considers the impact of change in robot's configuration, when loaded, on stiffness at the end-effector/platform whereas non-conservative stiffness mapping does not. Salisbury [Salisbury, 1980] first introduced the non-conservative stiffness mapping for a robotic manipulator and the conservative stiffness mapping was later introduced by Griffis & Duffy [Griffis and Duffy, 1993]. The magnitude of the difference in stiffness computed by the conservative and non-conservative methods depends on the stiffness of the robot and the load applied at the end-effector/platform. Therefore, non-conservative stiffness mapping is sufficient for robots which are very stiff and don't experience large deflections when loaded.

For the application concerned to this thesis, a parametric stiffness model was needed that could be used for experimental parameter identification (due to reasons stated in section 1.1.2) and that could make precise deflection predictions. Also, the robots under consideration in this thesis are very stiff and experience very small deflections relative to the size of the robot (see figure 1.3). Furthermore, compliance along actuated joints in these hexapods was expected to be dominate the compliance experienced at their plat-

forms since other components of these hexapods are relatively rigid. Therefore, a simple VJM based stiffness model (like the one in [Gosselin, 1990]) along with non-conservative stiffness mapping was used.

1.1.4 Outline of robot elastostatic calibration framework used in this thesis

The robot elastostatic calibration framework that will be used in this thesis was chosen as a result of the choices that were presented in sections 1.1.2 and 1.1.3. These choices were made considering the intended application: elastostatic calibration of a high-precision hexapod. As follows from those choices, a parametric robot elastostatic calibration framework shall be used that employs experimental stiffness identification. An elastostatic calibration framework of this nature consists of the following steps (in the order mentioned): (a) *stiffness modelling*, (b) *measurement of pose deflections* caused by application of a known forces/moments, (c) *stiffness parameter identification*, and (d) *pose error compensation* of the loaded robot. These steps can be described as follows:

(*a*) ***Stiffness modelling***: This is the first step in this process. The stiffness properties of the robot must be suitably modelled. This stiffness model must facilitate ease of experimental parameter identification while describing the system's stiffness properties accurately. As follows from the choices made in sections 1.1.2 and 1.1.3, the stiffness model to be used here will be based on virtual joint modelling (VJM) that will only consider stiffness in actuated joints. This stiffness modelling will also employ non-conservative stiffness mapping to map the influence of stiffness of actuated joints on the stiffness experienced at the end-effector/platform. Section 1.2 deals with the mathematical details of this modelling methodology.

(*b*) ***Measurement of pose deflections***: This is the second step in this process. A known load (or set of loads) must be applied at the end-effector/platform and the resultant pose deflections must be measured. Appropriate measurement system and method must be used which are suitable for the level of precision of compensation required. Redundant measurements of pose deflections must be made since the measurements are always accompanied with measurement noise. Furthermore,

these pose deflection measurements must be carried out in carefully designed experiments. Sections 1.2 and 1.3 present further insights into the nature of pose deflection measurements to be performed.

(*c*) ***Stiffness parameter identification***: This is the third step in this process. In this step, the pose deflection measurements must be appropriately treated (mathematically) to estimate the stiffness parameters. Least squares technique is generally used to identify the best set of parameters using the redundant pose deflection measurements acquired. Care should be taken to ensure that the acquired measurements are properly treated while employing the least squares technique. Section 1.2 elaborates on the mathematical details of this step.

(*d*) ***Compensation***: This is the fourth and the last step in this process. The desired pose to be achieved and the desired load to be applied on the end-effector/platform must be known. The set of stiffness parameters identified in the previous step can be used to predict the deflection of the end-effector/platform under desired loading. This prediction model can then be used to obtain the right set of actuator displacements that let the robot achieve the desired pose after undergoing deflection under the influence of the desired load.

Figure 1.5 illustrates this procedure applied to a bipod.

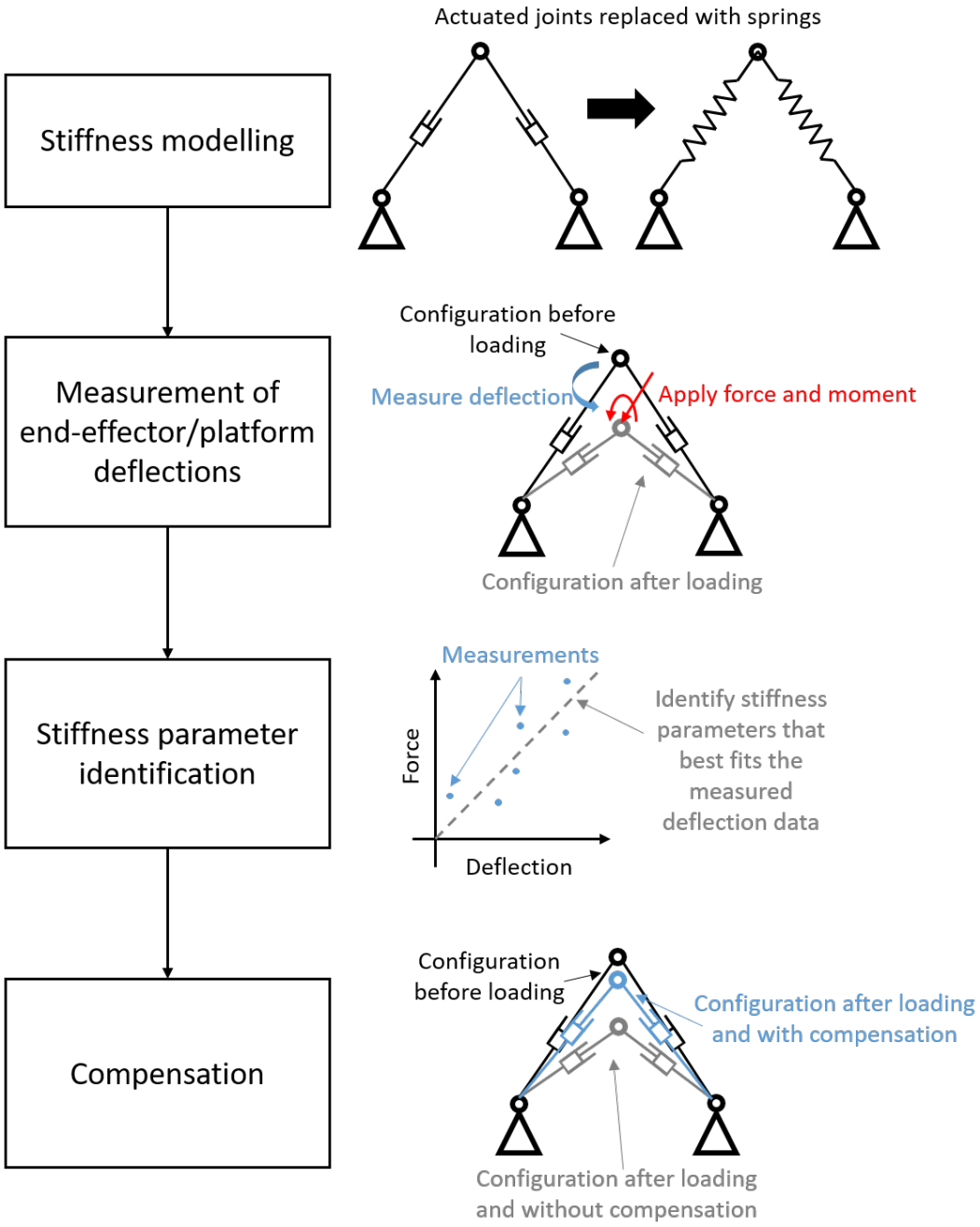

Figure 1.5: Outline of elastostatic calibration used in this thesis (illustrated on a bipod)

1.2 Mathematical framework for experimental stiffness identification in robot elastostatic calibration

This section presents the mathematical framework that is required for experimental stiffness identification in robot elastostatic calibration. This mathematical framework is as per the choices described in section 1.1. Section 1.2.1 presents the mathematical equations concerning the chosen stiffness modelling method and the stiffness identification technique. The stiffness parameter identification relies on least squares technique and this requires appropriate scaling of measured deflections and parameters, to facilitate good identification of stiffness parameters [Siciliano and Khatib, 2008, Chapter 14]. Section 1.2.2 presents the necessary appropriate techniques for scaling the measurements and parameters for good identification of these stiffness parameters.

1.2.1 Experimental stiffness identification framework

Let F^{in} and F^{fi} be the initial and final load vectors applied at the end-effector/platform of the robot. In a 3D case, these vectors have the components of force in the first three elements followed by the components of 3D moment in the next three elements. Let X^{in} and X^{fi} be the corresponding initial and final pose vectors of the end-effector/platform. The relationship between change in force/moment on the platform (ΔF) and its resultant deflection (ΔX) is given by [Merlet, 2006]

$$\Delta F = K_C \, \Delta X \tag{1.1}$$

Here, ΔF and ΔX are given by

$$\Delta F = F^{fi} - F^{in} \tag{1.2}$$

$$\Delta X = X^{fi} - X^{in} \tag{1.3}$$

K_C is called the *Cartesian stiffness matrix*. In order to obtain the expression for K_C, we need to use the equivalence between work done by the wrench applied at the end-effector/platform and the work done by resultant forces in the actuators of the robot. This relationship can be written as

$$\eta^T F = \dot{q}^T \tau \tag{1.4}$$

Here, F is any wrench applied at the end-effector/platform and η is its resulting velocity vector. τ is the force in each actuator as a consequence of F and q is the vector with actuator positions/lengths. η and $\dot{q}$ are related by means of the Jacobian matrix [Khalil and Dombre, 2004] as

$$\eta = J\,\dot{q} \tag{1.5}$$

Equations 1.4 and 1.5 give us

$$F = J^{-T}\,\tau \tag{1.6}$$

Differentiating equation 1.6, we get

$$dF = J^{-T}\,d\tau + d(J^{-T})\,\tau \tag{1.7}$$

When non-conservative stiffness mapping is employed, i.e., the influence of change in geometry of the robot (due to applied load) on the stiffness experienced at the end-effector/platform is neglected, the second term of equation 1.7 is neglected [Chen and Kao, 2000]. Equation 1.7 can then be rewritten as

$$dF = J^{-T}\,d\tau \tag{1.8}$$

Using equation 1.8, we can write

$$\Delta F = J^{-T}\,\Delta\tau = J^{-T}\,(\tau^{fi} - \tau^{in}) \tag{1.9}$$

Here, τ^{fi} and τ^{in} are the forces along actuators corresponding to the end-effector/platform wrenches F^{fi} and F^{in}, respectively. We also have

$$\Delta\tau = K\,\Delta q \tag{1.10}$$

Here, Δq is the change in actuator lengths as a result of change in forces along actuators $\Delta\tau$. This type of modelling assumes virtual springs along each actuator (as was mentioned in section 1.1.3). K is a diagonal matrix with the stiffness of actuators as its diagonal elements.

$$K = diag(k_1, k_2, ..., k_{n_p}) \tag{1.11}$$

Here, n_p denotes the number of stiffness parameters which is equal to the number of actuators in this case. Substituting for $\Delta\tau$ from equation 1.10 in equation 1.9, we get

$$\Delta F = J^{-T}\,K\,\Delta q \tag{1.12}$$

We also have

$$\Delta q = \check{J}^{-1}\,\Delta X \tag{1.13}$$

Here, $\check{J}$ is the modified Jacobian matrix. When a robot has less than two rotational degrees of freedom at the end-effector/platform, $\check{J} = J$. Using equations 1.12 and 1.13, we can write

$$\Delta F = J^{-T}\,K\,\check{J}^{-1}\,\Delta X \tag{1.14}$$

Comparing equations 1.1 and 1.14, we can write

$$K_C = J^{-T} K \check{J}^{-1} \tag{1.15}$$

Equation 1.14 can be rearranged to get

$$\Delta X = \check{J} K^{-1} J^T \Delta F \tag{1.16}$$

When elements of equation 1.14 are rearranged, we obtain

$$A\, c = \Delta X \tag{1.17}$$

A in equation 1.17 is a function of ΔF and the Jacobians and is called the *observation matrix*. It is given by

$$A_{ij} = \check{J}_{ij} \left(\sum_{r=1}^{n_p} J_{rj} \Delta F_r \right) \tag{1.18}$$

Here, A_{ij}, J_{ij} and $\check{J}_{ij}$ denote the j^{th} element of the i^{th} row of matrices A, J and $\check{J}$, respectively. ΔF_r denotes the r^{th} element of vector ΔF. c is the vector containing the compliance parameters.

$$c = \left[\frac{1}{k_1} \; \frac{1}{k_2} \; \ldots \; \frac{1}{k_{n_p}} \right]^T \tag{1.19}$$

The goal is to estimate the parameter vector c by measuring pose deflections ΔX_M at some poses X_M under the influence of force/moment applied ΔF_M. However, measurements are always accompanied with errors. All previous works on this subject have considered the error due to uncertainty of pose measurement system. It is then necessary to ensure that all the systematic errors of the measurement instrument are corrected. Taking

the random errors (due to uncertainty of pose measurements) into account, equation 1.17 can be rewritten as

$$A_M\,(c + {}^{Du}\mathcal{E}_c) = \Delta X_M + {}^{Du}\mathcal{E}_{\Delta X_M} \tag{1.20}$$

Here, A_M is the $mn \times n_p$ observation matrix corresponding to ΔF_M and X_M, where m is the number of measurements and n is the number of elements in a single deflection vector (DOFs of the end-effector/platform). ${}^{Du}\mathcal{E}_{\Delta X_M}$ is a $mn \times 1$ vector containing the errors in measurement due to uncertainty of the measurement system. The left superscript "Du" stands for *deflection uncertainty*. ${}^{Du}\mathcal{E}^{i}_{\Delta X_M}$ is the i^{th} measurement vector (of size $n \times 1$) of ${}^{Du}\mathcal{E}_{\Delta X_M}$ vector. The expectations of ${}^{Du}\mathcal{E}^{i}_{\Delta X_M}$ and ${}^{Du}\mathcal{E}_{\Delta X_M}$, $E({}^{Du}\mathcal{E}^{i}_{\Delta X_M})$ and $E({}^{Du}\mathcal{E}_{\Delta X_M})$, are zero vectors. ${}^{Du}\mathcal{E}_c$ is the error in the estimated parameter set due to ${}^{Du}\mathcal{E}_{\Delta X_M}$. The parameters that give the best fit are then generally estimated using least squares approach.

1.2.2 Scaling deflections and parameters for proper stiffness identification

Appropriate scaling of measurements and parameters is necessary to ensure good parameter estimation. This topic has been studied very well in the context of robot geometric calibration [Siciliano and Khatib, 2008; Schröer, 1993]. Since parameter identification framework for robot geometric calibration is similar to that of elastostatic calibration, same problems (and solutions) regarding scaling exist.

Two types of scaling need to be performed here [Siciliano and Khatib, 2008, Chapter 14]: (a) *task variable scaling*, and (b) *parameter scaling*. Task variable scaling is performed to ensure that: (a) the elements of the measured deflection error vector are independent [4] and identically distributed [5], and (b) the units of measurements being used for least squares fitting are same. Parameter scaling is done to improve the conditioning of the regressor matrix which in turn improves the identification quality. The regressor matrix is generally ill-conditioned when the parameter vector contains entities of varying magnitudes [Schröer,

4. meaning the elements of the vector are uncorrelated
5. meaning the elements of the vector have same standard deviation

1993]. Taking these scaling recommendations into account, equation 1.20 can be rewritten as

$$G\,A_M\,H\,H^{-1}\,(c+{}^{Du}\mathcal{E}_c) = G\,\Delta X_M + G\,{}^{Du}\mathcal{E}_{\Delta X_M} \tag{1.21}$$

In equation 1.21, G and H are the task variable and parameter scaling matrices, respectively. It must be noted that the parameter scaling matrix, H, is generally an identity matrix for elastostatic calibration of the kind being used in this work. This is because the stiffness parameters (the stiffnesses of actuated joints) of the robot have approximately same values.

The method to obtain G is well known when elements of ${}^{Du}\mathcal{E}_{\Delta X_M}$ are independent but don't have identical distribution (different standard deviations). In this case, G must contain the inverse of standard deviations of the corresponding elements of ${}^{Du}\mathcal{E}_{\Delta X_M}$ as its diagonal elements. Let this resulting task variable scaling matrix be called G_u.

$$G_u = \overbrace{\begin{bmatrix} \frac{1}{\mathcal{M}_{11}} & 0 & & \cdots & & 0 \\ 0 & \frac{1}{\mathcal{M}_{12}} & & & & \\ & & \ddots & & 0 & \vdots \\ \vdots & & & \frac{1}{\mathcal{M}_{1n}} & & \\ & 0 & & & & \\ & & & \frac{1}{\mathcal{M}_{21}} & & \\ & & & & \ddots & 0 \\ 0 & & \cdots & & 0 & \frac{1}{\mathcal{M}_{mn}} \end{bmatrix}}^{mn\times mn} \tag{1.22}$$

In equation 1.22, $\mathcal{M}_{i1}...\mathcal{M}_{in}$ are the standard deviations of elements of ${}^{Du}\mathcal{E}^{i}_{\Delta X_M}$ (the i^{th} measurement of the ${}^{Du}\mathcal{E}_{\Delta X_M}$ vector). When G_u is used for task variable scaling in least squares estimation, the method is also referred to as *weighted least squares estimation* [Seber and Lee, 2012]. When the elements of ${}^{Du}\mathcal{E}_{\Delta X_M}$ are correlated, it is usually ignored [Klimchik et al., 2012]. However, this ignorance is not necessary. Correlated measurements can be dealt with using the *generalized least squares method* [Seber and Lee, 2012] in which

task variable scaling is dealt with differently. The task variable scaling matrix in this case, G_C, is given by

$$G_C = \overbrace{\begin{bmatrix} {}_1S^{-1} & 0 & \cdots & 0 \\ 0 & {}_2S^{-1} & \cdots & 0 \\ \vdots & & \ddots & \vdots \\ 0 & \cdots & 0 & {}_mS^{-1} \end{bmatrix}}^{mn \times mn} \tag{1.23}$$

${}_iS$ is related to $Cov\left({}^{Du}\mathcal{E}^i_{\Delta X_M}\right)$ as

$$Cov\left({}^{Du}\mathcal{E}^i_{\Delta X_M}\right) = {}_iV = {}_iS\,{}_iS^T \tag{1.24}$$

To obtain ${}_iS$, eigen value decomposition of $Cov\left({}^{Du}\mathcal{E}^i_{\Delta X_M}\right)$ needs to be performed. As mentioned earlier, task variable scaling is done so that the resulting measured deflection vector becomes I.I.D (independent and identically distributed) and their elements possess same units. Appendix B presents the proof of the resulting deflection error vector being I.I.D and dimensionless.

1.3 Stiffness identification optimization

This section presents the concept and state of the art of the methods to optimize experimental stiffness parameter identification for robot elastostatic calibration. Section 1.3.1 presents the mathematical background behind parameter identification optimization while using a least squares technique. Section 1.3.2 presents the various methods that exist in the literature for optimizing parameter identification and provides an in-depth explanation of each one of them. Section 1.3.3 lists and elaborates on the limitations of the existing stiffness identification optimization methods.

1.3.1 Optimizing experiment design

In experimental parameter identification, a linear regression model is used to describe the relation between measurements and parameters to be estimated by means of a regressor. Equation 1.25 shows the general form of this regression model.

$$\mathcal{A}\,\check{\mathcal{X}} = \mathcal{A}\,(\mathcal{X} + \mathcal{E}_{\mathcal{X}}) = \mathcal{B} + \mathcal{E}_{\mathcal{B}} = \check{\mathcal{B}} \tag{1.25}$$

Here, parameter vector $\mathcal{X}$ needs to be identified when $\mathcal{B}$ is measured. These two are assumed to be related using the regressor matrix $\mathcal{A}$. Many redundant measurements are performed in order to find the parameter set that best fits the measurement data. Measurement is always accompanied with error vector $\mathcal{E}_{\mathcal{B}}$ which are assumed to be a consequence of random measurement errors from the measurement system. This measurement error leads to errors in identified parameters, $\mathcal{E}_{\mathcal{X}}$. $\check{\mathcal{X}}$ is obtained using

$$\check{\mathcal{X}} = \overbrace{\left(\mathcal{A}^{\mathsf{T}}\,\mathcal{A}\right)^{-1}\mathcal{A}^{\mathsf{T}}}^{\mathcal{A}^{+}}\,\check{\mathcal{B}} \tag{1.26}$$

where $\mathcal{A}^{+}$ is the pseudo-inverse of $\mathcal{A}$. It can be seen clearly in equation 1.26 that the regressor matrix $\mathcal{A}$ controls the propagation of errors from measurements to identified parameters. Hence, choice of $\mathcal{A}$ is crucial for good parameter identification. *Theory of experiment design* [Atkinson et al., 2007] focuses this phenomenon and approaches to obtain better parameter estimates when measurements have the said random errors.

To understand the significance of optimization of experiment design in the context of experimental stiffness parameter identification, let us first reformulate equation 1.21 to obtain

$$\widetilde{\overline{A_M}}\,H^{-1}\check{c} = \widetilde{\overline{A_M}}\,\bar{\check{c}} = G(\Delta X_M + {}^{Du}\mathcal{E}_{\Delta X_M}) \tag{1.27}$$

Here, $\widetilde{\overline{A_M}} = G\, A_M\, H$, $\check{c} = c + {}^{Du}\varepsilon_c$ and $\bar{\check{c}} = H^{-1}\check{c}$. The stiffness parameter estimate is then obtained as per

$$\check{c} = H\left(\widetilde{\overline{A_M}}^T \widetilde{\overline{A_M}}\right)^{-1} \widetilde{\overline{A_M}}^T \left(G(\Delta X_M + {}^{Du}\varepsilon_{\Delta X_M})\right) \tag{1.28}$$

It is apparent from equation 1.28 that $\widetilde{\overline{A_M}}$ controls the propagation of error (due to measurement uncertainty) from measurements to identified parameters. Consequently, $\widetilde{\overline{A_M}}$ must be chosen carefully for stiffness parameter identification. It is important to minimize this propagation and identify best set of parameters because they directly affect the quality of compensation achieved. Figure 1.6 shows an illustration of error propagation from measured deflection to accuracy attained after compensation in a one dimensional case when an identification experiment is performed many number of times. Many previous works have also demonstrated the importance of good experiment design by choosing a good regressor matrix for robot geometric calibration [Menq et al., 1989; Driels and Pathre, 1990; Joubair and Bonev, 2013]. In the context of robot geometric calibration, the regresor matrix is a function of pose at which the identification experiment is performed. Consequently, best set of poses are chosen for performing geometric parameter identification. In our case, as $\widetilde{\overline{A_M}}$ depends on the *choice of measurement pose* (X_M) *and the effective force/moment applied at the platform* (ΔF_M), it is necessary to find the best set of X_M and ΔF_M.

1.3.2 Existing methods for optimizing parameter identification

As mentioned earlier, the topic of finding the best regressor matrix in order to obtain the best set of parameter estimates has been a topic of interest in various fields. Many criteria exist in the theory of experiment design that are used to optimize experiment design in order to obtain best parameter estimates [Atkinson et al., 2007]. This topic has also been extensively studied to find the best set of poses for measurement in robot geometric calibration. Due to similarity of the general mathematical framework of parameter estimation, the parameter identification optimization criteria proposed in theory of experiment design and robot geometric parameter identification can be directly applied to robot stiffness pa-

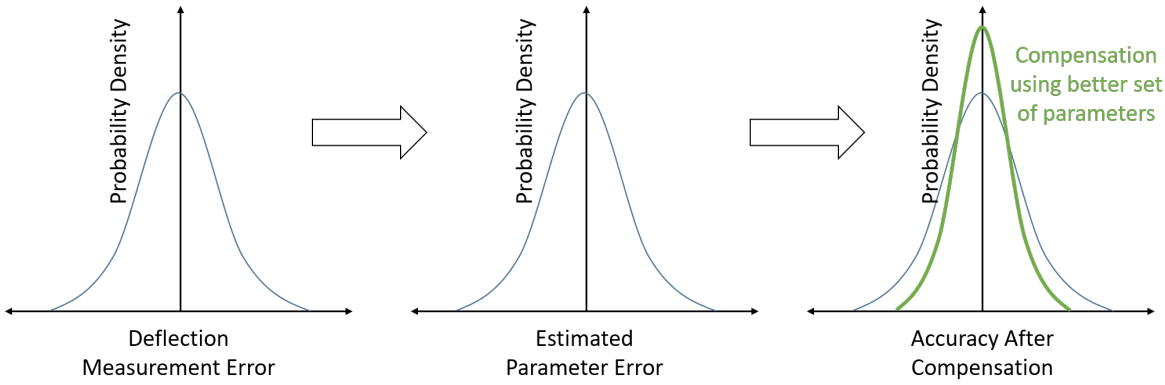

Figure 1.6: Error propagation from measured deflection to attained compensation in a one dimensional case when an identification experiment is performed many number of times (with the assumption that the stiffness model is perfect)

rameter identification. These optimization criteria can be broadly classified into:(a) *criteria focused on minimizing parameter error*, and (b) *criteria focused on minimizing pose error after compensation*. The former focuses on different interpretations of what it means to minimize the errors in identified parameters. Criteria that fall under this classification do not explicitly consider the specific requirements of the positioning application that the robot will be used for. In contrast, criteria focused on minimizing pose error after compensation considers (to varying extents, depending on the criterion) the intended application's specification. This allows the user to identify the set of parameters best suited for the particular application. Some of these criteria are listed in table 1.1. This classification defines the difference between *application-oriented* and *non-application-oriented* robot elastostatic calibrations (see figure 1.7).

The reasoning behind different previously proposed criteria for optimizing parameter identification, explained in the context of stiffness parameter identification optimization, are as follows:

(*a*) *A-optimality*: This criterion aims at minimizing the total variance of parameter es-

Table 1.1: Existing criteria to select best robot calibration experiment design

Criterion	Objective function
$A-optimality$ [Atkinson et al., 2007]	$tr(Cov(\check{c})) \rightarrow min$
$D-optimality$ [Atkinson et al., 2007]	$det\left(\left(Cov(\check{c})\right)^{-1}\right) \rightarrow max$
$E-optimality$ [Atkinson et al., 2007]	$min\left(eig\left(\left(Cov(\check{c})\right)^{-1}\right)\right) \rightarrow max$
$G-optimality$ [Atkinson et al., 2007]	$max\left(diag\left(Cov(\check{c})\right)\right) \rightarrow min$
O_1 [Borm and Menq, 1989]	$\frac{(\mu_1\mu_2\mu_3....\mu_{n_p})^{1/n_p}}{\sqrt{m}} \rightarrow max$
O_2 [Driels and Pathre, 1990]	$\frac{\mu_{min}}{\mu_{max}} \rightarrow max$
O_3 [Nahvi et al., 1994]	$\mu_{min} \rightarrow max$
O_4 [Nahvi and Hollerbach, 1996]	$\frac{(\mu_{min})^2}{\mu_{max}} \rightarrow max$
O_5 [Sun and Hollerbach, 2008]	$\frac{1}{\frac{1}{\mu_1}+\frac{1}{\mu_2}+...+\frac{1}{\mu_{n_p}}} \rightarrow max$
O_{TP} [Wu, 2014]	$tr\left(A_D\, H\, (\widetilde{A_M}^T \widetilde{A_M})^{-1}\, H^T\, A_D^T\right) \rightarrow min; l=1$
O_{MV} [Carrillo et al., 2013]	$\frac{1}{l}\sum_{i=1}^{l}\left(tr\left({}^iA_D\, H\, (\widetilde{A_M}^T \widetilde{A_M})^{-1}\, H^T\, {}^iA_D^T\right)\right) \rightarrow min$

'l' is the number of pose-force sets at which best performance is required; '$\mu_1, \mu_2 .... \mu_{n_p}$' are the singular values of $\widetilde{A_M}$; 'μ_{min}' and 'μ_{max}' are the minimum and maximum singular values of $\widetilde{A_M}$, respectively; 'A_D is the matrix A formulated using the set of poses (X_D) and forces/moments (ΔF_D) at which best positioning performance is desired

timates. Considering the identification as per equation 1.28, the optimization problem of this criterion is framed as

$$tr(Cov(\check{c})) \rightarrow min \tag{1.29}$$

Another variation of this criterion is called *T-optimality* criterion. This is given by

$$tr\left(\left(Cov(\check{c})\right)^{-1}\right) \rightarrow max \tag{1.30}$$

A- and T-optimality criteria are the same objective functions in essence.

(*b*) *D-optimality*: D-optimal design aims at minimizing the determinant of information

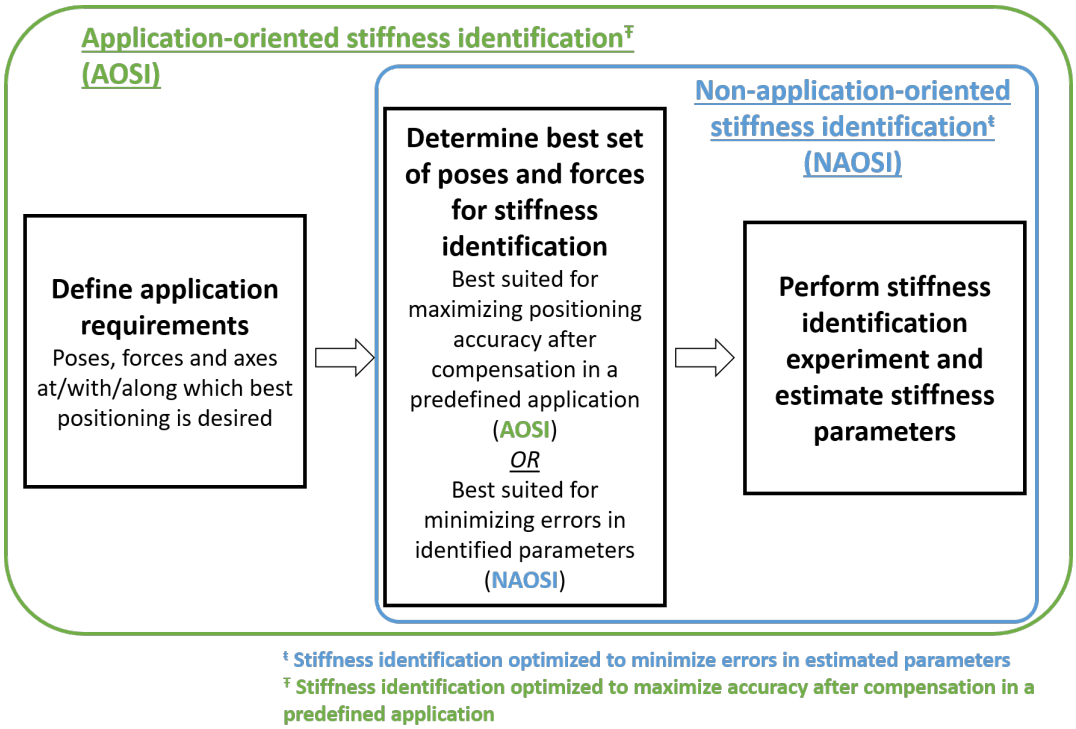

Figure 1.7: Application-oriented and non-application-oriented stiffness identifications

matrix (inverse of the covariance matrix) of the estimated parameters. The optimization problem of this criterion is given by

$$\det\left(\left(\mathrm{Cov}(\check{\mathbf{c}})\right)^{-1}\right) \rightarrow \max \tag{1.31}$$

To understand the aim of this criterion, consider the illustration of figure 1.8. In this figure, the propagation of an error ellipse [6] representing randomly varying measurement error to error ellipse representing the corresponding parameter errors is shown. The regressor matrix, as already known, controls the scaling and rotation of

6. Error ellipses (or confidence ellipse/ellipsoid) are used to visualize the boundary within which a certain number of samples of randomly varying variables lie. These elliptical/ellipsoidal boundaries are defined by axes dependent on standard deviations of the variables. For example, for a bi-variate (two-dimensional) Gaussian distribution in which both variables have same variance, 99.7% of the samples lie within the circular boundary defined by a radius that is three times the standard deviation of the variables' distributions [Seber and Lee, 2012].

these error ellipses. D-optimal design aims at minimizing the area (or volume for an ellipsoid) of the parameter error ellipse for a given measurement error ellipse.

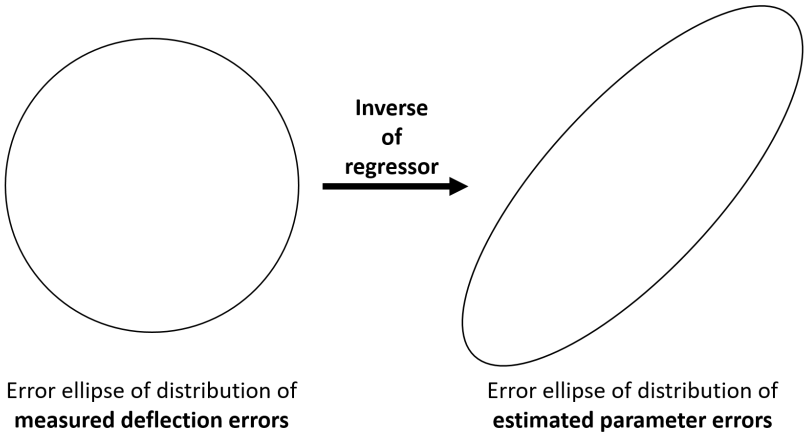

Figure 1.8: Propagation of error ellipses in stiffness parameter identification routine (shown for a two dimensional case)

(*c*) *E-optimality*: This criterion maximizes the minimum eigen value of the information matrix. The optimization problem for this criterion is given by

$$\min\left(eig\left(\left(Cov(\check{c})\right)^{-1}\right)\right) \rightarrow max \tag{1.32}$$

(*d*) *G-optimality*: This criterion aims at minimizing the maximum of the variances of the predicted parameters. The optimization problem for this criterion is given by

$$max\left(diag\left(Cov(\check{c})\right)\right) \rightarrow min \tag{1.33}$$

(*e*) O_1: Borm and Menq [Borm and Menq, 1989] first proposed this observability index for robot geometric calibration. This aims at maximizing the product of singular values of the regressor matrix.

$$\frac{(\mu_1\mu_2\mu_3....\mu_{n_p})^{1/n_p}}{\sqrt{m}} \rightarrow max \tag{1.34}$$

Here, μ_i are the singular values of $\widetilde{A_M}$. From a geometrical viewpoint (of error ellipse propagation as in figure 1.8), it can be shown that the volume of parameter error ellipsoid is proportional to the product of the singular values of the inverse of regressor

matrix. Maximzing the product of singular values of the regressor matrix minimizes the product of the singular values of the inverse of regressor matrix. This will effectively minimize the volume of parameter error ellipsoid for any given measurement error ellipsoid.

(f) O_2: Driels and Pathre [Driels and Pathre, 1990] introduced this observability index. It is given by

$$\frac{\mu_{min}}{\mu_{max}} \rightarrow max \tag{1.35}$$

Here, μ_{min} and μ_{max} are the minimum and maximum singular values of $\overline{\widetilde{A_M}}$, respectively. In the context of the illustration in figure 1.8, criterion aims at minimizing the eccentricity of the parameter error ellipsoid.

(g) O_3: Nahvi et al. [Nahvi et al., 1994] proposed this index and it aims at maximizing the minimum singular value of the regressor matrix.

$$\mu_{min} \rightarrow max \tag{1.36}$$

Nahvi et al. [Nahvi et al., 1994] showed that the minimum singular value of the regressor matrix acts as a de-amplifier in the propagation of the norm of measured deflection errors to norm of estimated parameter errors. In the context of the illustration in figure 1.8, this criterion aims at minimizing the largest semi-axis of the parameter error ellipsoid.

(h) O_4: Nahvi and Hollerbach [Nahvi and Hollerbach, 1996] proposed the following optimization problem to optimize parameter identification:

$$\frac{(\mu_{min})^2}{\mu_{max}} \rightarrow max \tag{1.37}$$

This observability index is also called the *noise amplification index*. This is because Nahvi and Hollerbach [Nahvi and Hollerbach, 1996] have shown that the norm of error in identified parameters is an amplification of the norm of error in measured deflections by a factor $\frac{\mu_{max}}{(\mu_{min})^2}$. Consequently, maximizing $\frac{(\mu_{min})^2}{\mu_{max}}$ will lead to minimum norm of error in identified parameters. In terms of error ellipsoid propagation

(as in figure 1.8), this observability index minimizes both the eccentricity and the size of parameter error ellipsoid.

(*i*) O_5: Sun and Hollerbach [Sun and Hollerbach, 2008] showed that the previous four observability indices, $O_1 - O_4$, are related to the alphabet optimalities from experiment design theory, except A-optimality. They then proposed O_5 which is equivalent to A-optimality.

$$\frac{1}{\frac{1}{\mu_1}+\frac{1}{\mu_2}+\ldots+\frac{1}{\mu_{n_p}}} \rightarrow max \tag{1.38}$$

(*j*) O_{TP}: Wu [Wu, 2014] proposed this criterion and this minimizes the RMS value of Euclidean norm of possible end-effector pose errors after calibration. The optimization problem of this criterion is given by

$$tr\left(A_D\, H\, \left(\widetilde{\widetilde{A_M}}^T \widetilde{\widetilde{A_M}}\right)^{-1} H^T\, A_D^T\right) \rightarrow min; l = 1 \tag{1.39}$$

In this, A_D is a function of the desired set of poses and forces/moments at and with which best performance positioning is required. l is the number of pose-force sets at which best positioning performance is required. This criterion is useful when the end-effector pose coordinates have translational coordinates only[7].

(*k*) O_{MV}: Carillo et al. [Carrillo et al., 2013] proposed a criterion similar to O_{TP}. In this, the average (over desired high performance pose-force sets) of the RMS of Euclidean norms of possible end-effector pose errors after calibration is minimized.

$$\frac{1}{l}\sum_{i=1}^{l}\left(tr\left({}^iA_D\, H\, \left(\widetilde{\widetilde{A_M}}^T \widetilde{\widetilde{A_M}}\right)^{-1} H^T\, {}^iA_D^T\right)\right) \rightarrow min \tag{1.40}$$

From all the stiffness parameter identification criteria listed above, all except O_{TP} and O_{MV} focus on minimizing parameter errors. It is worth noting here that Imoto et al. [Imoto et al., 2009] were the first ones to present a parameter identification optimization criterion focused on minimizing pose error after compensation. This criterion was developed for

7. Alternatively, the end-effector's orientations can be expressed using Cartesian coordinates of several reference points, as done by Wu [Wu, 2014].

robot geometric calibration. However, this criterion was designed considering their specific method of measuring the robot's accuracy which is different from how accuracy of robots are generally specified or measured.

1.3.3 Limitations of existing stiffness identification optimization methods

Having robots perform their assigned positioning task as best as possible is very desirable. In many cases, the specification of these positioning tasks are pre-defined. It is very desirable in these cases to identify parameters which are best suited for the intended application. It must be noted that parameter estimation is just a stepping stone to pose error compensation. Parameter errors can not be eliminated completely but can be acquired in a way that is most favorable for the intended compensation. Thus, it is advantageous to find poses and forces/moments for stiffness identification that minimize the influence of errors influencing stiffness identification on the accuracy after compensation. Moreover, some applications can demand best positioning performance along certain selected axes of the end-effector/platform only. In such a case, it is best to identify parameters that minimize the pose errors after compensation along those axes only as the user does not need best positioning performance along the other axes [8]. This is especially important in the context of the project corcerned to this thesis. This is because the partner company, Symétrie, often receives demands of this nature from their customers. Appendix C presents the details of an application where best positioning was required along certain selected axes of the platform of the robot. None of the methods present in the literature can be used in this case to obtain best possible results.

Furthermore, one aspect of stiffness parameter identification optimization has not been given any attention as yet. It is the fact that the force/moment actually applied during identification experiment will not be the same as the assumed value. This can have significant impact on compensation accuracy, especially for high-precision positioning robots.

8. Not obtaining best positioning performance along certain axes does not imply that the positioning performance along the those axes will be extremely bad. The robot will achieve high positioning performance along "non-best-performance axes" as well when a high-precision pose measurement instrument is used However, it won't achieve the best possible positioning performance along these non-best-performance axes.

Appendix D presents a study in which the impact of error in applied force/moment on the compensation accuracy has been studied for a hexapod positioning system. Results of this study show that error in applied force/moment indeed has a non-negligible impact on compensation accuracy.

The limitations of existing stiffness parameter identification criteria highlighted above define the requirements for a new criterion/criteria to be developed. Therefore, this new method should allow the user to optimize stiffness parameter identification such that:

1. best possible positioning performance can be achieved: (a) at desired poses, (b) along desired axes of the robot, and (c) with desired loads on the robot's platform.
2. the influence of error sources impacting stiffness identification, deflection measurement uncertainty and errors in forces/moments applied, on compensation quality can be minimized.

1.4 Conclusion

This chapter presented the state of the art and background of robot elastostatic calibration and its optimization. The concept of elastostatic calibration was first introduced along with the justification for its need for high-precision positioning hexapods. Different existing choices to perform elastostatic calibration were presented. This was followed by presentation and justification of the chosen method: parametric elastostatic calibration with experimental stiffness identification. The necessary mathematical background for experimental stiffness identification and its optimization was then presented. The existing criteria for optimizing stiffness identification for robot elastostatic calibration were presented and their limitations were discussed. These limitations dictated the requirements for a new criterion/set of criteria to be developed for optimizing stiffness identification. This set of requirements have been presented and discussed.

CHAPTER

2 Application-oriented robot elastostatic calibration optimization

Contents

Chapter Abstract

This chapter presents a stiffness identification optimization framework that counters the limitations[1] *of the existing criteria for the same. This framework helps to choose measurement conditions for stiffness identification (poses and forces/moments) that minimize the impact of errors influencing stiffness identification*[2] *on compensation quality. Discussion on the usage of the proposed framework is also provided.*

1. Presented in chapter 1.
2. Deflection measurement errors and errors in forces/moments applied.

2.1 Introduction

2.1.1 Requirements and proposed solutions

As mentioned in chapter 1, parametric elastostatic calibration with experimental stiffness identification was chosen to improve the accuracy of high-precision positioning hexapods when their platforms are loaded. This involves modelling the stiffness properties of the robot using a parametric stiffness model. The parameters of this model are estimated with the help of least squares method using measured deflections of the robot due to known applied loads. It was also shown that stiffness identification can be optimized by choosing the best set of poses and forces/moments used for the identification experiment. Several works proposing different criteria for stiffness identification optimization exist in the literature. These can be classified into the ones focused on minimizing the errors in estimated parameters and the ones focused on minimizing the compensation error after calibration. The latter approach was considered suitable for the work in this thesis. However, the existing criteria to achieve this have two main disadvantages and they define the requirements for the new criterion/criteria to be developed.

The first disadvantage of existing stiffness identification optimization criteria is their inability in ensuring best possible compensation no matter what the specifications of the positioning application are. Robot positioning applications can be of varied natures. An application might require the robot to be able to achieve best possible accuracy: (a) at some chosen poses or throughout the workspace, (b) along some chosen axes of the robot or along every axis, and (c) using some fixed load or a set of loads. Therefore, a truly application-oriented elastostatic calibration method must be able to deliver best possible positioning accuracy no matter what the application's specifications are. Consequently, the stiffness identification optimization criterion/criteria must be able to ensure best compensation quality in any specified positioning application. As explained in chapter 1, none of the stiffness identification optimization criteria present in the literature can satisfy this requirement. Hence, the new criterion or set of criteria for stiffness identification optimization must be able to satisfy this requirement.

The second disadvantage of existing stiffness identification optimization criteria is

their inability to minimize the influence of errors in forces/moments applied during stiffness identification on compensation quality. It was shown that the errors in applied forces/moments during stiffness identification experiment can have considerable impact on the positioning accuracy after compensation of a loaded robot. No work exists in the literature that considers the influence of this while choosing the best set of poses and forces/-moments for stiffness identification experiment. Hence, the new criterion/criteria to be developed must minimize the influence of: (a) the errors in forces/moments applied during stiffness identification experiment, and (b) the uncertainty of measured deflections, on the positioning accuracy after compensation of the loaded robot.

In light of the requirements mentioned above, a two step strategy is used here to find the criterion/criteria to optimize stiffness identification. First, the stiffness identification problem (equation 1.21) is reformulated to consider the influence of applied force/moment error on estimated stiffness parameters. Following this, equations are derived that relate the input [3] and the output [4] errors. These relationships allow a user to formulate criterion/criteria to choose best set of poses and forces/moments for stiffness identification based on a given application's specifications.

2.1.2 Outline of this chapter

Section 2.2 presents the reformulation of the stiffness identification problem. Section 2.3 presents the relationship between uncertainty of measured deflections and the uncertainty of resultant pose errors after compensation. It also discusses ways to formulate criteria to minimize the influence of uncertainty of measured deflections on the pose error after compensation in the application at hand. Section 2.4 presents the relationship between errors in applied forces/moments during stiffness identification and the resultant pose error after compensation. Subsequently, it discusses ways to formulate criterion/criteria to minimize the influence of errors in forces/moments applied for stiffness identification on the pose error after compensation in the application at hand. Finally, section 2.5 presents the conclusions of this chapter.

3. Errors in applied forces/moments and uncertainty of deflection measurement errors.
4. Resultant pose errors after compensation.

2.2 Reformulation of the stiffness identification problem

The need for reformulating the stiffness identification problem as in equation 1.21 is necessary in order to accommodate the influence of error in applied forces/moments during stiffness identification experiment. To do this, let us first mathematize the origin of this problem.

The origin of the problem is the difference (no matter how small) between the assumed and actual forces/moments applied during stiffness identification experiments. As a consequence of this, matrix A_M of equation 1.21 will be formulated using assumed applied loads and not the actual loads applied. Let the matrix A_M formulated using assumed loads be called ${}^{as}A_M$. ${}^{as}A_M$ is a function of X_M and the assumed differential force vector applied at the platform (${}^{as}\Delta F_M$). ${}^{as}\Delta F_M$ is given by

$$ {}^{as}\Delta F_M = \overbrace{\left[{}^{as}_{11}\Delta F_M{}^T \; {}^{as}_{12}\Delta F_M{}^T .... \; {}^{as}_{21}\Delta F_M{}^T .... \right]^T}^{n_f m \times 1} \tag{2.1} $$

Here, n_f is the number of elements in a single force vector. ${}^{as}_{ij}\Delta F_M$ is the assumed differential force vector corresponding to the j^{th} measurement at i^{th} measurement pose X^i_M. ${}^{as}_{ij}\Delta F_M$ is given by

$$ {}^{as}_{ij}\Delta F_M = {}^{as}_{ij}F^{fi}_M - {}^{as}_{ij}F^{in}_M \tag{2.2} $$

Here, ${}^{as}_{ij}F^{fi}_M$ and ${}^{as}_{ij}F^{in}_M$ are the final and initial loads that are assumed to have been applied at the end-effector/platform during the corresponding measurement, respectively. These are, however, different from the loads that are actually applied at the end-effector/platform. The actual differential load applied, ${}^{ac}_{ij}\Delta F_M$, is given by

$$ {}^{ac}_{ij}\Delta F_M = {}^{ac}_{ij}F^{fi}_M - {}^{ac}_{ij}F^{in}_M \tag{2.3} $$

Here, ${}^{ac}_{ij}F^{fi}_M$ and ${}^{ac}_{ij}F^{in}_M$ are the final and initial loads that are actually applied at the end-

effector/platform during the corresponding measurement. The error in applied force/moment is then given by

$$ {}_{ij}\mathcal{E}_{\Delta F_M} = {}^{ac}_{ij}\Delta F_M - {}^{as}_{ij}\Delta F_M \tag{2.4} $$

$$ \mathcal{E}_{\Delta F_M} = \left[{}_{11}\mathcal{E}_{\Delta F_M}{}^T \; {}_{12}\mathcal{E}_{\Delta F_M}{}^T \ldots {}_{21}\mathcal{E}_{\Delta F_M}{}^T .. \right]^T \tag{2.5} $$

The error in applied force/moment, $\mathcal{E}_{\Delta F_M}$, will result in an extra error in measured deflection[5]. Let this error in measured deflection due to $\mathcal{E}_{\Delta F_M}$ be called ${}^{FE}\mathcal{E}_{\Delta X_M}$. The left superscript "FE" stands for *force error*. The stiffness identification problem can then be reformulated to include the influence of applied force/moment error in the following manner:

$$ G\ {}^{as}A_M\ H\ H^{-1}\ (c + {}^{DU}\mathcal{E}_c + {}^{FE}\mathcal{E}_c) = G\ (\Delta X_M + {}^{DU}\mathcal{E}_{\Delta X_M} + {}^{FE}\mathcal{E}_{\Delta X_M}) \tag{2.6} $$

In equation 2.6, errors in estimated stiffness parameters are a consequence of errors in applied forces/moments and errors in deflection measurements. In this, ${}^{FE}\mathcal{E}_{\Delta X_M}$, which is a consequence of $\mathcal{E}_{\Delta F_M}$, leads to the corresponding error in estimated parameter, ${}^{FE}\mathcal{E}_c$. It must be noted here that matrix G must be appropriately computed in this case. This is because ${}^{FE}\mathcal{E}_{\Delta X_M}$ can also influence the variance of the total measured deflection vector.

As mentioned before, ${}^{DU}\mathcal{E}_{\Delta X_M}$ is a consequence of the uncertainty of pose measurement system. Consequently, the variance of measurements of pose measurement system decides the variance of ${}^{DU}\mathcal{E}_{\Delta X_M}$. This in turn contributes to the variance of positioning errors after compensation. Hence, a relationship relating the variance of ${}^{DU}\mathcal{E}_{\Delta X_M}$ to the corresponding component of variance of compensation errors can be useful in minimizing the influence of the former on the latter when the former is given. Section 2.3 presents this relationship and the ways to use it to optimize stiffness identification. The stiffness identification optimization criterion developed using this approach shall be called *DUIR criterion*, which stands for *deflection measurement uncertainty influence reduction criterion*.

5. In addition to the error in measured deflection due to uncertainty of the pose measurement system.

Similarly, a relationship relating ${}^{FE}\mathcal{E}_{\Delta X_M}$ and the corresponding component of compensation error can be useful in minimizing the influence of the former on the latter. Section 2.4 presents this relationship and the ways to use it to optimize stiffness identification. The stiffness identification optimization criterion developed using this approach shall be called *FEIR criterion*, which stands for *force error influence reduction criterion*. Figure 2.1 presents the flowchart of procedure to find best set of poses and forces/moments for stiffness identification using this method.

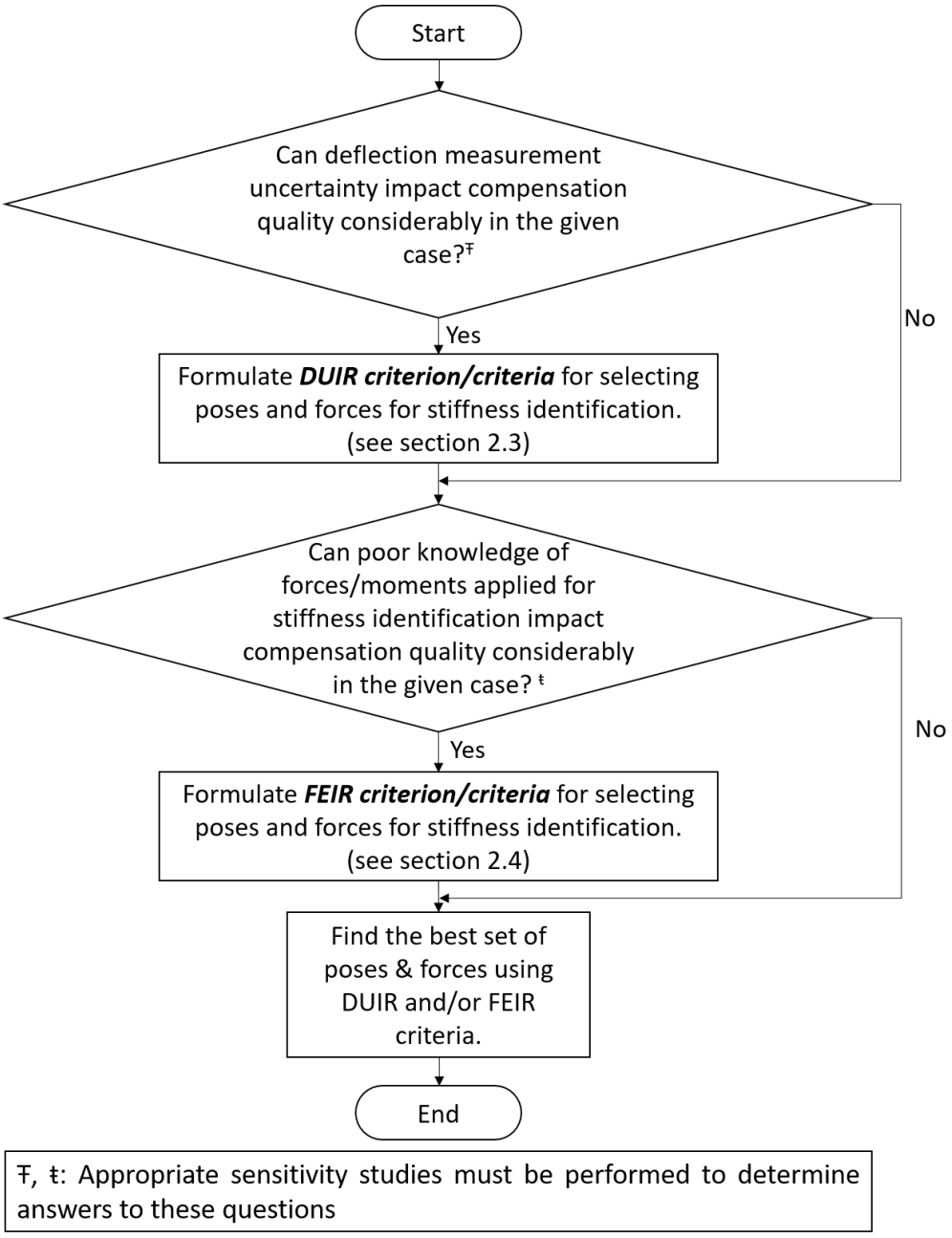

Figure 2.1: Flowchart of procedure to find best set of poses and forces/moments for stiffness identification as per the proposed method

2.3 Minimizing the influence of deflection measurement uncertainty on positioning error after compensation (DUIR criterion)

2.3.1 Relationship between deflection measurement uncertainty and the uncertainty of resultant positioning error after compensation

In order to derive the necessary relationship, the expression for the estimated parameter set can be first derived. To simplify this derivation, equation 2.6 can be rewritten in a simpler form as

$$^{as}\widetilde{A_M}\, H^{-1}\, \widehat{c} = G\, \widehat{\Delta X_M} \tag{2.7}$$

In equation 2.7, $^{as}\widetilde{A_M} = G\ {}^{as}A_M\ H$, $\widehat{c} = c + {}^{DU}\mathcal{E}_c + {}^{FE}\mathcal{E}_c$ and $\widehat{\Delta X_M} = \Delta X_M + {}^{DU}\mathcal{E}_{\Delta X_M} + {}^{FE}\mathcal{E}_{\Delta X_M}$. The estimated parameter set $\widehat{c}$ can then be estimated using the formula

$$\widehat{c} = H \underbrace{(^{as}\widetilde{A_M}^{T}\ {}^{as}\widetilde{A_M})^{-1}\ {}^{as}\widetilde{A_M}^{T}}_{^{as}\widetilde{A_M}^{+}} G\, \widehat{\Delta X_M} \tag{2.8}$$

In equation 2.8, $(^{as}\widetilde{A_M}^{T}\ {}^{as}\widetilde{A_M})^{-1}\ {}^{as}\widetilde{A_M}^{T}$ is nothing but the pseudo-inverse of $^{as}\widetilde{A_M}$, $^{as}\widetilde{A_M}^{+}$. From equations 2.8 and 2.6, the following expression can be written:

$$^{DU}\mathcal{E}_c = \underbrace{H \overbrace{(^{as}\widetilde{A_M}^{T}\ {}^{as}\widetilde{A_M})^{-1}\ {}^{as}\widetilde{A_M}^{T}}^{^{as}\widetilde{A_M}^{+}}}_{N} \underbrace{G\ {}^{DU}\mathcal{E}_{\Delta X_M}}_{^{DU}\widetilde{\mathcal{E}}_{\Delta X_M}} \tag{2.9}$$

Let $H\ (^{as}\widetilde{A_M}^{T}\ {}^{as}\widetilde{A_M})^{-1}\ {}^{as}\widetilde{A_M}^{T}$ in equation 2.9 be replaced by N for simplifying its further analysis. Furthermore, let $G\ {}^{DU}\mathcal{E}_{\Delta X_M}$ be replaced by $^{DU}\widetilde{\mathcal{E}}_{\Delta X_M}$ for the same reason.

Now, the influence of deflection measurement uncertainty on the uncertainty of estimated parameter set can be evaluated using the expression

$$\mathrm{Cov}({}^{\mathrm{Du}}\mathcal{E}_c) = \mathrm{N}\ \mathrm{Cov}({}^{\mathrm{Du}}\widetilde{\mathcal{E}}_{\Delta X_M})\ \mathrm{N}^{\mathrm{T}} \tag{2.10}$$

In equation 2.10, $\mathrm{Cov}({}^{\mathrm{Du}}\widetilde{\mathcal{E}}_{\Delta X_M})$ can be written as

$$\mathrm{Cov}({}^{\mathrm{Du}}\widetilde{\mathcal{E}}_{\Delta X_M}) = ({}^{\mathrm{Du}}\sigma_{\widetilde{\mathcal{E}}_{\Delta X_M}})^2\ \mathrm{I} \tag{2.11}$$

Here, ${}^{\mathrm{Du}}\sigma_{\widetilde{\mathcal{E}}_{\Delta X_M}}$ is the standard deviation of elements[6] of ${}^{\mathrm{Du}}\widetilde{\mathcal{E}}_{\Delta X_M}$ and I is an identity matrix. The expression of equation 2.11 follows from the fact that ${}^{\mathrm{Du}}\widetilde{\mathcal{E}}_{\Delta X_M}$ is independent and identically distributed[7]. By substituting for $\mathrm{Cov}({}^{\mathrm{Du}}\widetilde{\mathcal{E}}_{\Delta X_M})$ from equation 2.11 in equation 2.10, the following expression can be obtained:

$$\mathrm{Cov}({}^{\mathrm{Du}}\mathcal{E}_c) = \mathrm{N}\ ({}^{\mathrm{Du}}\sigma_{\widetilde{\mathcal{E}}_{\Delta X_M}})^2\ \mathrm{I}\ \mathrm{N}^{\mathrm{T}} \tag{2.12}$$

Equation 2.12 can then be expanded to get

$$\begin{aligned}
&\mathrm{Cov}({}^{\mathrm{Du}}\mathcal{E}_c)\\
&= ({}^{\mathrm{Du}}\sigma_{\widetilde{\mathcal{E}}_{\Delta X_M}})^2 \left(\mathrm{H}\ ({}^{\mathrm{as}}\widetilde{\mathrm{A}_M}^{\mathrm{T}}\ {}^{\mathrm{as}}\widetilde{\mathrm{A}_M})^{-1}\ {}^{\mathrm{as}}\widetilde{\mathrm{A}_M}^{\mathrm{T}}\right) \left(\mathrm{H}\ ({}^{\mathrm{as}}\widetilde{\mathrm{A}_M}^{\mathrm{T}}\ {}^{\mathrm{as}}\widetilde{\mathrm{A}_M})^{-1}\ {}^{\mathrm{as}}\widetilde{\mathrm{A}_M}^{\mathrm{T}}\right)^{\mathrm{T}}\\
&= ({}^{\mathrm{Du}}\sigma_{\widetilde{\mathcal{E}}_{\Delta X_M}})^2\ \mathrm{H}\ ({}^{\mathrm{as}}\widetilde{\mathrm{A}_M}^{\mathrm{T}}\ {}^{\mathrm{as}}\widetilde{\mathrm{A}_M})^{-1}\ {}^{\mathrm{as}}\widetilde{\mathrm{A}_M}^{\mathrm{T}} \left(({}^{\mathrm{as}}\widetilde{\mathrm{A}_M}^{\mathrm{T}}\ {}^{\mathrm{as}}\widetilde{\mathrm{A}_M})^{-1}\ {}^{\mathrm{as}}\widetilde{\mathrm{A}_M}^{\mathrm{T}}\right)^{\mathrm{T}}\ \mathrm{H}^{\mathrm{T}}\\
&= ({}^{\mathrm{Du}}\sigma_{\widetilde{\mathcal{E}}_{\Delta X_M}})^2\ \mathrm{H}\ \underbrace{({}^{\mathrm{as}}\widetilde{\mathrm{A}_M}^{\mathrm{T}}\ {}^{\mathrm{as}}\widetilde{\mathrm{A}_M})^{-1}\ {}^{\mathrm{as}}\widetilde{\mathrm{A}_M}^{\mathrm{T}}\ {}^{\mathrm{as}}\widetilde{\mathrm{A}_M}}_{\mathrm{I}}\ ({}^{\mathrm{as}}\widetilde{\mathrm{A}_M}^{\mathrm{T}}\ {}^{\mathrm{as}}\widetilde{\mathrm{A}_M})^{-\mathrm{T}}\ \mathrm{H}^{\mathrm{T}}\\
&= ({}^{\mathrm{Du}}\sigma_{\widetilde{\mathcal{E}}_{\Delta X_M}})^2\ \mathrm{H}\ ({}^{\mathrm{as}}\widetilde{\mathrm{A}_M}^{\mathrm{T}}\ {}^{\mathrm{as}}\widetilde{\mathrm{A}_M})^{-1}\ \mathrm{H}^{\mathrm{T}}
\end{aligned} \tag{2.13}$$

Equation 2.13 presents the relationship that governs the scaling of uncertainty of measured deflections to uncertainty of resultant errors in estimated parameters. The goal is,

6. Note that all the elements of ${}^{\mathrm{Du}}\widetilde{\mathcal{E}}_{\Delta X_M}$ have the same standard deviation. Therefore, ${}^{\mathrm{Du}}\sigma_{\widetilde{\mathcal{E}}_{\Delta X_M}}$ is a scalar value.

7. See section 1.2.2 to know more about this.

however, to find the relationship governing scaling of uncertainty of measured deflections to uncertainty of resultant errors in compensation. Hence, it is necessary to understand the propagation of errors in estimated parameters to compensation errors.

The parameters identified are used to predict the necessary actuator displacements, q_C, that ensures that the end-effector/platform reaches the desired pose X_D after undergoing deflection due to an applied load F_D. Let X_C be the pose array corresponding to q_C considering zero deflection due to load. X_C is the pose array that needs to be entered into the control interface of a robot's controller that doesn't have the compliance error model embedded in it. Let X_C be called "*command pose*". X_C is estimated using the formula

$$X_D = X_C + \Delta X_C \tag{2.14}$$

Here, ΔX_C is the deflection at pose X_C due to a load ΔF_D. The initial load on the end-effector/platform, which is the load on the platform for which the $X_D = X_C$, is considered zero. The solution to X_C in equation 2.14 needs to be found so that the robot's platform/end-effector reaches (close to) the desired pose.

In reality, however, the predicted command pose will have errors due to errors in estimated parameters. This can be expressed as

$$\widehat{X_C} = X_D - \widehat{\Delta X_C} \tag{2.15}$$

where $\widehat{X_C}$ is the predicted command pose with error and $\widehat{\Delta X_C}$ is the predicted deflection with error at pose $\widehat{X_C}$ and load ΔF_D. $\widehat{X_C}$ and $\widehat{\Delta X_C}$ are given by

$$\widehat{X_C} = X_C + {}^{DU}\varepsilon_{X_C} + {}^{FE}\varepsilon_{X_C} \tag{2.16}$$

$$\widehat{\Delta X_C} = \Delta X_C + {}^{DU}\varepsilon_{\Delta X_C} + {}^{FE}\varepsilon_{\Delta X_C} \tag{2.17}$$

$$\widehat{\Delta X_C} = \widehat{A_C}\,\widehat{c} \tag{2.18}$$

Here, ${}^{\mathrm{DU}}\mathcal{E}_{\Delta X_C}$ and ${}^{\mathrm{FE}}\mathcal{E}_{\Delta X_C}$ are the components of error in predicted deflection $\widehat{\Delta X_C}$ as a result of ${}^{\mathrm{DU}}\mathcal{E}_c$ and ${}^{\mathrm{FE}}\mathcal{E}_c$, respectively. ${}^{\mathrm{DU}}\mathcal{E}_{X_C}$ and ${}^{\mathrm{FE}}\mathcal{E}_{X_C}$ are the components of error in predicted command pose as a consequence of ${}^{\mathrm{DU}}\mathcal{E}_{\Delta X_C}$ and ${}^{\mathrm{FE}}\mathcal{E}_{\Delta X_C}$, respectively. Matrix $\widehat{A_C}$ is a function of $\widehat{X_C}$ and ΔF_D.

The robot's end-effector/platform attains a pose X_A after elastostatic error compensation and this is equal to X_D when there are no parameter errors. Therefore, the following expression can be written:

$$X_A = X_C + \Delta X_C = X_D \tag{2.19}$$

In the presence of errors in estimated parameters, however, the platform reaches a different pose $\widehat{X_A}$. The following can then be written:

$$\widehat{X_A} = \widehat{X_C} + {}^{\mathrm{ac}}\Delta X_C \tag{2.20}$$

Here, ${}^{\mathrm{ac}}\Delta X_C$ is the actual deflection of the end-effector/platform at the pose $\widehat{X_C}$ as a result of actual stiffness parameters (c) and applied load ΔF_D.

Now, the following expression can be obtained using equations 2.20 and 2.15:

$$\widehat{X_A} = X_D - \widehat{\Delta X_C} + {}^{\mathrm{ac}}\Delta X_C \tag{2.21}$$

Equation 2.21 can be expanded to obtain

$$X_A + {}^{\mathrm{DU}}\mathcal{E}_{X_A} + {}^{\mathrm{FE}}\mathcal{E}_{X_A} = X_D - \left(\Delta X_C + {}^{\mathrm{DU}}\mathcal{E}_{\Delta X_C} + {}^{\mathrm{FE}}\mathcal{E}_{\Delta X_C}\right) + {}^{\mathrm{ac}}\Delta X_C \tag{2.22}$$

In equation 2.22, ${}^{\mathrm{DU}}\mathcal{E}_{X_A}$ and ${}^{\mathrm{FE}}\mathcal{E}_{X_A}$ are the errors in pose attained after compensation as a consequence of ${}^{\mathrm{DU}}\mathcal{E}_{\Delta X_C}$ and ${}^{\mathrm{FE}}\mathcal{E}_{\Delta X_C}$, respectively. ${}^{\mathrm{DU}}\mathcal{E}_{\Delta X_C}$ and ${}^{\mathrm{FE}}\mathcal{E}_{\Delta X_C}$ are, in turn,

a consequence of ${}^{\mathrm{DU}}\mathcal{E}_c$ and ${}^{\mathrm{FE}}\mathcal{E}_c$, respectively. ${}^{\mathrm{DU}}\mathcal{E}_{\Delta X_C}$ and ${}^{\mathrm{FE}}\mathcal{E}_{\Delta X_C}$ can be expressed as

$$ {}^{\mathrm{DU}}\mathcal{E}_{\Delta X_C} = \widehat{A_C}\ {}^{\mathrm{DU}}\mathcal{E}_c \tag{2.23} $$

$$ {}^{\mathrm{FE}}\mathcal{E}_{\Delta X_C} = \widehat{A_C}\ {}^{\mathrm{FE}}\mathcal{E}_c \tag{2.24} $$

Furthermore, the following can also be written:

$$ \Delta X_C = A_C\, c \approx \widehat{A_C}\, c = {}^{ac}\Delta X_C \tag{2.25} $$

Note that A_C is a function of X_C and F_D while $\widehat{A_C}$ is a function of $\widehat{X_C}$ and F_D. X_C and $\widehat{X_C}$ need to be very close in the workspace for equation 2.25 to be true. X_C and $\widehat{X_C}$ will indeed be very close in the workspace unless: (a) the errors in measurements are very high relative to the level of positioning precision required[8], and/or (b) the force/moment assumed to have been applied at the end-effector/platform during positioning is very different from the force/moment actually applied. These two reasons are assumed to be untrue. Hence, X_C and $\widehat{X_C}$ can be assumed to be close and consequently, equation 2.25 can be assumed to be valid. Simlarly, X_D and X_C will also be very close in the workspace. The following can then be written:

$$ \Delta X_C = A_C\, c \approx A_D\, c = \Delta X_D \tag{2.26} $$

Here, A_D is a function of X_D and F_D. Now, using equation 2.22 and that $X_A = X_D$ (see equation 2.19) and $\Delta X_C \approx {}^{ac}\Delta X_C$ (see equation 2.25), the following expression can be obtained:

$$ {}^{\mathrm{DU}}\mathcal{E}_{X_A} \approx -\,{}^{\mathrm{DU}}\mathcal{E}_{\Delta X_C} \tag{2.27} $$

8. When, for example, the required positioning precision is in microns and the errors in measurements are in centimeters.

Finally, the covariance matrix of ${}^{Du}\mathcal{E}_{X_A}$ can be derived which will be useful in evaluating the influence of uncertainty of measured deflections on the uncertainty of resultant compensation errors. Using equation 2.27, the following can be obtained:

$$\begin{aligned} Cov({}^{Du}\mathcal{E}_{X_A}) &\approx Cov({}^{Du}\mathcal{E}_{\Delta X_C}) \\ &\approx Cov(A_C\,{}^{Du}\mathcal{E}_c) \end{aligned} \tag{2.28}$$

Since, A_D and A_C are approximately equal, equation 2.28 can be further expanded as

$$\begin{aligned} Cov({}^{Du}\mathcal{E}_{X_A}) &\approx Cov(A_D\,{}^{Du}\mathcal{E}_c) \\ &\approx A_D\,Cov({}^{Du}\mathcal{E}_c)\,A_D^T \end{aligned} \tag{2.29}$$

Finally, equations 2.29 and 2.13 lead to the following expression:

$$Cov({}^{Du}\mathcal{E}_{X_A}) \approx ({}^{Du}\sigma_{\widetilde{\mathcal{E}}_{\Delta X_M}})^2 \underbrace{A_D\,H\,({}^{as}\widetilde{\overline{A_M}}^T\,{}^{as}\widetilde{\overline{A_M}})^{-1}\,H^T\,A_D^T}_{U} \tag{2.30}$$

Equation 2.30 presents the relationship that governs the propagation of uncertainty in measured deflections to uncertainty of resultant errors in pose attained after compensation. In this, matrix U contains the scaling factors that scale ${}^{Du}\sigma^2_{\widetilde{\mathcal{E}}_{\Delta X_M}}$ to respective elements of $Cov({}^{Du}\mathcal{E}_{X_A})$. U is a function of the poses and forces/moments used for stiffness identification. Hence, U can be used as a medium to evaluate the influence of poses and forces/moments used for stiffness identification on the propagation of uncertainty from deflection measurements to resultant compensation errors. Section 2.3.2 discusses about the appropriate usage of the relationship of equation 2.30 to identify the set of poses and forces/moments for stiffness identification which are best suited for the application at hand.

2.3.2 Formulation of DUIR criterion

As seen in equation 2.30, matrix U controls the propagation of uncertainty in measured deflections to uncertainty of resultant compensation errors. Hence, relevant components of U must be minimized in order to optimize stiffness identification in a way that is best for a given application at hand. The diagonal elements of U scale ${}^{\mathrm{Du}}\sigma^2_{\widetilde{\varepsilon}_{\Delta X_M}}$ to the variances of the respective elements of ${}^{\mathrm{Du}}\varepsilon_{X_A}$. Minimizing the first diagonal element of U, for example, will ensure that variance of first element of ${}^{\mathrm{Du}}\varepsilon_{X_A}$ will be the least possible for a given ${}^{\mathrm{Du}}\sigma_{\widetilde{\varepsilon}_{\Delta X_M}}$. When best positioning performance is needed along multiple axes of the robot's end-effector/platform, multiple diagonal elements of U must be minimized. This can be done using a multi-objective optimization approach or by minimizing some combination of the diagonal elements of U.

When the robot's end-effector/platform pose coordinates have both translations and rotations, the diagonal elements of U correspond to translational and rotational elements. Consequently, if the diagonal elements of U need to be compared in an optimization procedure, the issue of non-homogeneous comparison arises. This is because comparing the diagonal elements of U corresponding to translational coordinates of ${}^{\mathrm{Du}}\varepsilon_{X_A}$ with the diagonal elements of U corresponding to rotational coordinates of ${}^{\mathrm{Du}}\varepsilon_{X_A}$ is not valid. To solve this issue, equation 2.30 can be split into two: one concerned only to the translational elements of ${}^{\mathrm{Du}}\varepsilon_{X_A}$ and the other concerned only to rotational elements of ${}^{\mathrm{Du}}\varepsilon_{X_A}$. They can be written as

$$\mathrm{Cov}({}^{\mathrm{Du,t}}\varepsilon_{X_A}) \approx ({}^{\mathrm{Du}}\sigma_{\widetilde{\varepsilon}_{\Delta X_M}})^2 \; {}^{\mathrm{t}}A_D \; H \; ({}^{as}\widetilde{\widetilde{A_M}}^T \; {}^{as}\widetilde{\widetilde{A_M}})^{-1} \; H^T \; {}^{\mathrm{t}}A_D^T \tag{2.31}$$

$$\mathrm{Cov}({}^{\mathrm{Du,r}}\varepsilon_{X_A}) \approx ({}^{\mathrm{Du}}\sigma_{\widetilde{\varepsilon}_{\Delta X_M}})^2 \; {}^{\mathrm{r}}A_D \; H \; ({}^{as}\widetilde{\widetilde{A_M}}^T \; {}^{as}\widetilde{\widetilde{A_M}})^{-1} \; H^T \; {}^{\mathrm{r}}A_D^T \tag{2.32}$$

In equation 2.31, ${}^{\mathrm{Du,t}}\varepsilon_{X_A}$ contains the translational components of ${}^{\mathrm{Du}}\varepsilon_{X_A}$. Similarly, in equation 2.32, ${}^{\mathrm{Du,r}}\varepsilon_{X_A}$ contains the rotational components of ${}^{\mathrm{Du}}\varepsilon_{X_A}$. ${}^{\mathrm{r}}A_D$ and ${}^{\mathrm{t}}A_D$ are the rows of A_D corresponding to the rotational and translational elements of ΔX_D, re-

spectively. ${}^{t}A_D$ and ${}^{r}A_D$ are related to their respective elements of ΔX_D, $\Delta X_D{}^{t}$ and $\Delta X_D{}^{r}$, respectively, as

$$\overbrace{\begin{bmatrix} {}^{t}A_D \\ {}^{r}A_D \end{bmatrix}}^{A_D} c = \overbrace{\begin{bmatrix} \Delta X_D{}^{t} \\ \Delta X_D{}^{r} \end{bmatrix}}^{\Delta X_D} \tag{2.33}$$

Furthermore, some applications can demand for minimization of positioning error after compensation in terms of translational distance (Euclidean norm). Appendix E shows the relationship between the RMS value of possible Euclidean norms of ${}^{Du,t}\varepsilon_{X_A}$, denoted as ${}^{Du}\rho$, and $Cov({}^{Du,t}\varepsilon_{X_A})$. In equation E.7 of Appendix E, it can be seen that ${}^{Du}\Omega$ from E.6 is a scalar that is directly proportional to ${}^{Du}\rho$ and it is dependent on the measurement conditions (poses and forces/moments used for stiffness identification). Therefore, choosing appropriate poses and forces/moments for stiffness identification that minimizes ${}^{Du}\Omega$ will minimize the RMS value of possible Euclidean norms of ${}^{Du,t}\varepsilon_{X_A}$. It must be noted here that this criterion is similar to O_{TP} and O_{MV} (see table 1.1). When positioning at multiple poses and/or multiple loads needs to be optimized, multiple values of ${}^{Du}\Omega$ are obtained (one corresponding to each positioning case). A multi-objective optimization to minimize the multiple values of ${}^{Du}\Omega$ can then be done. Alternately, some combination of the values of ${}^{Du}\Omega$ can be minimized.

2.4 Minimizing the influence of applied force/moment error on positioning error after compensation (FEIR criterion)

2.4.1 Relationship between applied force/moment error and resultant positioning error after compensation

In order to derive the necessary relationship, the expression relating errors in forces/-moments applied during stiffness identification and the resultant errors in estimated pa-

rameters can be obtained first. Equation 2.6 can be used to obtain this expression and it can be written as

$$G\ {}^{as}A_M\ H\ H^{-1}\ {}^{FE}\mathcal{E}_c = G\ {}^{FE}\mathcal{E}_{\Delta X_M} \tag{2.34}$$

Furthermore, the following expression can also be written:

$${}^{as}_{ij}\Delta F_M = {}_iJ^{-T}\ K\ {}_i\check{J}^{-1}\ \Delta X_M{}^{ij} \tag{2.35}$$

In equation 2.35, $\Delta X_M{}^{ij}$ is the j^{th} deflection measurement performed at the i^{th} measurement pose, X^i_M. ${}_iJ$ and ${}_i\check{J}$ are the Jacobians corresponding to X^i_M.

Any error in the load applied on the platform leads to an error in the measured deflection. Therefore, the following can be written:

$${}^{as}_{ij}\Delta F_M + {}_{ij}\mathcal{E}_{\Delta F_M} = {}_iJ^{-T}\ K\ {}_i\check{J}^{-1}(\Delta X_M{}^{ij} + {}^{FE}_{ij}\mathcal{E}_{\Delta X_M}) \tag{2.36}$$

In equation 2.36, ${}^{FE}_{ij}\mathcal{E}_{\Delta X_M}$ is the error corresponding to $\Delta X_M{}^{ij}$ due to the applied force/moment error ${}_{ij}\mathcal{E}_{\Delta F_M}$. Equations 2.36 and 2.35 give

$${}_{ij}\mathcal{E}_{\Delta F_M} = {}_iJ^{-T}\ K\ {}_i\check{J}^{-1}\ {}^{FE}_{ij}\mathcal{E}_{\Delta X_M} \tag{2.37}$$

Equation 2.37 can be rewritten as

$${}^{FE}_{ij}\mathcal{E}_{\Delta X_M} = \underbrace{{}_i\check{J}\ K^{-1}\ {}_iJ^T}_{{}_iD}\ {}_{ij}\mathcal{E}_{\Delta F_M} \tag{2.38}$$

Equation 2.38 leads to the following expression:

$$
{}^{FE}\mathcal{E}_{\Delta X_M} = \overbrace{\begin{bmatrix} {}_1D & & & \\ & {}_1D & 0 & \\ & & \ddots & \\ & & & {}_2D \\ & 0 & & \ddots \\ & & & & \ddots \end{bmatrix}}^{D} \mathcal{E}_{\Delta F_M} \tag{2.39}
$$

Substituting for ${}^{FE}\mathcal{E}_{\Delta X_M}$ from equation 2.39 in equation 2.34 leads to

$$
G\ {}^{as}A_M\ H\ H^{-1}\ {}^{FE}\mathcal{E}_c = G\ D\ \mathcal{E}_{\Delta F_M} \tag{2.40}
$$

Equation 2.40 can be rewritten as

$$
{}^{FE}\mathcal{E}_c = H\ {}^{as}\widetilde{\overline{A_M}}^{+}\ G\ D\ \mathcal{E}_{\Delta F_M} \tag{2.41}
$$

Equation 2.41 can be used to evaluate the effect of $\mathcal{E}_{\Delta F_M}$ on ${}^{FE}\mathcal{E}_c$. However, matrix D is not known a priori since K (matrix containing stiffness parameters to be estimated) is not known a priori. Consequently, a preliminary test must be performed to obtain the matrix containing approximate values of stiffness parameter values, ${}^{ap}K$. The following expressions can then be written:

$$
{}^{ap}_{i}D = {}_i\check{J}\ {}^{ap}K^{-1}\ {}_iJ^T \tag{2.42}
$$

$$
{}^{ap}D = diag({}^{ap}_{1}D\ {}^{ap}_{1}D \ldots {}^{ap}_{2}D \ldots) \tag{2.43}
$$

${}^{ap}D$ is the matrix D formulated using ${}^{ap}K$. Equation 2.41 can then be rewritten as

$$
{}^{FE}\mathcal{E}_c = H\ {}^{as}\widetilde{\overline{A_M}}^{+}\ G\ {}^{ap}D\ \mathcal{E}_{\Delta F_M} \tag{2.44}
$$

Equations 2.15, 2.16 and 2.17 give

$$X_C + {}^{DU}\mathcal{E}_{X_C} + {}^{FE}\mathcal{E}_{X_C} = X_D - (\Delta X_C + {}^{DU}\mathcal{E}_{\Delta X_C} + {}^{FE}\mathcal{E}_{\Delta X_C}) \tag{2.45}$$

Following from the definitions of ${}^{DU}\mathcal{E}_{X_C}$, ${}^{FE}\mathcal{E}_{X_C}$, ${}^{DU}\mathcal{E}_{\Delta X_C}$ and ${}^{FE}\mathcal{E}_{\Delta X_C}$ and equations 2.45 and 2.14, the following can be written:

$${}^{FE}\mathcal{E}_{X_C} = -{}^{FE}\mathcal{E}_{\Delta X_C} \tag{2.46}$$

Furthermore, equations 2.46, 2.18, 2.25, 2.26 and 2.6 give

$$\begin{aligned} {}^{FE}\mathcal{E}_{X_C} &= -\widehat{A_C}\,{}^{FE}\mathcal{E}_c \\ &\approx -A_D\,{}^{FE}\mathcal{E}_c \end{aligned} \tag{2.47}$$

Also, equations 2.47 and 2.44 give

$${}^{FE}\mathcal{E}_{X_C} \approx -A_D\, H\, {}^{as}\widetilde{\overline{A_M}}^{+}\, G\, {}^{ap}D\, \mathcal{E}_{\Delta F_M} \tag{2.48}$$

Additionally, equation 2.21 gives

$$X_A + {}^{DU}\mathcal{E}_{X_A} + {}^{FE}\mathcal{E}_{X_A} \approx X_C + {}^{DU}\mathcal{E}_{X_C} + {}^{FE}\mathcal{E}_{X_C} + \Delta X_D \tag{2.49}$$

In equation 2.49, ${}^{DU}\mathcal{E}_{X_A}$ and ${}^{FE}\mathcal{E}_{X_A}$ are the errors in pose attained after compensation as a consequence of ${}^{DU}\mathcal{E}_{X_C}$ and ${}^{FE}\mathcal{E}_{X_C}$, respectively. ${}^{DU}\mathcal{E}_{X_C}$ and ${}^{FE}\mathcal{E}_{X_C}$ are a consequence of ${}^{DU}\mathcal{E}_{\Delta X_C}$ and ${}^{FE}\mathcal{E}_{\Delta X_C}$ (see equation 2.45), respectively. Equation 2.49 is true because $\Delta X_D \approx {}^{ac}\Delta X_C$ (see equation 2.25 and 2.26).

Now, using equations 2.49 and 2.19 and from definitions of ${}^{DU}\mathcal{E}_{X_A}$, ${}^{FE}\mathcal{E}_{X_A}$, ${}^{DU}\mathcal{E}_{X_C}$ and ${}^{FE}\mathcal{E}_{X_C}$, the following can be written:

$${}^{FE}\mathcal{E}_{X_A} \approx {}^{FE}\mathcal{E}_{X_C} \tag{2.50}$$

Finally, equations 2.48 and 2.50 yield the necessary expression:

$$\begin{aligned} {}^{FE}\mathcal{E}_{X_A} &\approx -A_D\, H\, {}^{as}\widetilde{\overline{A_M}}^{+}\, G\, {}^{ap}D\, \mathcal{E}_{\Delta F_M} \\ &\approx -\underbrace{A_D\, {}^{as}A_M{}^{+}\, {}^{ap}D}_{Z}\, \mathcal{E}_{\Delta F_M} \end{aligned} \tag{2.51}$$

Equation 2.51 presents the relationship that governs the propagation of errors in applied force/moment during stiffness identification to the resultant errors in pose attained after compensation. The choice of poses and forces/moments for stiffness identification experiment changes matrix "Z" which in turn influences propagation of $\mathcal{E}_{\Delta F_M}$ to ${}^{FE}\mathcal{E}_{X_A}$. Z can be used as a medium to evaluate the influence of poses and forces/moments used for stiffness identification on the propagation of errors in applied force/moment during stiffness identification to the resultant errors in pose attained after compensation. Section 2.4.2 discusses about the appropriate usage of the relationship of equation 2.51 to identify the set of poses and forces/moments for stiffness identification which are best suited for an application at hand.

2.4.2 Formulation of FEIR criterion

As can be seen in equation 2.51, matrix Z controls the propagation of errors in forces/-moments applied for stiffness identification to the resultant errors in pose attained after compensation. Hence, relevant components of Z must be minimized in order to optimize stiffness identification in a way that is best for a given application at hand. For example, when best performance is required along the first axis of the end-effector/platform (first element of X_D) at the desired target pose, the first element of ${}^{FE}\mathcal{E}_{X_A}$ must be minimized. When no prior information about the errors in applied forces/moments is available, for example when force/moment is manually applied without measuring it, it is best to minimize all the elements of first row of Z. One way to do this is to minimize the 2-norm of the first row of Z. Sometimes, even when the load is applied manually without measuring it, the user can have an idea as to which element(s) of $\mathcal{E}_{\Delta F_M}$ might acquire high values. This

can be evident due to the nature of loading[9]. Consequently, the corresponding elements of matrix Z can be minimized.

When the applied load is measured using some force measurement instrument, the uncertainty of these measurements are usually specified by the instrument's supplier. This information can be helpful in optimizing stiffness identification. Equation 2.51 can be used to get the following expression:

$$\mathrm{Cov}\left({}^{\mathrm{FE}}\mathcal{E}_{X_A}\right) \approx Z\,\mathrm{Cov}\left(\mathcal{E}_{\Delta F_M}\right) Z^T \tag{2.52}$$

When the uncertainties of force measurements are known, $\mathrm{Cov}\left(\mathcal{E}_{\Delta F_M}\right)$ can be deduced. The concerned elements of $Z\,\mathrm{Cov}\left(\mathcal{E}_{\Delta F_M}\right) Z^T$ can then be minimized as per the requirement of the application. $Z\,\mathrm{Cov}\left(\mathcal{E}_{\Delta F_M}\right) Z^T$ has a structure similar to any covariance matrix. The variances of the individual elements of ${}^{\mathrm{FE}}\mathcal{E}_{X_A}$ are along its diagonal while the off-diagonal elements correspond to correlations between elements of the vector ${}^{\mathrm{FE}}\mathcal{E}_{X_A}$. Therefore, the diagonal elements of $Z\,\mathrm{Cov}\left(\mathcal{E}_{\Delta F_M}\right) Z^T$ decide the variances along the corresponding elements of ${}^{\mathrm{FE}}\mathcal{E}_{X_A}$. Minimizing the first diagonal element of $Z\,\mathrm{Cov}\left(\mathcal{E}_{\Delta F_M}\right) Z^T$, for example, will ensure that variance of first element of ${}^{\mathrm{FE}}\mathcal{E}_{X_A}$ will be the least possible for a given $\mathrm{Cov}\left(\mathcal{E}_{\Delta F_M}\right)$. When best positioning performance is needed along multiple axes of the robot's end-effector/platform, multiple diagonal elements of $Z\,\mathrm{Cov}\left(\mathcal{E}_{\Delta F_M}\right) Z^T$ must be minimized using a multi-objective optimization approach or by minimizing some combination of its diagonal elements.

When the robot's end-effector/platform pose coordinates have both translations and rotations, care must be taken while comparing elements of Z or $Z\,\mathrm{Cov}\left(\mathcal{E}_{\Delta F_M}\right) Z^T$. This is because comparing variances of rotational coordinates (or scaling factors corresponding to thereof) with their translational counterparts is not valid. To solve this issue, separate relationships corresponding to the rotational and translational coordinates of the

9. For example, in the loading case for stiffness identification in Appendix D, moment errors about the X and Y axes of the robot's platform can be expected due to the nature of loading.

end-effector/platform pose vector can be used. Equations 2.51 and 2.52 can be used to get the following expressions:

$$^{FE,r}\mathcal{E}_{X_A} \approx -\overbrace{{}^{r}A_D\ {}^{as}A_M{}^{+\ ap}D}^{{}^{r}Z}\ \mathcal{E}_{\Delta F_M} \tag{2.53}$$

$$^{FE,t}\mathcal{E}_{X_A} \approx -\overbrace{{}^{t}A_D\ {}^{as}A_M{}^{+\ ap}D}^{{}^{t}Z}\ \mathcal{E}_{\Delta F_M} \tag{2.54}$$

$$Cov\left(^{FE,r}\mathcal{E}_{X_A}\right) \approx {}^{r}Z\ Cov\left(\mathcal{E}_{\Delta F_M}\right)\ {}^{r}Z^{T} \tag{2.55}$$

$$Cov\left(^{FE,t}\mathcal{E}_{X_A}\right) \approx {}^{t}Z\ Cov\left(\mathcal{E}_{\Delta F_M}\right)\ {}^{t}Z^{T} \tag{2.56}$$

In the above equations, $^{FE,t}\mathcal{E}_{X_A}$ and $^{FE,r}\mathcal{E}_{X_A}$ are the translational and rotational components of $^{FE}\mathcal{E}_{X_A}$, respectively. ${}^{t}Z$ and ${}^{r}Z$ are the rows of Z corresponding to $^{FE,t}\mathcal{E}_{X_A}$ and $^{FE,r}\mathcal{E}_{X_A}$, respectively.

Furthermore, some applications demand for minimization of positioning error after compensation in terms of translational distance (Euclidean norm). In such cases, another set of expressions can be useful to formulate FEIR criterion. When the variance of expected force/moment error is not known, the relationship between the norm of $^{FE,t}\mathcal{E}_{X_A}$ and the error in applied force/moment can be useful. This expression can be obtained using equation 2.54 in the following form [10]:

$$\|\,^{FE,t}\mathcal{E}_{X_A}\|_2 \approx \|-{}^{t}Z\ \mathcal{E}_{\Delta F_M}\|_2 \leq \|-{}^{t}Z\|_2\ \|\mathcal{E}_{\Delta F_M}\|_2 \tag{2.57}$$

It can be seen in equation 2.57 that minimizing $\|-{}^{t}Z\|_2$ minimizes the influence of errors in applied forces/moments on the resultant distance error after compensation.

10. This follows from the inequality $\|\mathcal{A}\ \mathcal{X}\|_2 \leq \|\mathcal{A}\|_2\ \|\mathcal{X}\|_2$ for any $m \times n$ matrix $\mathcal{A}$ and n-vector $\mathcal{X}$ (refer chapter 9 of [Seber and Lee, 2012]).

When the variance of the expected force/moment error is known[11], the expression derived in Appendix F can be useful. In this, the relationship between the RMS value of possible Euclidean norms of ${}^{FE,t}\mathcal{E}_{X_A}$, denoted as ${}^{FE}\rho$, and $Cov({}^{FE,t}\mathcal{E}_{X_A})$ is shown. In Appendix F, it can be seen that[12] $tr\left({}^{t}Z\, Cov(\mathcal{E}_{\Delta F_M})\, {}^{t}Z^T\right)$ is equal to ${}^{FE}\rho$ and the value of $tr\left({}^{t}Z\, Cov(\mathcal{E}_{\Delta F_M})\, {}^{t}Z^T\right)$ is dependent on the measurement conditions (poses and forces/-moments used for stiffness identification). Consequently, choosing poses and forces/moments for stiffness identification that minimize $tr\left({}^{t}Z\, Cov(\mathcal{E}_{\Delta F_M})\, {}^{t}Z^T\right)$ will minimize the RMS value of possible Euclidean norms of ${}^{FE,t}\mathcal{E}_{X_A}$. When positioning at multiple poses and/or multiple loads needs to be optimized, multiple values of $tr\left({}^{t}Z\, Cov(\mathcal{E}_{\Delta F_M})\, {}^{t}Z^T\right)$ are obtained (one corresponding to each positioning case). Consequently, multiples values of $tr\left({}^{t}Z\, Cov(\mathcal{E}_{\Delta F_M})\, {}^{t}Z^T\right)$ must be minimized. This can be accomplished using a multi-objective optimization approach or by minimizing some combination of those values.

2.5 Conclusion

This chapter presented a stiffness identification optimization framework that counters the limitations of the existing criteria for the same, which were presented in chapter 1. To accomplish this, a reformulated stiffness identification problem was firstly presented. This reformulated stiffness identification problem considers the influence of two error sources impacting stiffness identification: the errors in forces/moments applied during stiffness identification experiment and the uncertainty of deflection measurements performed. This is unlike previous works as they ignored the former source of error. This was followed by derivation of relationships that relate the errors impacting stiffness identification to the resultant pose errors after compensation. Discussion was then provided on the usage of the presented relationships to formulate necessary criterion/criteria for best stiffness identification depending on the specifications of the application at hand.

11. For example, when the force/moment applied is measured using an instrument and the uncertainty of the measurements made using this instrument is known.
12. Note here that $tr()$ denotes the trace of the corresponding matrix.

CHAPTER

3 Validation of developed techniques using simulated elastostatic calibrations of a bipod

Contents

Chapter Abstract

This chapter aims at validating the efficacy of stiffness identification optimization framework presented in chapter 2. This is achieved using simulated elastostatic calibrations of a bipod. Three simulation studies are presented which validate the efficacy of using: (a) DUIR criterion[1], (b) FEIR criterion[2], and (c) both criteria together, to select best poses and forces for stiffness identification. Results of these simulation studies confirm the efficacy of the presented stiffness identification optimization framework.

1. This criterion can be formulated using the presented stiffness identification optimization framework. It minimizes the influence of uncertainty of deflection measurements (performed for stiffness identification) on the compensation quality.

2. This criterion can be formulated using the presented stiffness identification optimization framework. It minimizes the influence of errors in forces applied for stiffness identification on the compensation quality.

3.1 Introduction

This chapter presents simulation studies performed on a planar bipod to evaluate the efficacy of the presented stiffness identification optimization framework. This mechanism was chosen for these simulation studies to facilitate ease of analysis of results as this mechanism is simple.

Three simulation studies are presented in this chapter. In these studies, elastostatic calibrations of a bipod are simulated. In the first simulation study, elastostatic calibrations are simulated with only deflection measurement uncertainty influencing stiffness identifications. The performances of stiffness identification measurement conditions (poses and forces) selected using DUIR criterion and various previously proposed criteria [3] are then compared. In the second simulation study, elastostatic calibrations are simulated in which stiffness identifications are influenced only by errors in forces applied. These are used to evaluate the ability of FEIR criterion to recommend stiffness identification measurement conditions which minimize the influence of these errors on compensation quality. In the third and the last simulation study, errors from both sources [4] influence the simulated stiffness identifications. These are then used to evaluate the efficacy of using DUIR and FEIR criteria together to select best set of poses and forces for stiffness identification.

This chapter is organized as follows: section 3.2 describes the assumed mechanism, its kinematics and its stiffness model. Sections 3.3, 3.4 and 3.5 present the details and results of the three simulation studies. Finally, section 3.6 presents the conclusion of this chapter.

3.2 Mechanism description, kinematics and stiffness model

Figure 3.1 shows the bipod under study and its assumed dimensions. This bipod is assumed to be driven using two prismatic actuators as shown in the figure. This bipod is assumed to have a simple workspace, as shown in figure 3.1, for ease of analysis. The compliance is assumed to exist only in the actuated joints and the rest of the structure

3. For minimizing the influence of deflection measurement uncertainty on stiffness identification.
4. Deflection measurement uncertainty and errors in forces applied.

is assumed to be rigid. The stiffness of each of the two actuated joints is assumed to be 10 N/μm. Also, the joints of this mechanism are assumed to be frictionless and the legs are assumed to have negligible mass.

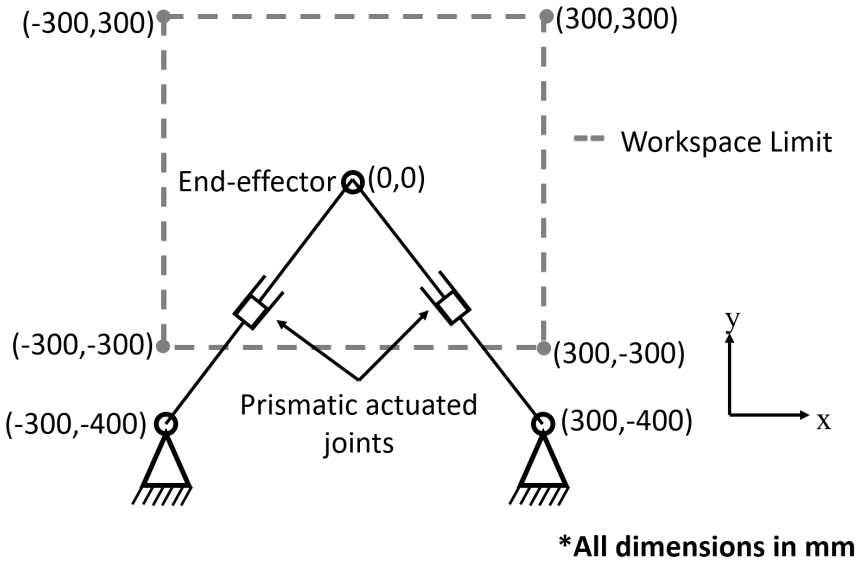

Figure 3.1: Schematic of the bipod under study

The end-effector position vector, ${}_B\mathrm{X}$, defines the position of the end-effector with respect to its position when the bipod has the configuration as in figure 3.1. ${}_B\mathrm{q}$ contains the lengths of the prismatic links and is written as

$$ {}_B\mathrm{q} = [{}_B\mathrm{q}_1 \; {}_B\mathrm{q}_2]^T \tag{3.1} $$

The relationship between the velocity of the end-effector and those of the actuated joints is given by

$$ {}_B\eta = {}_B\mathrm{J} \, {}_B\dot{\mathrm{q}} \tag{3.2} $$

Here, ${}_B\eta$ is the end-effector's velocity vector, ${}_B\dot{\mathrm{q}}$ contains the velocities of the actuators and ${}_B\mathrm{J}$ is the Jacobian matrix. The equation relating the differential position vector (${}_B\Delta X$)

and the differential actuator position vector (${}_B\Delta q$), as in equation 1.13, can be written for this case as

$$ {}_B\Delta q = {}_B J^{-1}\, {}_B\Delta X \tag{3.3} $$

Note that the relationship in equation 3.3 contains the normal Jacobian matrix ${}_B J$ instead of a modified Jacobian matrix as in equation 1.13. This is because the end-effector pose coordinates have less than two rotational degrees of freedom (zero in this case).

A simple lumped stiffness model (shown in figure 3.2) was used to model the static stiffness characteristics of this mechanism. One spring is used to model the stiffness of each leg (${}_B k_{i=1,2}$). This modelling method is consistent with the method described in chapter 1.

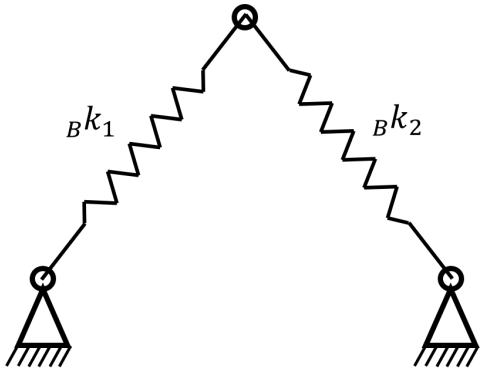

Figure 3.2: Lumped stiffness model of the bipod under study

The Cartesian stiffness matrix (as in equation 1.15), ${}_B K_C$, for this bipod can be written as

$$ {}_B K_C = {}_B J^{-T}\, {}_B K\, {}_B J^{-1} \tag{3.4} $$

where matrix ${}_B K$ is diagonal matrix with leg stiffnesses forming its diagonal elements. It is given by

$$ {}_B K = \begin{bmatrix} {}_B k_1 & 0 \\ 0 & {}_B k_2 \end{bmatrix} \tag{3.5} $$

The Cartesian stiffness matrix ${}_{B}K_{C}$ relates the differential force vector (${}_{B}\Delta F$) and the differential position vector (${}_{B}\Delta X$) as

$$ {}_{B}\Delta F = {}_{B}K_{C}\ {}_{B}\Delta X \tag{3.6} $$

Rearrangement of this equation yields the relationship similar to equation 1.17:

$$ {}_{B}A\ {}_{B}c = {}_{B}\Delta X \tag{3.7} $$

Here, ${}_{B}A$ is the *observation matrix* and it is given by

$$ {}_{B}A_{ij} = {}_{B}J_{ij}\ \Big(\sum_{r=1}^{2}\ {}_{B}J_{rj}\ {}_{B}\Delta F_{r}\Big) \tag{3.8} $$

where ${}_{B}A_{ij}$ and ${}_{B}J_{ij}$ denote the j^{th} element of the i^{th} row of matrices ${}_{B}A$ and ${}_{B}J$, respectively. ${}_{B}\Delta F_{r}$ denotes the r^{th} element of vector ${}_{B}\Delta F$. ${}_{B}c$ is the vector with compliance parameters and is given by

$$ {}_{B}c = \Big[\frac{1}{{}_{B}k_{1}}\ \frac{1}{{}_{B}k_{2}}\Big]^{T} \tag{3.9} $$

3.3 Simulation study 1: validation of DUIR criterion

Consider a case in which elastostatic calibration of the bipod (figure 3.1) must be performed to position its end-effector precisely at a position ${}_{B1}X_{D} = [250; -250]$ mm with a force ${}_{B1}F_{D} = [0; -200]$ N applied on it. Assume that best possible positioning accuracy is desired only along the X-axis of the end-effector and that the positioning accuracy along its Y-axis is inconsequential. Also suppose that stiffness identification can be done at only one position using three deflection measurements and with a force of ${}_{B1}F_{M} = [0; -200]$ N applied at the end-effector. Let the uncertainty of position measurement system lead to independent deflection measurement uncertainties of 10 µm and 20 µm standard deviations along the end-effector's X and Y axes, respectively. Furthermore, let the errors in

forces applied during stiffness identification be zero in this case. The best position for stiffness identification must, therefore, be selected to minimize the influence of deflection measurement uncertainty on positioning accuracy after compensation.

Since only uncertainty of measured deflections affects stiffness identification quality, DUIR criterion must be formulated to find the best position for stiffness identification in this case. For the sake of comparison, other previously proposed criteria[5] (O_1-O_5, O_{TP} and O_{MV}) can be used to find the best position for stiffness identification. To compare the performances of different identification positions, Monte-Carlo simulations were performed in which elastostatic calibrations of the bipod were simulated many times. Section 3.3.1 presents the details and results of stiffness identification optimization. The details and results of the validation simulations are then presented in section 3.3.2.

3.3.1 Stiffness identification optimization

The stiffness identification equation (equation 2.6) can be rewritten for this case as

$$ {}_{B1}G_U \, {}^{as}_{B1}A_M \, {}_{B1}H \, {}_{B1}H^{-1} \, ({}_{B1}c + {}^{Du}_{B1}\varepsilon_c) = {}_{B1}G_U \, ({}_{B1}\Delta X_M + {}^{Du}_{B1}\varepsilon_{\Delta X_M}) \tag{3.10} $$

Here, the left subscript "B1" specifies that the corresponding matrices/arrays of equation 2.6 have been formulated for this case. Since there is no applied force error, the corresponding terms of equation 2.6 do not exist in equation 3.10. ${}_{B1}G_U$ is a 6×6 matrix with inverse of deflection measurement standard deviations along its diagonal elements and is formulated as shown in equation 1.22. ${}_{B1}H$ is a 2×2 identity matrix because the expected magnitudes of estimated parameters are same. ${}_{B1}\Delta X_M$ and ${}^{Du}_{B1}\varepsilon_{\Delta X_M}$ are 6×1 vectors which together constitute the measured deflections. ${}^{Du}_{B1}\varepsilon_{\Delta X_M}$ contains the errors in measured deflections due to deflection measurement uncertainty. ${}^{as}_{B1}A_M$ is a 6×2 matrix which is a function of the forces assumed to be applied and the position used for stiffness identification. Parameter set of equation 3.10 is estimated using least squares method.

5. The criteria from theory of experiment design (ex: A-optimality, D-optimality, etc.) are not mentioned here because each of them has an equivalent *observability index* [Sun and Hollerbach, 2008].

Let ${}_{B1}\widehat{X_A}$ be the position attained after compensation in this case. U from equation 2.30 can be rewritten for this case as

$$ {}_{B1}U = {}_{B1}A_D \, {}_{B1}H \left(\overline{\widetilde{{}^{as}_{B1}A_M}}^{T} \overline{\widetilde{{}^{as}_{B1}A_M}} \right)^{-1} {}_{B1}H^T \, {}_{B1}A_D^T \tag{3.11} $$

Here, ${}_{B1}U$ and ${}_{B1}A_D$ are 2×2 matrices. ${}_{B1}A_D$ is a function of the target position and force applied at the end-effector during the intended positioning. The first diagonal element of ${}_{B1}U$, ${}_{B1}U_{11}$, is the scaling factor corresponding to variance along the X-axis of ${}_{B1}\widehat{X_A}$. Hence, the identification position which minimizes ${}_{B1}U_{11}$ must be found.

The plot of DUIR criterion formulated for this case, ${}_{B1}U_{11}$, varying across the allowed workspace is shown in figure 3.3. Also, figure 3.4 shows values of other position selection criteria (O_1-O_5, O_{TP} and O_{MV}) at positions across the workspace of the bipod. Note that O_{TP} and O_{MV} yield same values in this case. This is because these two criteria have same expressions when best positioning is desired at just one position (see table 1.1). Figure 3.5 shows the best position as per each criterion for this case.

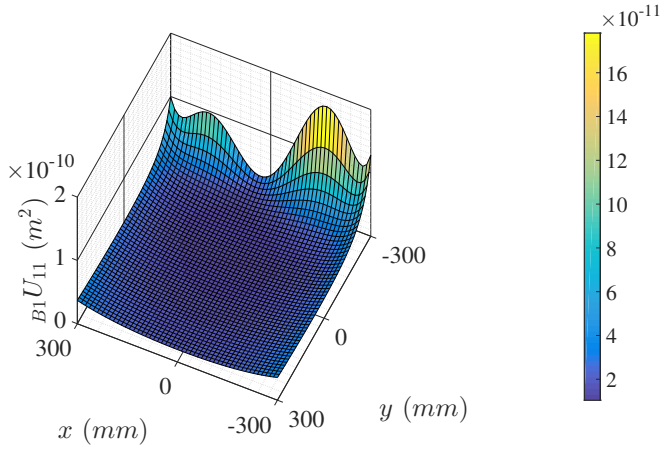

Figure 3.3: Plot showing values of DUIR criterion (${}_{B1}U_{11}$) for the elastostatic calibration of simulation study 1 (position having the lowest value of ${}_{B1}U_{11}$ is the best position for stiffness identification as per DUIR criterion in this case)

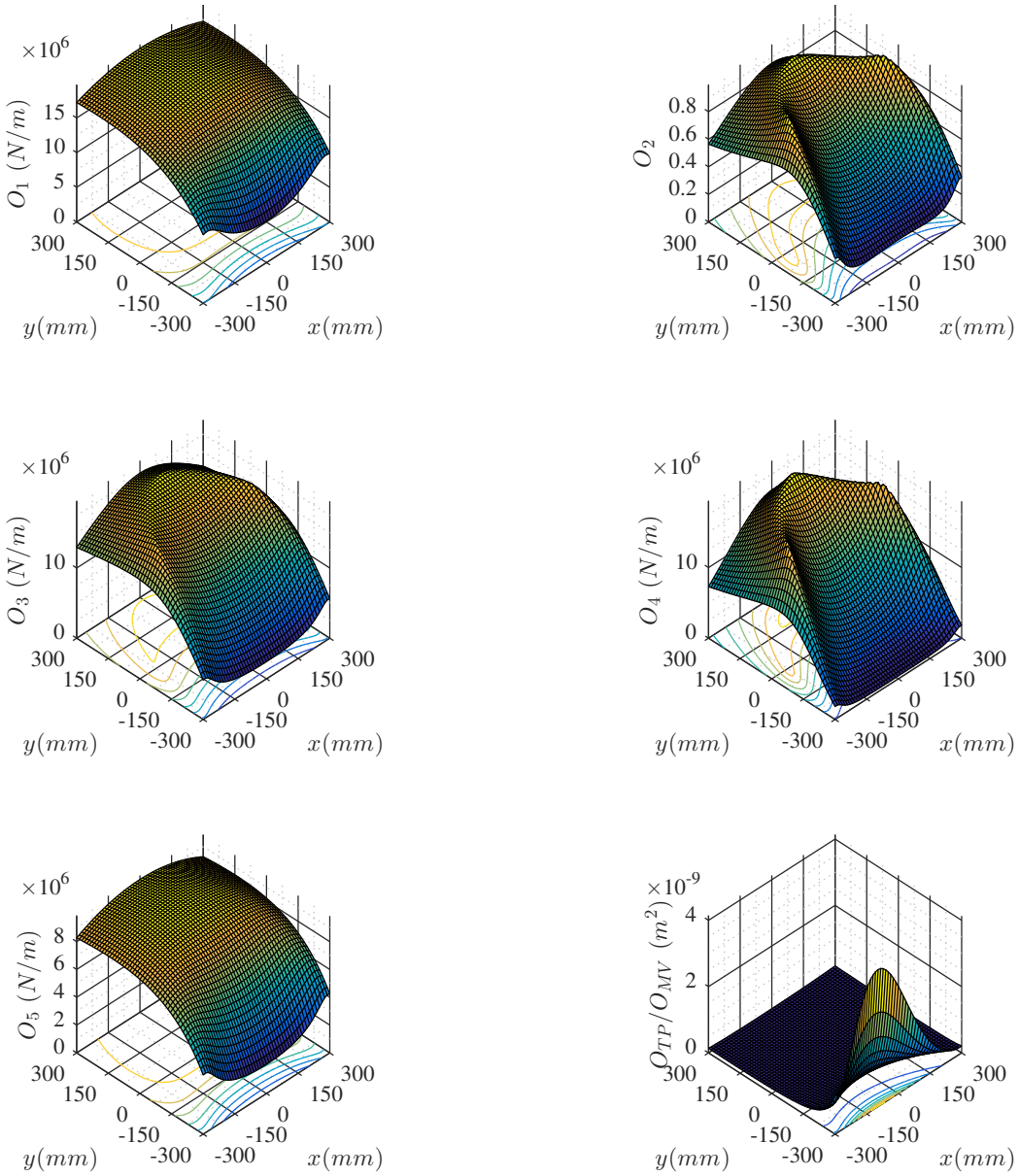

Figure 3.4: Plots showing values of O_1, O_2, O_3, O_4, O_5 and O_{TP}/O_{MV} for the elastostatic calibration of simulation study 1

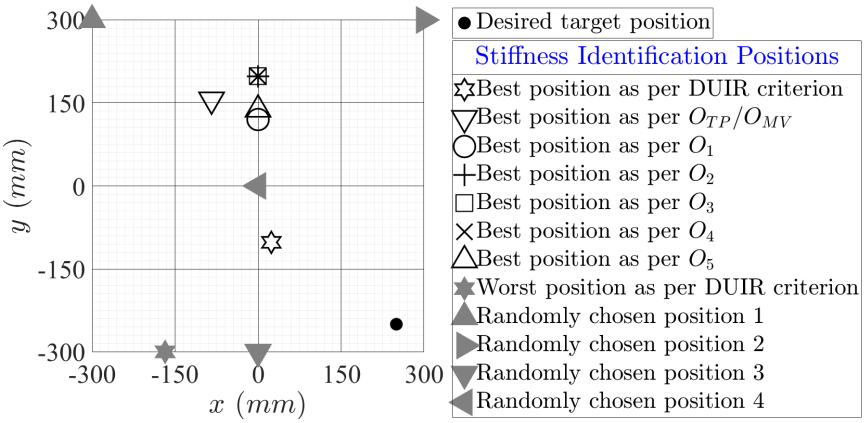

Figure 3.5: Plot showing different positions at which stiffness identifications were simulated in simulation study 1

3.3.2 Validation simulations

In order to validate the proposed criterion, Monte-Carlo simulations of simulated elastostatic calibrations were performed. Stiffness identification experiment was simulated 10000 times at each of the identification positions[6]. For the sake of comparison, stiffness identification experiments were also simulated at: (a) the desired target position, [250;−250] mm, (b) the worst position as per DUIR criterion, and (c) four other randomly chosen positions (see figure 3.5). During each trial of simulated stiffness identification, a different measured deflection error was supplied and they varied as per the assumed standard deviations: 10 µm and 20 µm standard deviations along X and Y axes, respectively. The estimated parameter set in each trial was used to simulate the compensation. The standard deviations of errors in positions attained after these simulated compensations can be used to evaluate the quality of each identification position. Figure 3.6 shows the flowchart of this simulation.

Figure 3.7 shows the probability density functions of errors in positions attained after simulated compensations using parameters identified at different identification positions mentioned above. Table 3.1 lists the standard deviations of these distributions along with the corresponding values of ${}_{B1}U_{11}$. These results show that the best identification position

6. Suggested by different criteria.

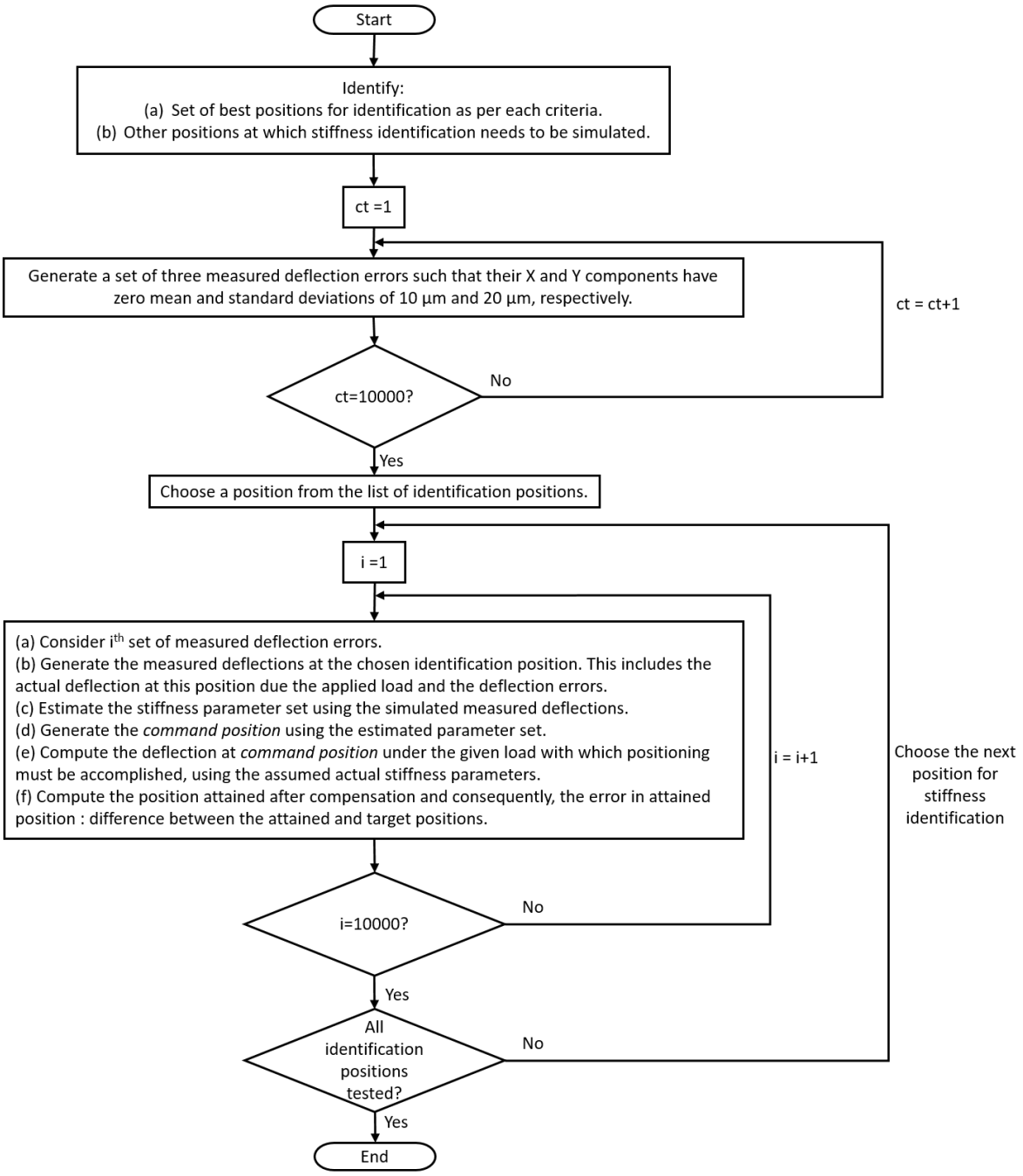

Figure 3.6: Flowchart of the Monte-Carlo simulations of simulation study 1

as per DUIR criterion performs best. Also, the worst identification position as per DUIR criterion is seen to perform worst among all the identification positions. Furthermore,

comparing the values of ${}_{B1}U_{11}$ with the standard deviations of X-coordinate of errors in attained positions shows that the performance trend (of identification positions) shown by the two are same. These observations show that DUIR can effectively predict and help to optimize stiffness identification such that influence of deflection measurement uncertainty on compensation errors is minimized.

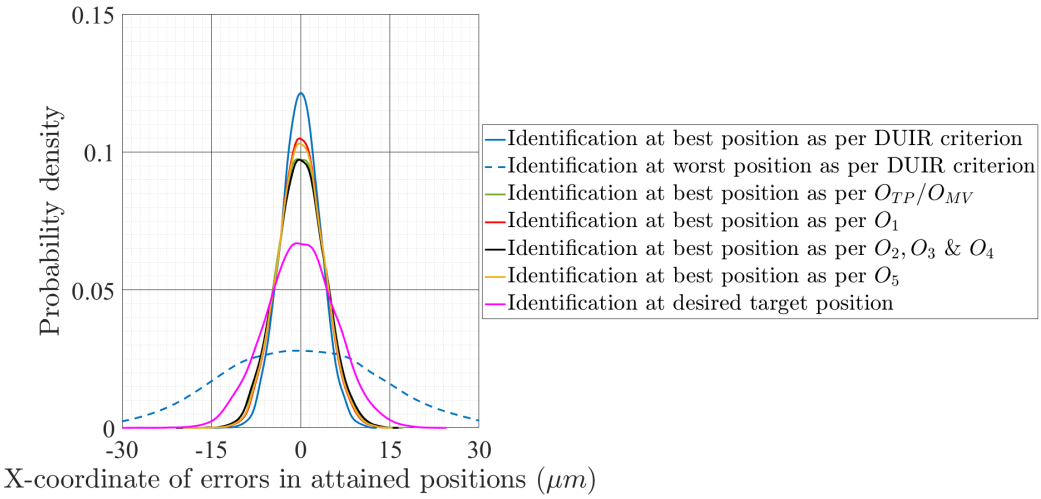

Figure 3.7: Probability density functions of errors in positions attained after simulated compensations in Monte-Carlo simulations of simulation study 1

Table 3.1: Standard deviations of X-coordinate of attained position errors (obtained from Monte Carlo simulations of simulation study 1) and the corresponding values of ${}_{B1}U_{11}$

Identification position	**Standard deviation of X-coordinate of attained position errors** (μm)	**Value of** ${}_{B1}U_{11}$ (m^2)
Best position as per DUIR criterion	3.27	1.044×10^{-11}
Worst position as per DUIR criterion	13.45	1.781×10^{-10}
Best position as per O_{TP}/O_{MV}	3.99	1.557×10^{-11}
Best position as per O_1	3.75	1.377×10^{-11}
Best position as per O_2, O_3 & O_4	4.05	1.602×10^{-11}
Best position as per O_5	3.82	1.425×10^{-11}
Desired target position ${}_{B1}X_D$	5.84	3.3×10^{-11}
Randomly chosen position 1	6	3.579×10^{-11}
Randomly chosen position 2	6.15	3.687×10^{-11}
Randomly chosen position 3	6	3.55×10^{-11}
Randomly chosen position 4	3.4	1.127×10^{-11}

3.4 Simulation study 2: validation of FEIR criterion

Consider a case where elastostatic calibration of the bipod (figure 3.1) must be performed to position its end-effector precisely at a position ${}_{B2}X_D = [0;0]$ mm with a force ${}_{B2}F_D = [0;-200]$ N applied on it. Assume that the measurement system used for deflection measurements has zero (relatively negligible) uncertainty. Also suppose that identification can only be done at one position using one deflection measurement and using a force ${}_{B2}F_M = [0;-200]$ N applied at the end-effector. Furthermore, assume that the forces applied along the X and Y axes at the end-effector are measured using two independent force gauges which have standard uncertainty[7] of 10 N. Therefore, the force assumed to be applied at the end-effector will have an error due to the uncertainty of the force measurement instrument used. The best position for stiffness identification must, therefore, be selected to minimize the influence of error in force applied during stiffness identification on compensation quality, depending on the specifications of desired positioning task[8].

Since only uncertainty of force applied affects stiffness identification, only FEIR criterion had to be formulated to evaluate the suitability of positions for stiffness identification. Here, FEIR criteria were formulated for the case where best positioning would be desired along the X-axis or Y-axis of the end-effector after compensation. In order to validate the proposed criteria, Monte-Carlo simulations were performed in which elastostatic calibrations were simulated many times. In these Monte-Carlo simulations, stiffness identifications were simulated at different positions across the workspace. The performance of these identification positions were then compared with the indication of the proposed FEIR criteria. Section 3.4.1 presents the formulation and indications of FEIR criteria for this case. The details and results of the validation simulations are then presented in section 3.4.2.

7. Uncertainty of measurement expressed in terms of standard deviation.

8. Depending on whether best positioning accuracy is desired : (a) along the X-axis only, or (b) along the Y-axis only, or (c) along both axes, or (d) in terms of distance errors, of the end-effector after compensation.

3.4.1 Formulation of FEIR criterion

The stiffness identification equation (equation 2.6) can firstly be rewritten for this case as

$$ {}_{B2}G \; {}^{as}_{B2}A_M \; {}_{B2}H \; {}_{B2}H^{-1} \left({}_{B2}c + {}^{FE}_{B2}\varepsilon_c \right) = {}_{B2}G \left({}_{B2}\Delta X_M + {}^{FE}_{B2}\varepsilon_{\Delta X_M} \right) \tag{3.12} $$

Here, the left subscript "B2" specifies that the corresponding matrices/arrays of equation 2.6 have been formulated for this case. Since there are no errors in measured deflections due to uncertainty of deflection measurement system, the corresponding terms of equation 2.6 do not exist in equation 3.12. ${}_{B2}G$ is a 2×2 identity matrix since there is only one deflection measurement. ${}_{B2}H$ is a 2×2 identity matrix because the expected magnitudes of estimated parameters are same. ${}_{B2}\Delta X_M$ and ${}^{FE}_{B2}\varepsilon_{\Delta X_M}$ are 2×1 vectors which together constitute the measured deflection. ${}^{FE}_{B2}\varepsilon_{\Delta X_M}$ contains the error in measured deflection due to error in force applied during stiffness identification experiment. ${}^{as}_{B2}A_M$ is a 2×2 matrix which is a function of the force assumed to be applied and the position used for stiffness identification. Parameter set of equation 3.12 is estimated using least squares method.

Matrix Z from equation 2.51 can be written for this case first as it relates the errors in force applied during stiffness identification to the resultant errors in position attained after compensation. It is given by

$$ {}_{B2}Z = {}_{B2}A_D \; {}^{as}_{B2}A_M{}^{+} \; {}^{ap}_{B2}D \tag{3.13} $$

where ${}_{B2}Z$ is a 2×2 matrix. 2×2 matrix ${}_{B2}A_D$ is a function of the target position and force applied at the end-effector during the intended positioning. ${}^{ap}_{B2}D$ is also a 2×2 matrix which is a function of the identification position and the approximate values of stiffness parameters (see section 2.4.1). The assumed actual values of stiffness parameters were used as approximate stiffness parameters.

In this case, the relation between covariance matrices of applied force error and the corresponding error in position attained after compensation (see equation 2.52) can be used

to optimize stiffness identification. The relation between covariance matrices of applied force error and the corresponding attained position error in this case is given by

$$\mathrm{Cov}\left({}^{\mathrm{FE}}_{\mathrm{B2}}\mathcal{E}_{\mathrm{X_A}}\right) \approx {}_{\mathrm{B2}}\mathrm{Z}\ \mathrm{Cov}\left({}_{\mathrm{B2}}\mathcal{E}_{\Delta \mathrm{F_M}}\right)\ {}_{\mathrm{B2}}\mathrm{Z}^{\mathrm{T}} \tag{3.14}$$

Here, ${}^{\mathrm{FE}}_{\mathrm{B2}}\mathcal{E}_{\mathrm{X_A}}$ is the error in position attained after compensation due to the error in force applied during stiffness identification (${}_{\mathrm{B2}}\mathcal{E}_{\Delta \mathrm{F_M}}$). $\mathrm{Cov}\left({}_{\mathrm{B2}}\mathcal{E}_{\Delta \mathrm{F_M}}\right)$ is known from data about uncertainty of the force gauges. Equation 3.14 can then be written as

$$\begin{aligned} \mathrm{Cov}\left({}^{\mathrm{FE}}_{\mathrm{B2}}\mathcal{E}_{\mathrm{X_A}}\right) &\approx {}_{\mathrm{B2}}\mathrm{Z}\ \mathfrak{v}\ \mathrm{I}\ {}_{\mathrm{B2}}\mathrm{Z}^{\mathrm{T}} \\ &\approx \mathfrak{v}\ {}_{\mathrm{B2}}\mathrm{Z}\ {}_{\mathrm{B2}}\mathrm{Z}^{\mathrm{T}} \end{aligned} \tag{3.15}$$

$\mathfrak{v}$ in equation 3.15 is a scalar which is determined by the diagonal elements of $\mathrm{Cov}\left({}_{\mathrm{B2}}\mathcal{E}_{\Delta \mathrm{F_M}}\right)$. The diagonal elements of $\mathrm{Cov}\left({}_{\mathrm{B2}}\mathcal{E}_{\Delta \mathrm{F_M}}\right)$ contain the variances of each element of ${}_{\mathrm{B2}}\mathcal{E}_{\Delta \mathrm{F_M}}$ and they are equal to [9] 100. Consequently, $\mathfrak{v}$ is equal to 100. $\mathrm{Cov}\left({}^{\mathrm{FE}}_{\mathrm{B2}}\mathcal{E}_{\mathrm{X_A}}\right)$ is a 2×2 matrix and its first diagonal element corresponds to the variance along the X-axis of end-effector after compensation. Consequently, the position that minimizes the first diagonal element of $\mathrm{Cov}\left({}^{\mathrm{FE}}_{\mathrm{B2}}\mathcal{E}_{\mathrm{X_A}}\right)$ must be found for best positioning along end-effector's X-axis. Similarly, its second diagonal element must be minimized for best positioning along end-effector's Y-axis. Since ${}_{\mathrm{B2}}\mathrm{Z}\ {}_{\mathrm{B2}}\mathrm{Z}^{\mathrm{T}}$ is only scaled with $\mathfrak{v}$ to get $\mathrm{Cov}\left({}^{\mathrm{FE}}_{\mathrm{B2}}\mathcal{E}_{\mathrm{X_A}}\right)$, the diagonal elements of ${}_{\mathrm{B2}}\mathrm{Z}\ {}_{\mathrm{B2}}\mathrm{Z}^{\mathrm{T}}$ can also be minimized. Let ζ contain the diagonal elements of ${}_{\mathrm{B2}}\mathrm{Z}\ {}_{\mathrm{B2}}\mathrm{Z}^{\mathrm{T}}$.

$$\zeta = \mathrm{diag}\left({}_{\mathrm{B2}}\mathrm{Z}\ {}_{\mathrm{B2}}\mathrm{Z}^{\mathrm{T}}\right) \tag{3.16}$$

Therefore, the position that minimizes the first element of ζ, ζ_1, must be found for best positioning along X-axis of the end-effector. Similarly, the second element of ζ, ζ_2, must be minimized for best positioning along its Y-axis. Figures 3.8 and 3.9 show the values of ζ_1 and ζ_2 for different identification positions across the workspace of the bipod.

9. Since the standard deviations of each element of ${}_{\mathrm{B2}}\mathcal{E}_{\Delta \mathrm{F_M}}$ is 10 N.

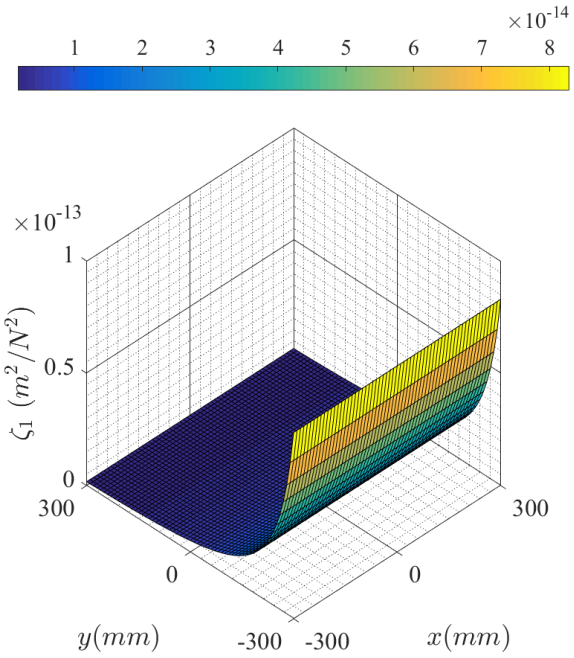

Figure 3.8: ζ_1 values for different identification positions across the workspace of the bipod

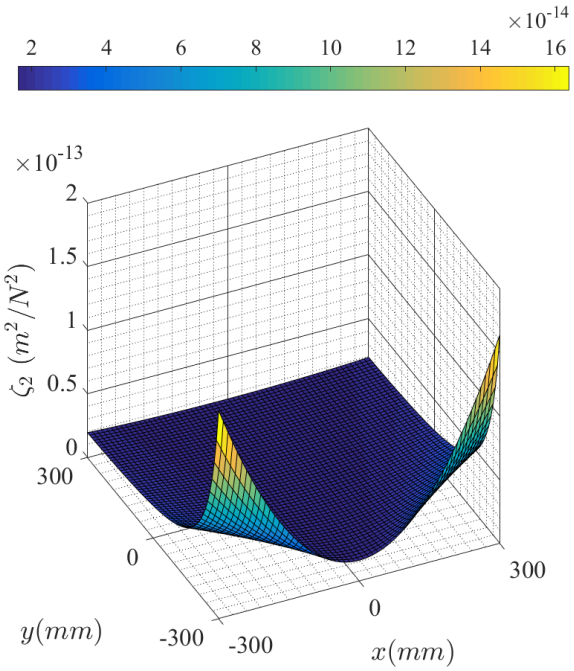

Figure 3.9: ζ_2 values for different identification positions across the workspace of the bipod

3.4.2 Validation simulations

Monte Carlo simulations were performed to validate the efficacy of the proposed FEIR criteria. Figure 3.10 shows the flowchart for this simulation. In these Monte Carlo simulations, stiffness identification experiments were simulated at different positions. These are: P1 $= [0;250]$ mm, P2 $= [0;0]$ mm, P3 $= [0;-250]$ mm, P4 $= [-250;-250]$ mm and P5 $= [250;-250]$ mm. At each of these identification positions, stiffness identification experiments were simulated 10000 times and the error in applied force was different in each trial[10]. The estimated parameter set in each trial was used to simulate the compensation at the target position ${}_{B2}X_D$ with a force $[0;-200]$ N at its end-effector. To validate the proposed FEIR criteria, the compensation quality achieved (in terms of compensation errors along the X and Y axes) using the different identification positions can be cross-checked with the indication of FEIR criteria (figures 3.8 and 3.9).

Table 3.2 lists the standard deviations of errors in positions attained after performing the Monte-Carlo simulations described above. Comparing the indication of FEIR criteria (ζ_1 and ζ_2) with the results of Monte Carlo simulations (standard deviations of errors in positions attained), one can observe the following:

(a) positions P1, P2 and P3 have the same standard deviations of ${}^{FE}_{B2}\mathcal{E}^{y}_{X_A}$ in the results of the Monte-Carlo simulations. The standard deviation of ${}^{FE}_{B2}\mathcal{E}^{x}_{X_A}$ for P1 is smaller than that of P2, which in turn is smaller than that of P3. The same corresponding trends are seen in plots of ζ_1 and ζ_2 (figures 3.8 and 3.9) which are the indicators of compensation performance along X and Y coordinates of the end-effector, respectively. That is, ζ_2 remains the same (and is minimum) for P1, P2 and P3 while ζ_1 decreases along the +ve direction of Y-axis.

(b) positions P3 and P4 have the same standard deviations of ${}^{FE}_{B2}\mathcal{E}^{x}_{X_A}$ in the results of the Monte-Carlo simulations whereas the standard deviation of ${}^{FE}_{B2}\mathcal{E}^{y}_{X_A}$ for P3 is smaller than that of P4. The same corresponding trends can be seen for ζ_1 and ζ_2.

(c) positions P4 and P5 have same standard deviations of ${}^{FE}_{B2}\mathcal{E}^{x}_{X_A}$ and ${}^{FE}_{B2}\mathcal{E}^{y}_{X_A}$. Corresponding values of ζ_1 and ζ_2 also indicate the same.

10. The applied force error varied as per the assumed standard deviations of force gauge uncertainty: 10 N along X and Y coordinates of the applied force.

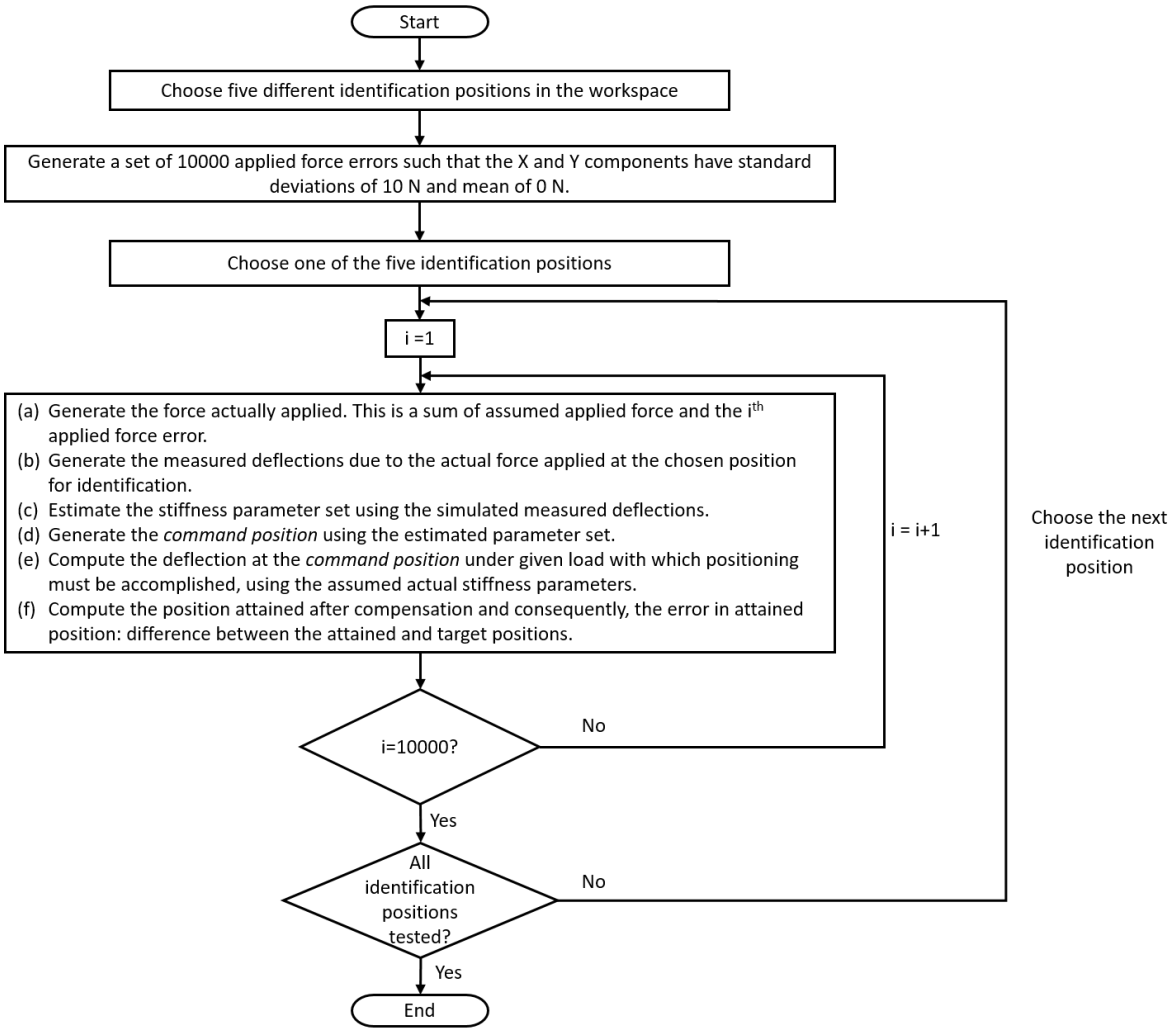

Figure 3.10: Flowchart of the Monte-Carlo simulations of simulation study 2

The observations listed above indicate that FEIR criterion can predict and consequently, allow to minimize the influence of errors in forces applied during stiffness identification experiment on the compensation quality.

Table 3.2: Standard deviations of errors in positions attained after compensations, in the Monte-Carlo simulations described in figure 3.10

Position label	**Identification position (mm)**	**Standard deviation of** ${}^{FE}_{B2}\mathcal{E}^{x}_{X_A}$ (μm)	**Standard deviation of** ${}^{FE}_{B2}\mathcal{E}^{y}_{X_A}$ (μm)
P1	[0;250]	0.4	1.3
P2	[0;0]	0.7	1.3
P3	[0;-250]	1.9	1.3
P4	[-250;-250]	1.9	2.5
P5	[250;-250]	1.9	2.5

Note: ${}^{FE}_{B2}\mathcal{E}^{x}_{X_A}$ and ${}^{FE}_{B2}\mathcal{E}^{y}_{X_A}$ are the X and Y coordinates of ${}^{FE}_{B2}\mathcal{E}_{X_A}$, respectively.

3.5 Simulation study 3: validation of use of both criteria together

Consider a case where elastostatic calibration of the bipod (figure 3.1) has to be performed to position its end-effector at position ${}_{B3}X_D = [0;0]$ mm with a force ${}_{B3}F_D = [0;-200]$ N applied to it. Assume that best positioning accuracy is required only along its X-axis. Also suppose that stiffness identification can be done at only one position using three deflection measurements and using force ${}_{B3}F_M = [0;-200]$ N applied at the end-effector. Let the uncertainty of position measurement system lead to independent deflection measurement uncertainty of 10 μm standard deviation along end-effector's X and Y axes. Furthermore, assume that the applied force can't be determined precisely due to the setup being used. Let there be an error in applied force described by the vector $[-75;-75]$ N every time force is applied using this apparatus. Note that this applied force error is not known to the user. Best position for stiffness identification must, therefore, be selected to identify optimal parameter set.

Stiffness identification is bound to be affected by uncertainty of deflection measurements and errors in forces applied in this case. Therefore, both DUIR and FEIR criteria must be used together to find the best position for stiffness identification. For the sake of comparison, best position for stiffness identification can also be found using only DUIR criterion and only FEIR criterion. To compare the performances of these identification positions, Monte-Carlo simulations can be performed to simulate elastostatic calibrations

of the bipod many times. Section 3.5.1 presents the details and results of stiffness identification optimization. The details and results of the validation simulations are shown in section 3.5.2.

3.5.1 Stiffness identification optimization

The stiffness identification equation (equation 2.6) can be written for this case as

$$ {}_{B3}G_U \, {}^{as}_{B3}A_M \, {}_{B3}H \, {}_{B3}H^{-1} \left({}_{B3}c + {}^{DU}_{B3}\varepsilon_c + {}^{FE}_{B3}\varepsilon_c \right) = {}_{B3}G_U \left({}_{B3}\Delta X_M + {}^{DU}_{B3}\varepsilon_{\Delta X_M} + {}^{FE}_{B3}\varepsilon_{\Delta X_M} \right) \tag{3.17} $$

Here, the left subscript "B3" specifies that the corresponding matrices/arrays of equation 2.6 have been formulated for this case. ${}_{B3}G_U$ is a 6×6 matrix with inverse of deflection measurement uncertainties along its diagonal elements and is formulated as shown in equation 1.22. ${}_{B3}H$ is a 2×2 identity matrix because the expected magnitudes of estimated parameters are same. ${}_{B3}\Delta X_M$, ${}^{DU}_{B3}\varepsilon_{\Delta X_M}$ and ${}^{FE}_{B3}\varepsilon_{\Delta X_M}$ are 6×1 vectors which together constitute the measured deflections. ${}^{DU}_{B3}\varepsilon_{\Delta X_M}$ and ${}^{FE}_{B3}\varepsilon_{\Delta X_M}$ contain the errors in measured deflections due to deflection measurement uncertainty and errors in force applied during stiffness identification, respectively. ${}^{as}_{B3}A_M$ is a 6×2 matrix which is a function of the forces assumed to be applied and the position used for stiffness identification. Parameter set of equation 3.17 is estimated using least squares method.

To formulate a DUIR criterion, matrix U must first be formulated for this case. Using equation 2.30, matrix U for this case can be written as

$$ {}_{B3}U = {}_{B3}A_D \, {}_{B3}H \left(\widetilde{{}^{as}_{B3}A_M}^{T} \, \widetilde{{}^{as}_{B3}A_M} \right)^{-1} {}_{B3}H^T \, {}_{B3}A_D^T \tag{3.18} $$

Here, ${}_{B3}A_D$ is a 2×2 matrix which is a function of the target position and the force applied at the end-effector during the intended positioning. ${}_{B3}U$ is a 2×2 matrix and it relates the uncertainty of deflection measurements to uncertainty of resultant errors in positioning after compensation (see equation 2.30). The first element of ${}_{B3}U$, ${}_{B3}U_{11}$, is the scaling factor corresponding to the variance of X-coordinate of errors in position attained after

compensation. Hence, the identification position that leads to minimum value of ${}_{B3}U_{11}$ minimizes the impact of uncertainty of measured deflections on the desired compensation.

To formulate a FEIR criterion for this case, matrix Z needs to be formulated first. Using equation 2.51, Z can be written for this case as

$$ {}_{B3}Z = {}_{B3}A_D \; {}^{as}_{B3}A_M{}^{+} \; {}^{ap}_{B3}D \tag{3.19} $$

Here, ${}_{B3}Z$ is a 2×6 matrix. ${}^{ap}_{B3}D$ is a 2×2 matrix which is a function of the identification position and the approximate values of stiffness parameters (see section 2.4.1). The assumed actual values of stiffness parameters (10 $N/\mu m$ for each spring) were used as approximate stiffness parameters. Given that prior information is not available about the error in applied force, one way to minimize its impact on the desired compensation is to minimize the norm of first row of ${}_{B3}Z$. The reason for this is that the values of the first row of ${}_{B3}Z$ scale the error in applied force to give the X component of error in position attained after compensation.

Since both DUIR and FEIR criteria need to be considered to find the best position for stiffness identification, a multi-objective optimization needs to be done. The multi-objective optimization problem for this case can be written as

$$ \begin{aligned} \min_{{}_{B3}X_M} \quad & \{f_1, f_2\} \\ \text{s.t.} \quad & \text{Workspace limits} \\ \text{where,} \quad & f_1 = {}_{B3}U_{11} \\ & f_2 = \text{norm}\left(\left[\, {}_{B3}Z_{11} \; {}_{B3}Z_{12} \; \ldots \; {}_{B3}Z_{16} \,\right]\right) \end{aligned} \tag{3.20} $$

Here, ${}_{B3}X_M$ is the identification position which minimizes both f_1 and f_2. ${}_{B3}Z_{ij}$ is the j^{th} element of i^{th} row of ${}_{B3}Z$. The optimization problem of equation 3.20 leads to a number of Pareto optimal solutions. These are shown in figure 3.11. 50 solutions were considered on the Pareto front. Many methods exist to choose the optimal solution from these Pareto solutions. One of these methods, called the *method of global criterion* [Miettinen, 1999], was used to find the optimal solution in this case. For this, the *ideal objective vector* must be

obtained first, which is a solution that would be ideal but not reachable. The ideal objective vector, denoted here as w^{id}, is defined by the lower bounds of the Pareto front. It is given by

$$w^{id} = \left[\min\left(f_1({}^{PF}_{B3}X^i_M)\right), \min\left(f_2({}^{PF}_{B3}X^i_M)\right)\right], i = 1...50 \tag{3.21}$$

where ${}^{PF}_{B3}X^i_M$ is the identification position corresponding to the i^{th} solution on the Pareto front. The solution on the Pareto front that is closest to the ideal objective vector is then usually chosen as the optimal solution. However, when the objective functions have different units and magnitudes, the function values of Pareto solutions must be scaled before choosing the closest point [Miettinen, 1999]. The new scaled objective function values are given by

$$\overline{f_1}^r = \frac{f_1^r - w_1^{id}}{w_1^{nad}} \tag{3.22}$$

$$\overline{f_2}^r = \frac{f_2^r - w_2^{id}}{w_2^{nad}} \tag{3.23}$$

In equations 3.22 and 3.23, $\overline{f_1}^r$, $\overline{f_2}^r$, ${f_1}^r$ and ${f_2}^r$ are the values of $\overline{f_1}$, $\overline{f_2}$, f_1 and f_2 corresponding to the r^{th} Pareto solution (out of 50), respectively. w_i^{id} and w_i^{nad} refer to the i^{th} components of w^{id} and w^{nad}, respectively. w^{nad} is the *Nadir objective vector* [Miettinen, 1999] and it is defined by the upper bounds of Pareto front. It is given by

$$w^{nad} = \left[\max\left(f_1({}^{PF}_{B2}X^i_M)\right), \max\left(f_2({}^{PF}_{B2}X^i_M)\right)\right], i = 1...50 \tag{3.24}$$

Ideal and Nadir objective vectors are shown in figure 3.11. The scaled Pareto front and the corresponding ideal and Nadir objective vectors are shown in figure 3.12 . The solution on the scaled Pareto front closest to the scaled ideal objective vector was then chosen as the optimal solution. The optimal solution is shown in figures 3.11 and 3.12.

The best position for stiffness identification were found using: (a) both FEIR and DUIR criteria (optimal solution on the Pareto front), (b) DUIR criterion only (minimizing only f_1

from 3.20), and (c) FEIR criterion only (minimizing only f_2 from 3.20). The best positions for stiffness identification as per all three criteria mentioned above are shown in table 3.3.

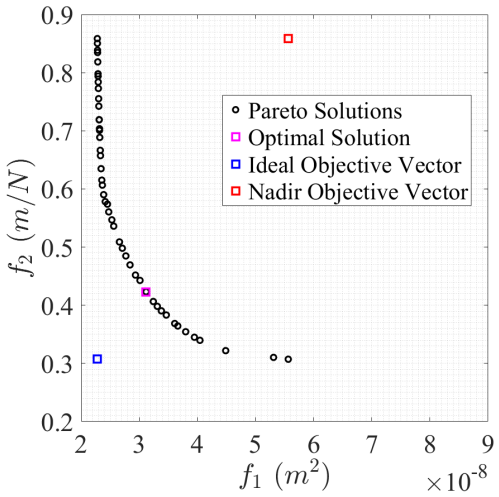

Figure 3.11: Pareto front for the multi-objective optimization problem of equation 3.20

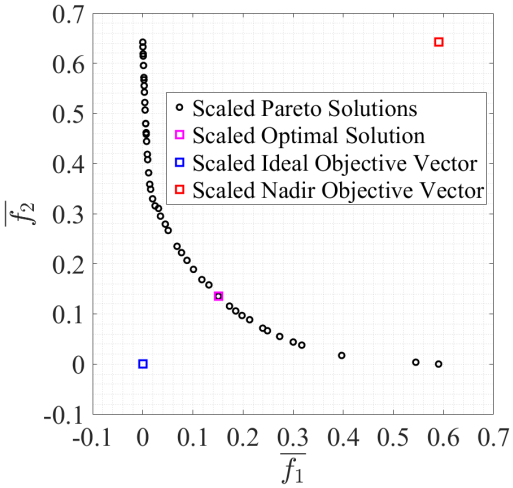

Figure 3.12: Scaled Pareto front for the multi-objective optimization problem of equation 3.20

Table 3.3: Best position for stiffness identification as per different criteria discussed in section 3.5.1

Best position as per	**Position** (mm)
DUIR and FEIR criteria	[25.4;134.4]
DUIR criterion only	[0;-100]
FEIR criterion only	[300;300]

3.5.2 Validation simulations

To compare performances of different identification positions, Monte-Carlo simulations of simulated elastostatic calibrations of the bipod were performed with the positioning specifications of this simulation study. Stiffness identification experiment was simulated 10000 times at each identification position with different set of errors in measured deflections every time. The errors in measured deflections had errors due to: (a) uncertainty of measured defections (10 µm standard deviation along each axis), and (b) error in force applied ($[-75;-75]$ N). The estimated set of stiffness parameters in each trial was used to simulate position compensation. The mean and standard deviations of errors in positions attained after simulated compensations can then be used to evaluate the performance of the three identification positions. Figure 3.13 shows the flowchart for this Monte-Carlo simulation.

Figure 3.14 shows the probability density functions of X-coordinates of position errors after compensation, obtained using the Monte-Carlo simulations described above. Table 3.4 lists the corresponding standard deviations and means. These results show that the standard deviation of X-coordinates of position errors is least when only DUIR criterion was used to choose the best identification position. This result was expected because the variance of position errors after compensation was dependent only on the variance of deflection measurements in this case and DUIR criterion was framed to minimize this propagation. Furthermore, the mean of X-coordinates of position errors after compensation is least when only FEIR criterion was used to select the best identification position. This too is as expected because the constant error in forces applied in the Monte-Carlo simulations lead to a constant offset in positions attained after compensation and the FEIR criterion formulated here minimizes this propagation. When the best identification position

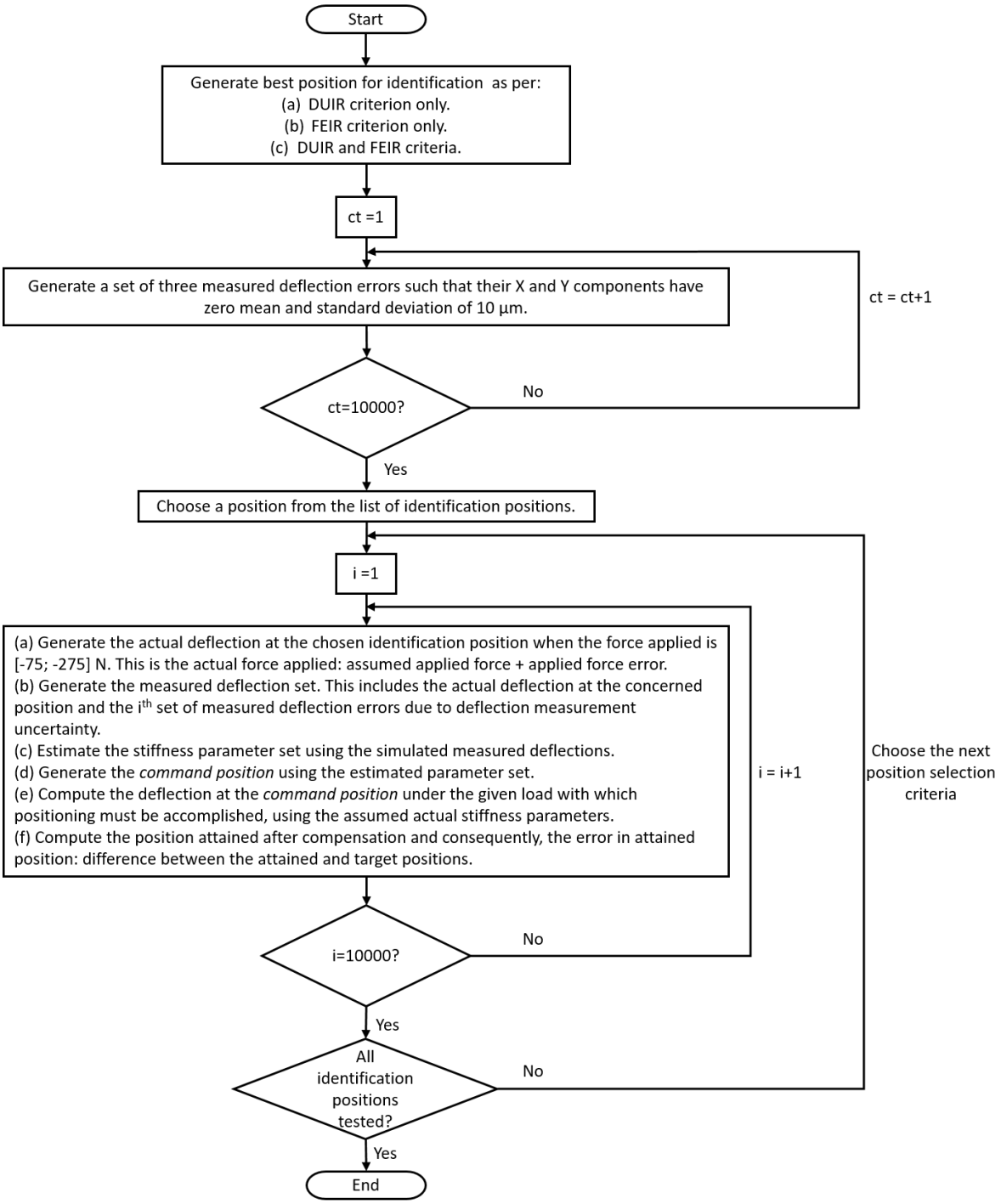

Figure 3.13: Flowchart for the Monte-Carlo simulations of simulation study 3

according to both criteria was used for stiffness identification, the resulting distribution shows that a middle ground has been found. This distribution is desirable over the other two because it has the highest probability of achieving perfect compensation (zero error in position attained after compensation).

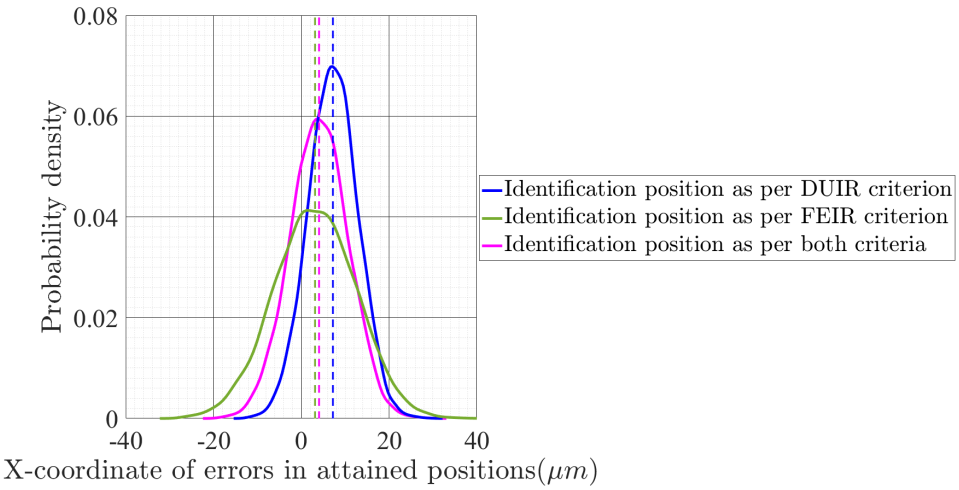

Figure 3.14: Probability density functions of errors in positions attained after compensation in the Monte-Carlo simulations described in section 3.5.2 (dashed lines show the mean of each distribution)

Table 3.4: Standard deviations and means of errors in positions attained after compensation in the Monte-Carlo simulations described in section 3.5.2

Identification position as per	**Standard deviation of X-coordinates of errors in attained positions** (μm)	**Mean of X-coordinates of errors in attained positions** (μm)
DUIR criterion only	5.6	7.2
FEIR criterion only	9.3	3.1
DUIR and FEIR criteria	6.6	4.1

3.6 Conclusion

This chapter presented three simulation studies performed on a bipod to evaluate the efficacy of stiffness identification optimization framework presented in chapter 2. In the first simulation study, elastostatic calibrations were simulated in which only deflec-

tion measurement uncertainty affected stiffness identification. In this, stiffness identification measurement conditions (poses and forces) suggested by DUIR criterion and various previously proposed criteria were used for stiffness identification. The measurement conditions suggested by DUIR criterion lead to best compensation quality as compared to the ones suggested by previously proposed criteria. Furthermore, results also showed that DUIR criterion could precisely predict the influence of stiffness identification measurement conditions on compensation quality, in the presence of deflection measurement uncertainties. In the second simulation study, elastostatic calibrations were simulated in which stiffness identification was affected only by errors in applied forces. In this, elastostatic calibrations were simulated using different measurement conditions for stiffness identification. The positioning performances achieved using the different stiffness identification measurement conditions were compared to the indications of FEIR criteria. Results showed that FEIR criterion can precisely predict and allow to minimize the influence of errors in forces applied during stiffness identification on the compensation quality. In the last simulation study, elastostatic calibrations were simulated in which errors from both sources [11] were made to influence stiffness identification. In these simulated elastostatic calibrations, three sets of measurement conditions were selected for stiffness identification: one using DUIR criterion, another using FEIR criterion and the last one using both criteria. Results confirmed that using both criteria for selecting measurement conditions for stiffness identification gives best compensation quality in this case.

11. Deflection measurement uncertainty and errors in forces applied during stiffness identification.

CHAPTER

4 Experimental validation of developed techniques using elastostatic calibrations of a hexapod positioning system

Contents

Chapter Abstract

In this chapter, experimental studies on elastostatic calibration of a high-precision positioning hexapod are documented. These studies were aimed at experimentally validating the efficacies of elastostatic calibration of hexapods and the stiffness identification optimization framework presented in chapter 2. Results of these studies confirm the efficacies of both.

4.1 Introduction

This chapter presents experimental studies on elastostatic calibration of a high-precision hexapod positioning system. These studies are aimed at: (a) experimentally validating elastostatic calibration of hexapod, and (b) experimentally validating the FEIR criterion. Experimental validation of DUIR criterion was not performed because of impracticality of this endeavour with the setup available. This is because this study would require repetition of positioning experiments large number of times (>> 1000) and this was not practical with the experimental setup available. Large number of positioning experiments are required because obtaining reliable values of variance of poses attained after compensation is necessary for validation of DUIR criterion. This is because DUIR criterion minimizes the variance of possible errors in poses attained after compensation (see section 2.3).

The experimental studies presented in this chapter were performed on a hexapod used for high-precision positioning applications from Symétrie [Symétrie, d] (see figures 4.1 and 4.2). This hexapod has a repeatability of $\pm 0.5\ \mu m$ in translations and $\pm 2.5\ \mu rad$ in rotations. More details about this hexapod can't be disclosed due to confidentiality. These experiments required an apparatus for measuring the pose of the hexapod's platform and an apparatus for applying necessary forces/moments on it. The pose measurement apparatus consisted of a coordinate measuring machine (LK-METRIS CMM with a RENISHAW SP25M scanning probe [Renishaw]) and three precision balls. The uncertainty of points measured using this CMM, quantified using the MPE_P value [ISO, 2000], is about $\pm 2\ \mu m$.. The apparatus available for applying force/moment consisted of a set of weights that could be only placed on the platform (see figure 4.2). This loading setup lead to the constraint that load could be applied only along the Z-axis of the hexapod's platform. Furthermore, the hexapod couldn't be rotated about its X and Y axes with the mass mounted on it as it would lead to sliding off of the weights from the platform.

This chapter is organized as follows: section 4.2 presents the kinematic and stiffness modelling of hexapods. Section 4.3 presents the details and results of the experimental study performed to validate elastostatic calibration of the hexapod. This is followed by

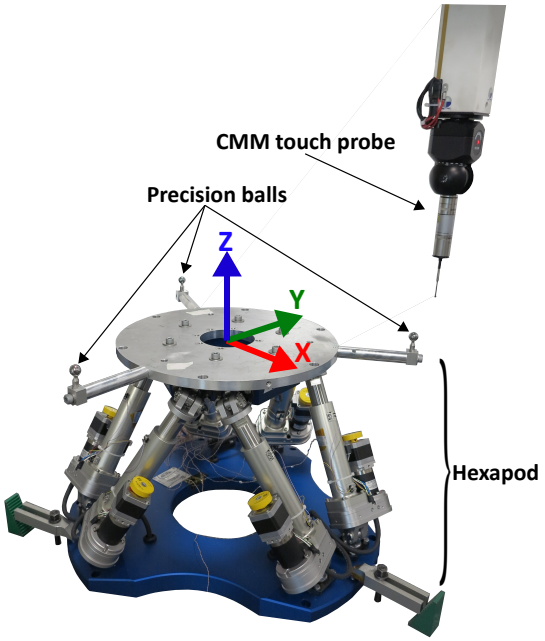

Figure 4.1: Hexapod (without mass mounted on the platform) along with the pose measurement apparatus

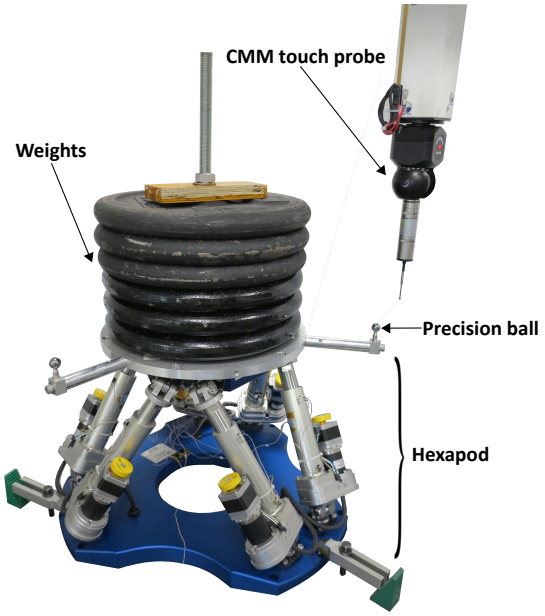

Figure 4.2: Hexapod (with mass mounted on the platform) along with the pose measurement apparatus

details and results of the experimental study performed on the hexapod to validate FEIR citeria in section 4.4. Finally, section 4.5 presents the conclusions of this chapter.

4.2 Kinematic and stiffness modelling of hexapod

Figure 4.3 shows the kinematic scheme of the UPS (universal-prismatic-spherical) hexapod of figures 4.1 and 4.2. Each leg consists of a UPS chain that connects the base to the platform. Poses of the platform of this hexapod are defined by a coordinate frame fixed to the platform at its center (platform frame).

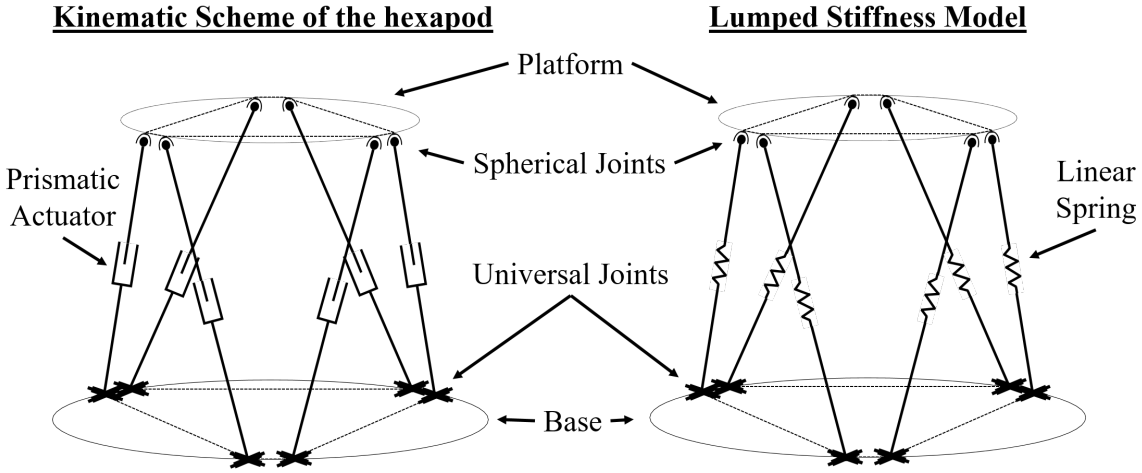

Figure 4.3: Kinematic scheme and the lumped stiffness model of the hexapod under study

${}_{H}X$ contains the 6-DOF pose coordinates of the platform frame with the hexapod in any arbitrary configuration, with respect to the same frame when the hexapod is in configuration shown in figure 4.1 (zero pose [1]). It is given by

$$ {}_{H}X = [Tx\ Ty\ Tz\ Rx\ Ry\ Rz]^{T} \tag{4.1} $$

where Tx,Ty and Tz denote the translations along the X, Y and Z axes of the platform

1. This is the configuration of the hexapod in which all of the platform pose parameters are zero. In this configuration, all the legs are locked in the center of their strokes and have the same lengths.

frame. Rx,Ry and Rz denote the rotations about the X, Y and Z axes of the platform frame. ${}_H q$ contains the lengths of the legs and is given by

$$ {}_H q = [{}_H q_1 \ {}_H q_2 \ {}_H q_3 \ {}_H q_4 \ {}_H q_5 \ {}_H q_6]^T \tag{4.2} $$

The velocity of the end-effector and those of the actuated joints are related as per the following equation:

$$ {}_H \eta = {}_H J \ {}_H \dot{q} \tag{4.3} $$

Here, ${}_H \eta$ is the end-effector's velocity vector, ${}_H \dot{q}$ contains the velocities of the actuators and ${}_H J$ is the Jacobian matrix. The equation relating the differential pose vector (${}_H \Delta X$) and the differential actuator position vector (${}_H \Delta q$), as in equation 1.13, can be written for this case as

$$ {}_H \Delta q = {}_H \check{J}^{-1} \ {}_H \Delta X \tag{4.4} $$

Here, ${}_H \check{J}$ is the modified Jacobian matrix. ${}_H \check{J}^{-1}$ is given by

$$ {}_H \check{J}^{-1} = {}_H J^{-1} \begin{bmatrix} 1 & 0 \\ 0 & \mathcal{B} \end{bmatrix} \tag{4.5} $$

where I is a 3×3 identity matrix and $\mathcal{B}$ is given by

$$ \mathcal{B} = \underbrace{\begin{bmatrix} c_{Rz}.c_{Ry} & -s_{Rz}.c_{Rx} + c_{Rz}.s_{Ry}.s_{Rx} & s_{Rz}.s_{Rx} + c_{Rz}.s_{Ry}.c_{Rx} \\ s_{Rz}.c_{Ry} & c_{Rz}.c_{Rx} + s_{Rz}.s_{Ry}.s_{Rx} & -c_{Rz}.s_{Rx} + s_{Rz}.s_{Ry}.c_{Rx} \\ -s_{Ry} & c_{Ry}.s_{Rx} & c_{Ry}.c_{Rx} \end{bmatrix}}_{\mathcal{R}} \begin{bmatrix} 1 & 0 & -s_{Ry} \\ 0 & c_{Rx} & c_{Ry}.s_{Rx} \\ 0 & -s_{Rx} & c_{Ry}.c_{Rx} \end{bmatrix} \tag{4.6} $$

In equation 4.6, $c_\bullet = \cos(\bullet)$, $s_\bullet = \sin(\bullet)$ and $\mathcal{R}$ is the rotation matrix. The operation of equation 4.5 is necessary because ${}_H \check{J}^{-1}$ relates the derivatives of components of ${}_H X$ to

the derivatives of components of ${}_{H}q$ whereas ${}_{H}J^{-1}$ relates the end-effector velocity vector to the actuator velocities. Consequently, J^{-1} must be modified to get ${}_{H}\check{J}^{-1}$ as per equation 4.5 to take into account the relationship between angular velocities and angle derivatives. The reader is referred to [Ardakani and Bridges, 2010] for the derivation of the expression for $\mathcal{B}$.

A simple lumped stiffness model can be used to model the static stiffness characteristics of this hexapod (see figure 4.3). This model uses one linear spring[2] to model the stiffness of each leg (${}_{H}k_{i=1..6}$). This modelling method is consistent with the method described in chapter 1, i.e., only stiffnesses along actuated joints are considered. The Cartesian stiffness matrix (as in equation 1.15), ${}_{H}K_{C}$, for this stiffness model of the hexapod can be written as

$$ {}_{H}K_{C} = {}_{B}J^{-T}\ {}_{H}K\ {}_{H}\check{J}^{-1} \tag{4.7} $$

where matrix ${}_{H}K$ is diagonal matrix with leg stiffnesses forming its diagonal elements. It is given by

$$ {}_{H}K = \begin{bmatrix} {}_{H}k_1 & 0 & 0 & 0 & 0 & 0 \\ 0 & {}_{H}k_2 & 0 & 0 & 0 & 0 \\ 0 & 0 & {}_{H}k_3 & 0 & 0 & 0 \\ 0 & 0 & 0 & {}_{H}k_4 & 0 & 0 \\ 0 & 0 & 0 & 0 & {}_{H}k_5 & 0 \\ 0 & 0 & 0 & 0 & 0 & {}_{H}k_6 \end{bmatrix} \tag{4.8} $$

Matrix ${}_{H}K_{C}$ relates the differential force vector (${}_{H}\Delta F$) and the differential position vector (${}_{H}\Delta X$) as

$$ {}_{H}\Delta F = {}_{H}K_{C}\ {}_{H}\Delta X \tag{4.9} $$

2. This follows the assumption that each of the legs exhibit linear stiffness behavior.

Rearranging equation 4.9 yields a relationship similar to equation 1.17:

$$ {}_{H}A\ {}_{H}c = {}_{H}\Delta X \tag{4.10} $$

In equation 4.10, ${}_{H}A$ is the *observation matrix* and it is given by

$$ {}_{H}A_{ij} = {}_{H}\check{J}_{ij}\ \Big(\sum_{r=1}^{6} {}_{H}J_{rj}\ {}_{H}\Delta F_{r}\Big) \tag{4.11} $$

${}_{H}A_{ij}$, ${}_{H}J_{ij}$ and ${}_{H}\check{J}_{ij}$ in the above equation denote the j^{th} element of the i^{th} row of matrices ${}_{H}A$, ${}_{H}J$ and ${}_{H}\check{J}_{ij}$, respectively. ${}_{H}\Delta F_{r}$ is the r^{th} element of vector ${}_{H}\Delta F$. ${}_{H}c$ is the vector containing compliance parameters and is given by

$$ {}_{H}c = \Big[\frac{1}{{}_{H}k_1}\ \frac{1}{{}_{H}k_2}\ \frac{1}{{}_{H}k_3}\ \frac{1}{{}_{H}k_4}\ \frac{1}{{}_{H}k_5}\ \frac{1}{{}_{H}k_6}\Big]^{T} \tag{4.12} $$

Appendix G presents a preliminary study performed on another high-precision positioning hexapod to validate the efficacy of the stiffness model (for hexapods) presented here to predict the deflections of a hexapod with loaded platform.

4.3 Experimental study 1: validation of elastostatic calibration of hexapod

This section presents the details and results of an experimental study performed to validate elastostatic calibration of the hexapod shown in figures 4.1 and 4.2. This elastostatic calibration was performed to achieve best possible positioning performance along all the axes (Tx—Rz) of the platform and throughout its workspace, with a mass of 121.25 kg (close to the maximum payload allowed for the given hexapod) mounted on it. The setups used for pose measurement and loading for this study are described in section 4.1.

One of the factors[3] defining the possible pose-force sets for stiffness identification was

3. Other factors defining the possible pose-force sets were: (a) the joint and actuator limits, and (b) payload limit.

the apparatus available for applying forces/moments on the platform. As shown in figure 4.2, this setup consisted of a set of weights which could be placed on the hexapod's platform. Due to this loading constraint, force could be applied only along the Z-axis of the platform and the poses for stiffness identification needed to have Rx and Ry to be zero. The magnitude of mass to be placed on the platform for stiffness identification experiment also had to be chosen. The maximum possible mass (121.25 kg - close to the hexapod's payload limit) was chosen for this purpose. This was desirable because higher magnitude of measured deflections leads to lesser impact of measurement uncertainty on identified parameters. Furthermore, choice was made to perform stiffness identification at just one pose for the sake of simplicity. Therefore, the best pose had to be found for stiffness identification of this hexapod and maximum possible number of deflection measurements had to be performed at this pose. The factor limiting the maximum number of deflection measurements was the thermal deflection of the hexapod during pose measurements. It was necessary to keep the thermal deflection of the hexapod as less as possible so that it wouldn't adulterate the load-deflection measurements. From past experience, 30 minutes was deemed as a good estimation of the maximum time until which thermally stable readings could be made. Approximately 5 deflection measurements (5 pose measurements before and after loading) could be made in these 30 minutes using the method described in appendix A.

Section 4.3.1 presents the details and results of stiffness identification and its optimization in this case. This is followed by details and results of the experiments performed to validate the compensation using estimated stiffness parameters in section 4.3.2.

4.3.1 Stiffness identification optimization

For performing stiffness identification as per choices described above, the stiffness identification equation can be written for this case first. Equation 2.6 can be written for this case as

$$ {}_{H1}G_C \; {}^{as}_{H1}A_M \; {}_{H1}H \; {}_{H1}H^{-1} \left({}_{H1}c + {}^{Du}_{H1}\varepsilon_c + {}^{FE}_{H1}\varepsilon_c \right) = {}_{H1}G_C \left({}_{H1}\Delta X_M + {}^{Du}_{H1}\varepsilon_{\Delta X_M} + {}^{FE}_{H1}\varepsilon_{\Delta X_M} \right) \tag{4.13} $$

Left subscript "H1" of the variables in the above equation specifies that the corresponding matrices/arrays of equation 2.6 have been formulated for this case. ${}_{H1}G_C$ is a 30×30 task variable scaling matrix[4] and is formulated as shown in equation 1.23. Matrix ${}_{H1}H$ in this case is a 6×6 identity matrix because the stiffness parameters are expected to have the same order of magnitude. This is because every leg of the given hexapod has the same design and materials. ${}_{H1}\Delta X_M$, ${}^{Du}_{H1}\mathcal{E}_{\Delta X_M}$ and ${}^{FE}_{H1}\mathcal{E}_{\Delta X_M}$ are 30×1 vectors which together constitute the measured deflections. ${}^{Du}_{H1}\mathcal{E}_{\Delta X_M}$ and ${}^{FE}_{H1}\mathcal{E}_{\Delta X_M}$ contain the errors in measured deflections due to deflection measurement uncertainty and errors in force/moment applied during stiffness identification, respectively. ${}^{as}_{H1}A_M$ is a 30×6 matrix which is a function of the forces/moments assumed to be applied and the pose used for stiffness identification. Parameter set of equation 4.13 is estimated using least squares method. Best pose had to be found using the DUIR and FEIR criteria to ensure best possible compensation.

For the formulation of a DUIR criterion, matrix ${}_{H1}G_C$ must be known beforehand (see section 2.3). Formulation of matrix ${}_{H1}G_C$ requires knowledge of variance and correlation of deflection measurements. However, the variance and correlation of measured deflections is extremely difficult to predict in this case. Among other factors such as complexity of CMM measurements and the measurement method (as in appendix A), minor thermal deflections of the hexapod complicate the estimation of deflection measurement uncertainty beforehand. Consequently, ${}_{H1}G_C$ could not be determined beforehand in this case and a DUIR criterion could not be formulated. Hence, the best pose for stiffness identification was found using FEIR criterion only.

For the formulation of FEIR criterion, matrix Z must be formulated first. Since the platform pose coordinates have both translations and rotations, two separate Z matrices must be formulated here as in equations 2.53 and 2.54. They can be written as

$$ {}^{FE,r}_{H1}\mathcal{E}_{X_A} \approx -\overbrace{{}^{r}_{H1}A_D \, {}^{as}_{H1}A_M^{+} \, {}^{ap}_{H1}D}^{{}^{r}_{H1}Z} \, {}_{H1}\mathcal{E}_{\Delta F_M} \tag{4.14} $$

4. Note that the deflection measurements are correlated in this case and consequently, task variable scaling matrix must be formulated as per equation 1.23. The deflection measurements are correlated because the individual measured pose parameters (Tx, Ty,...,Rz) are correlated. This is a consequence of the pose measurement method (refer appendix A).

$$ {}^{FE,t}_{H1}\mathcal{E}_{X_A} \approx -\overbrace{{}^{t}_{H1}A_D\ {}^{as}_{H1}A_M{}^{+}\ {}^{ap}_{H1}D}^{{}^{t}_{H1}Z}\ {}_{H1}\mathcal{E}_{\Delta F_M} \tag{4.15} $$

where the left subscript 'H1' specifies that the corresponding matrices/arrays of equations 2.53 and 2.54 have been formulated for this case. ${}^{t}_{H1}A_D$ and ${}^{r}_{H1}A_D$ are the matrices containing first and last three rows of ${}_{H1}A_D$, respectively. ${}_{H1}A_D$ is a 6×6 matrix which is a function of the target pose and the force/moment applied at the end-effector during the intended positioning. To get ${}^{ap}_{H1}D$, some preliminary approximate stiffness estimations must be made[5]. The approximate stiffness parameter values were found by performing a set of three deflection measurements at zero pose by mounting 121.25 kg mass on the platform. Table 4.1 shows the approximate values of these stiffness parameters. ${}^{r}_{H1}Z$ and ${}^{t}_{H1}Z$ are 3×30 matrices. ${}_{H1}\mathcal{E}_{\Delta F_M}$ is a 30×1 array in which the first six elements repeat themselves five times due to presence of redundant measurements. It must be noted that equations 4.14 and 4.15 consider only one pose at which best positioning is desired. Since best possible positioning is desired throughout the workspace, equation that relates ${}_{H1}\mathcal{E}_{\Delta F_M}$ to positioning errors at poses throughout the workspace must be found. To do this, the workspace was discretized using uniformly distributed poses in the allowed workspace. The positioning errors at these poses were then minimized. This is one way to ensure best positioning performance throughout the workspace. 3409 uniformly distributed poses were chosen for this purpose. The equations relating ${}_{H1}\mathcal{E}_{\Delta F_M}$ to the errors in poses attained (at 3409 uniformly distributed poses) after compensation are given by

$$ {}^{FE,r}_{H1}\mathcal{E}^{st}_{X_A} \approx -\overbrace{{}^{r}_{H1}A^{st}_{D}\ {}^{as}_{H1}A_M{}^{+}\ {}^{ap}_{H1}D}^{{}^{r}_{H1}Z^{st}}\ {}_{H1}\mathcal{E}_{\Delta F_M} \tag{4.16} $$

$$ {}^{FE,t}_{H1}\mathcal{E}^{st}_{X_A} \approx -\overbrace{{}^{t}_{H1}A^{st}_{D}\ {}^{as}_{H1}A_M{}^{+}\ {}^{ap}_{H1}D}^{{}^{t}_{H1}Z^{st}}\ {}_{H1}\mathcal{E}_{\Delta F_M} \tag{4.17} $$

In these equations, the right superscript 'st' indicates that the corresponding matrices/arrays from equations 4.14 and 4.15 are stacked row-wise and they correspond to 3409

5. See section 2.4 for more explanation.

arrays of ${}^{FE,r}_{H1}\mathcal{E}_{X_A}$ and ${}^{FE,r}_{H1}\mathcal{E}_{X_A}$. ${}^{r}_{H1}Z^{st}$ and ${}^{t}_{H1}Z^{st}$ can be used to optimize positioning after compensation at the 3409 target poses in the workspace. The sizes of ${}^{FE,r}_{H1}\mathcal{E}_{X_A}$ and ${}^{r}_{H1}Z^{st}$ are 10227×1 and 10227×30, respectively. ${}^{FE,t}_{H1}\mathcal{E}_{X_A}$ and ${}^{t}_{H1}Z^{st}$ have sizes similar to ${}^{FE,r}_{H1}\mathcal{E}_{X_A}$ and ${}^{r}_{H1}Z^{st}$, respectively.

Table 4.1: Approximate values of stiffness parameters evaluated for the hexapod studied in section 4.3.1

Approximate stiffness parameter values (N/µm)					
${}^{ap}_{H1}k_1$	${}^{ap}_{H1}k_2$	${}^{ap}_{H1}k_3$	${}^{ap}_{H1}k_4$	${}^{ap}_{H1}k_5$	${}^{ap}_{H1}k_6$
10.51	12.11	12.59	10.86	11.57	11.03

An information important for formulating FEIR criterion for this case is that the errors in applied forces/moments are due to the offset of the center of mass from its assumed position. This offset produces undesired moments about the X and Y axes of the platform. This implies that ${}_{H1}\mathcal{E}_{\Delta F_M}$ can have non-zero terms in its fourth and fifth elements. Due to the redundant nature of ${}_{H1}\mathcal{E}_{\Delta F_M}$, the fourth and fifth elements also repeat themselves at the appropriate spots within this array[6]. The elements of ${}^{r}_{H1}Z^{st}$ and ${}^{t}_{H1}Z^{st}$ that scale these elements of ${}_{H1}\mathcal{E}_{\Delta F_M}$ had to be minimized. Furthermore, the elements of ${}^{r}_{H1}Z^{st}$ and ${}^{t}_{H1}Z^{st}$ that couple with the fourth and fifth elements of ${}_{H1}\mathcal{E}_{\Delta F_M}$ also repeat themselves at appropriate spots in these matrices. Consequently, minimizing the terms of ${}^{r}_{H1}Z^{st}$ and

6. For instance, the 4^{th} element of ${}_{H1}\mathcal{E}_{\Delta F_M}$ repeats itself at 10^{th}, 16^{th}, 22^{nd} and 28^{th} spots.

${}^{t}_{H1}Z^{st}$ that couple with fourth and fifth elements of ${}_{H1}\mathcal{E}_{\Delta F_M}$ will also minimize the other relevant terms of ${}^{r}_{H1}Z^{st}$ and ${}^{t}_{H1}Z^{st}$. Therefore, the following minimization can be done:

$$\begin{aligned}
\min_{{}_{H1}X_M} \quad & \{f_3, f_4, f_5, f_6\} \\
\text{s.t.} \quad & \text{Workspace constraints} \\
\text{where,} \quad & f_3 = max(E^t) \\
& f_4 = avg(E^t) \\
& f_5 = max(E^r) \\
& f_6 = avg(E^r) \\
& E^t_i = norm_2\left({}^{t}_{H1}Z^{st}_{i,4}\ {}^{t}_{H1}Z^{st}_{i,5}\right); i = 1...10227 \\
& E^r_i = norm_2\left({}^{r}_{H1}Z^{st}_{i,4}\ {}^{r}_{H1}Z^{st}_{i,5}\right); i = 1...10227
\end{aligned} \tag{4.18}$$

${}_{H1}X_M$ in equation 4.18 is the identification pose. E^t_i and E^r_i are the i^{th} elements of E^t and E^r, respectively. ${}^{t}_{H1}Z^{st}_{i,j}$ and ${}^{r}_{H1}Z^{st}_{i,j}$ are the j^{th} elements of the i^{th} rows of ${}^{t}_{H1}Z^{st}$ and ${}^{r}_{H1}Z^{st}$, respectively. The optimization problem of equation 4.18 leads to a number of Pareto solutions. The best solution was obtained using the *method of global criterion* [Miettinen, 1999], similar to the manner in which the optimal solution was chosen for the optimization problem of equation 3.20 of chapter 3. Subsequently, the best pose obtained for stiffness identification for this case was [14.3 mm −1.8 mm −4.3 mm 0° 0° −3.67°].

Stiffness identification experiment was performed at the best pose obtained for this case. To accomplish this, the hexapod's platform was commanded to the identified best pose for stiffness identification. The platform's pose was measured [7] five times without the mass (121.25 kg) mounted on its platform first. Following this, the mass was mounted and the platform's pose was measured five times again. The variance and correlation of the deflection measurements were computed and matrix ${}_{H1}G_C$ was formulated as per equation 1.23. The set of six stiffness parameters was then identified using least squares method. Table 4.2 lists the identified optimal stiffness parameter set.

7. Using the pose measurement method outlined in appendix A.

Table 4.2: Optimal values of stiffness parameters identified for the hexapod using the method described in section 4.3.1

Optimal stiffness parameter values (N/μm)					
${}^{op}_{H1}k_1$	${}^{op}_{H1}k_2$	${}^{op}_{H1}k_3$	${}^{op}_{H1}k_4$	${}^{op}_{H1}k_5$	${}^{op}_{H1}k_6$
11.46	12.05	11.68	10.43	12.99	11.70

4.3.2 Evaluation of compensation efficiency

In order to assess the efficiency of compensation using estimated stiffness parameters (table 4.3.1), positioning errors of the hexapod's platform were measured: (a) without load, (b) with load and without elastostatic error compensation, and (c) with load and with elastostatic error compensation. These positioning experiments were performed at different poses along the X and Y axes of the hexapod. These poses are listed in table 4.3 and visually described in figure 4.4. The pose measurements were performed using the method [8] outlined appendix H. The mass mounted on the hexapod during these positioning experiments was 121.25 kg.

Table 4.3: Poses of hexapod's platform at which positioning experiments were performed

Poses along	Pose parameters					
	Tx (mm)	Ty (mm)	Tz (mm)	Rx (deg)	Ry (deg)	Rz (deg)
X-axis	-60	0	0	0	0	0
	-30					
	0					
	30					
	60					
Y-axis	0	-60	0	0	0	0
		-30				
		0				
		30				
		60				

8. The pose measurement method outlined in appendix H was used instead of the one in appendix A because latter is susceptible to thermal deflections of the hexapod when pose measurements need to be performed for long duration, unlike the former one. The pose measurements to be performed for the validation study in section 4.3.2 was bound to take long time. Consequently, pose measurement method outlined in appendix H was used for pose measurement in this case.

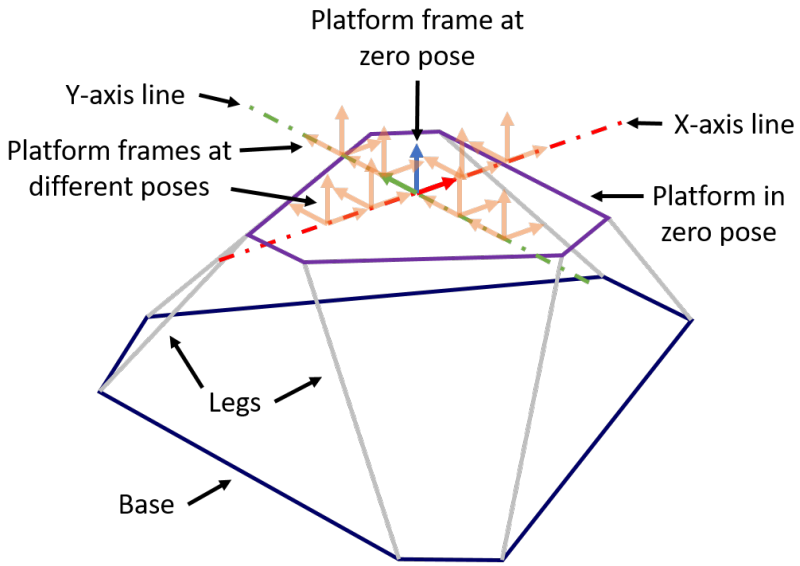

Figure 4.4: Visual description of platform frame poses at which compensation efficiency was evaluated

Figures 4.5 and 4.6 show the measured errors in poses attained by the hexapod's platform ($\mathcal{E}_{Tx}$, $\mathcal{E}_{Ty}$,...,$\mathcal{E}_{Rz}$) at the poses listed in table 4.3. These measured pose errors are the difference between the measured and target poses. Several trials of these measurements were performed and the results were found to be very repeatable ($< \pm 1\mu m$ for translations and $< \pm 2\mu rad$ for rotations). Consequently, results of just one trial are presented. These measured pose errors are a consequence of: (a) errors in geometric parameters, (b) errors in stiffness parameters (for cases where compensation is done), and (c) error in measured reference coordinate frame[9]. Since the purpose here is to evaluate the efficiency of elastostatic error compensation, measured pose errors of the loaded hexapod (with and without compensation) must be compared with measured pose errors without load. With this comparative framework in mind, one can see (in figures 4.5 and 4.6) that elastostatic error compensation using the identified stiffness parameters works very well. The loaded hexapod with elastostatic error compensation is able to reach the level of accuracy of the hexapod without load. Tables 4.4 and 4.5 present some quantitative metrics to assess the level of improvement in positioning accuracy with the use of elastostatic error compen-

9. This is the coordinate frame with respect to which all poses were measured.

sation. It can be seen that the maximum of differences between measured pose errors of the loaded hexapod with compensation and the hexapod without load are less than 5.48 μm for translations and 23.9 μrad for rotations, as compared to 31.25 μm and 90.27 μrad for loaded hexapod without compensation. Furthermore, the RMS values of differences between measured pose errors of the loaded hexapod with compensation and the hexapod without load are less than 3.28 μm for translations and 12.86 μrad for rotations, as compared to 26.08 μm and 49.49 μrad for loaded hexapod without compensation.

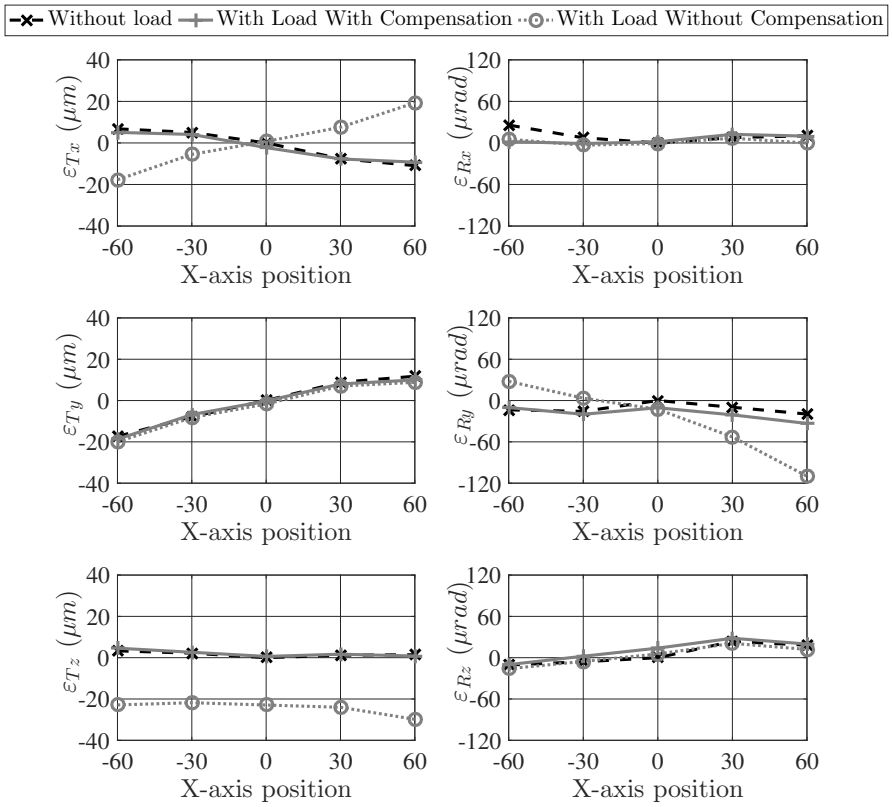

Figure 4.5: Measured errors in poses attained by the hexapod's platform at poses along X-axis

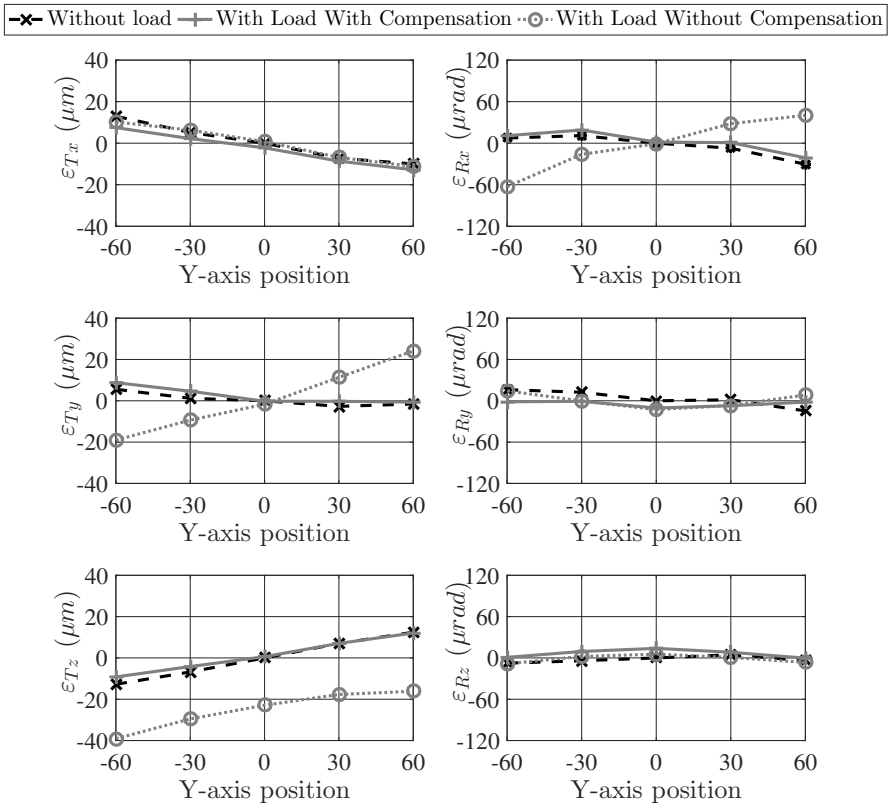

Figure 4.6: Measured errors in poses attained by the hexapod's platform at poses along Y-axis

Table 4.4: Comparing measured pose errors of loaded hexapod (with and without compensation) with those of the hexapod without mounted load, for poses measured along its X-axis

Axis	$\xi_{max,WC}$	$\xi_{max,WoC}$	$\xi_{RMS,WC}$	$\xi_{RMS,WoC}$
Tx	2.25 µm	30.24 µm	1.53 µm	19.26 µm
Ty	1.79 µm	2.95 µm	1.17 µm	2.09 µm
Tz	1.29 µm	31.25 µm	0.75 µm	26.08 µm
Rx	23.92 µrad	20.47 µrad	11.55 µrad	11.35 µrad
Ry	13.65 µrad	90.27 µrad	9.44 µrad	49.49 µrad
Rz	13.90 µrad	6.14 µrad	7.49 µrad	4.54 µrad

$\xi_{max,WC}$ and $\xi_{RMS,WC}$ are the maximum and RMS values of absolute differences between measured pose errors of hexapod without load and those of hexapod with load & with compensation, respectively.; $\xi_{max,WoC}$ and $\xi_{RMS,WoC}$ are the maximum and RMS values of absolute differences between measured pose errors of hexapod without load and those of hexapod with load & without compensation, respectively.

Table 4.5: Comparing measured pose errors of loaded hexapod (with and without compensation) with those of the hexapod without mounted load, for poses measured along its Y-axis

Axis	$\Xi_{max,WC}$	$\Xi_{max,WoC}$	$\Xi_{RMS,WC}$	$\Xi_{RMS,WoC}$
Tx	5.48 µm	2.75 µm	3.28 µm	1.48 µm
Ty	3.44 µm	25.74 µm	2.41 µm	17.77 µm
Tz	3.55 µm	28.58 µm	1.99 µm	25.15 µm
Rx	9.33 µrad	70.69 µrad	6.79 µrad	48.84 µrad
Ry	17.54 µrad	23.18 µrad	12.86 µrad	13.66 µrad
Rz	13.90 µrad	6.34 µrad	9.73 µrad	4.25 µrad

$\Xi_{max,WC}$ and $\Xi_{RMS,WC}$ are the maximum and RMS values of absolute differences between measured pose errors of hexapod without load and those of hexapod with load & with compensation, respectively.; $\Xi_{max,WoC}$ and $\Xi_{RMS,WoC}$ are the maximum and RMS values of absolute differences between measured pose errors of hexapod without load and those of hexapod with load & without compensation, respectively.

4.4 Experimental study 2: validation of FEIR criterion

In this section, an experimental study is presented which was performed to validate the FEIR criterion. This study was performed on the hexapod shown in figures 4.1 and 4.2, and using the measurement and loading apparatuses shown in them.

In order to validate FEIR criterion, a simple scenario of elastostatic calibration was considered. In this, elastostatic calibration of the hexapod was required to achieve best possible positioning along its Tz axis and at poses listed in table 4.3, with a mass of 121.25 kg mounted on its platform. The force/moment to be applied for stiffness identification was fixed. Stiffness identification experiments were then performed at: (a) best poses for stiffness identification as per FEIR criterion [10], (b) respective target poses, and (c) the zero pose. Each of these stiffness identification experiments was performed with a high error in force/moment applied at the platform. The compensation qualities using stiffness parameters identified at each of these identification poses were then compared.

For stiffness identification at the various poses listed above, the force/moment was applied on the platform by mounting a mass of 121.25 kg (as shown in figure 4.2) on it.

10. One pose for stiffness identification was chosen for each target pose.

However, the force/moment that was assumed to have been applied [11] had an extra moment of 1000 Nm about the X-axis (M_x). This big error in applied load was introduced to clearly show the problem and improvement (using the proposed optimization). The errors in identified stiffness parameters would, in this case, be dominated by errors (in thereof) due to applied force/moment error. Owing to this, only one deflection measurement was enough for each stiffness identification experiment.

The remaining part of this section is organized as follows: section 4.4.1 presents the details about stiffness identification optimization using FEIR criterion. This is followed by section 4.4.2 which presents the details of experiments performed to validate the improvement in compensation quality when FEIR criterion are used to optimize stiffness identification.

4.4.1 Stiffness identification optimization

For performing stiffness identifications as per choices described above, the stiffness identification equation can be written for this case first. Equation 2.6 can be rewritten for this case as

$$ {}_{H2}G\ {}^{as}_{H2}A_M\ {}_{H2}H\ {}_{H2}H^{-1}\ (\ {}_{H2}c + {}^{Du}_{H2}\mathcal{E}_c + {}^{FE}_{H2}\mathcal{E}_c) = {}_{H2}G\ ({}_{H2}\Delta X_M + {}^{Du}_{H2}\mathcal{E}_{\Delta X_M} + {}^{FE}_{H2}\mathcal{E}_{\Delta X_M}) \tag{4.19} $$

Left subscript "H2" of the variables in the above equation specifies that the corresponding matrices/arrays of equation 2.6 have been formulated for this case. Matrix ${}_{H2}G$ is a 6×6 identity matrix. This is because only one measurement is performed in each stiffness identification experiment in this case, resulting in zero variance of measured deflections. Matrix ${}^{as}_{H2}A_M$ is the observation matrix which is a function of the identification pose used in each stiffness identification experiment and the forces/moments assumed to have been applied in them. Matrix ${}_{H2}H$ is a 6×6 identity matrix since the stiffness parameters are expected to have the same order of magnitude. This is because every leg of the given hexapod has the same design and materials. ${}_{H2}\Delta X_M$, ${}^{Du}_{H2}\mathcal{E}_{\Delta X_M}$ and ${}^{FE}_{H2}\mathcal{E}_{\Delta X_M}$ are 6×1 vectors which

11. ${}^{as}\Delta F_M$ from equation 2.1.

together constitute the measured deflections. ${}^{Du}_{H2}\mathcal{E}_{\Delta X_M}$ and ${}^{FE}_{H2}\mathcal{E}_{\Delta X_M}$ contain the errors in measured deflections due to deflection measurement uncertainty and errors in force/moment applied during stiffness identification, respectively. Parameter set of equation 4.19 is estimated using least squares method. The errors in these estimated parameters were bound to be (mostly) a consequence of errors in forces/moments applied during stiffness identification. This is a consequence of the large error in force/moment applied for stiffness identification.

In order to formulate a FEIR criterion for this case, matrix Z (from equation 2.51) must be formulated first. This is because this matrix relates the errors in forces/moments applied during stiffness identification to the resultant errors in poses attained after compensation. Equation 2.51 can be rewritten for this case as

$$ {}^{FE}_{H2}\mathcal{E}_{X_A} \approx -\overbrace{{}_{H2}A_D \, {}^{as}_{H2}A_M{}^{+} \, {}^{ap}_{H2}D}^{{}_{H2}Z} \; {}_{H2}\mathcal{E}_{\Delta F_M} \tag{4.20} $$

In equation 4.20, ${}_{H2}Z$ and ${}^{ap}_{H2}D$ are 6×6 matrices. ${}^{ap}_{H2}D$ was computed (as per equation 2.43) using the approximate values of stiffness parameter values listed in table 4.1. ${}_{H2}\mathcal{E}_{\Delta F_M}$ is the 6×1 array containing errors in forces/moments applied during stiffness identification and ${}^{FE}_{H2}\mathcal{E}_{X_A}$ is the 6×1 array containing the resultant errors in poses attained after compensation. Since the applied force/moment error is a moment about the X-axis and best positioning performance was desired along Tz axis, identification pose that minimizes the fourth element of the third row of ${}_{H2}Z$, ${}_{H2}Z_{34}$, had to be found. This is because ${}_{H2}Z_{34}$ scales the element of ${}_{H2}\mathcal{E}_{\Delta F_M}$ corresponding to the moment about X-axis to contribute to the element of ${}^{FE}_{H2}\mathcal{E}_{X_A}$ corresponding to platform's Tz axis. The minimization problem to find an identification pose for each of the target poses listed in table 4.3 can be written as

$$ \begin{aligned} \min_{{}_{H2}X_M} \quad & {}_{H2}Z_{34} \\ \text{s.t.} \quad & \text{Workspace constraints} \end{aligned} \tag{4.21} $$

where ${}_{H2}X_M$ is the identification pose. ${}_{H2}Z_{34}$ from equation 4.21 was minimized to obtain one identification pose for each target pose. MATLAB optimization toolbox was

used to solve the optimization problem and obtain the best identification poses. These optimization routines are very sensitive to the starting point supplied. To tackle this, a large number of starting points were supplied so that the best solution could be found.

The deflection measurements were then performed at the identified best poses, the target poses and the zero pose. The mass weighing 121.25 kg (as in figure 4.2) was mounted on the platform during these stiffness identification experiments. The measured deflections and the "false assumed applied load" were used to estimate the stiffness parameters.

4.4.2 Evaluation of compensation efficiency

For validation of optimal parameter sets identified using FEIR criterion, positioning experiments were performed at poses listed in table 4.3. The platform was commanded to position at these poses with a mass of 121.25 kg mounted on its platform using command poses that were generated using: (a) the identified optimal parameter sets, (b) parameter set identified when stiffness identification was performed at zero pose, and (c) parameter sets identified when stiffness identification was performed at respective target poses. Errors in poses attained were then measured [12]. For the sake of comparison, errors in attained poses were also measured with the platform commanded to those poses without load. These positioning experiments were conducted multiple times and the results were found to be very repeatable ($< \pm 1\mu m$ for translations and $< \pm 2\mu rad$ for rotations). Owing to this, results of just one trial are presented here for analysis.

Figure 4.7 shows the measured errors in poses attained by the hexapod's platform at different poses. It can be seen that the best compensations were achieved using stiffness parameters identified at poses as per FEIR criterion. Two data points stand out in the obtained results (in figure 4.7): (a) pose error at pose [30 mm 0 mm 0 mm 0° 0° 0°] using parameters identified at the same pose, and (b) pose error at pose [0 mm −60 mm 0 mm 0° 0° 0°] using parameters identified at the best pose as per FEIR criterion. The reader is referred to figure 4.8 to gain an understanding of the reason behind (a). This figure shows values of ${}_{H2}Z_{34}$ for each of the poses along X-axis (listed in table 4.3) when stiffness identification is performed at the respective poses for positioning

12. Pose measurement method described in appendix H was used for this.

at the same pose. These values scale the error in forces/moments applied during stiffness identification to the Tz-axis error in pose attained after compensation. As can be seen in figure 4.8, the large error in (a) is due to the scaling provided by ${}_{H2}Z_{34}$ for this particular case. The magnitude of ${}_{H2}Z_{34}$ is approximately 11.7 times larger for the pose [30 mm 0 mm 0 mm 0° 0° 0°] as compared to the other poses in figure 4.8. This correlates with the observation in figure 4.7, i.e., the magnitude of positioning error is approximately 11.7 times larger for pose [30 mm 0 mm 0 mm 0° 0° 0°] as compared to the other poses along X-axis when stiffness identification is performed at those respective poses. Regarding (b), two possibilities exist for the reason behind the error in pose attained for the best case scenario (using FEIR criterion) not reaching the ideal level (measured accuracy of hexapod without load). One is that the matrix ${}_{H2}Z$ possible under the given workspace constraints can't completely eliminate the impact of the applied load error [13] considered in this case on the positioning task intended in this case. The second reason could be that the best solution was not found in the optimization routine. The second possibility is highly unlikely because optimization was carefully performed using a large number of starting points.

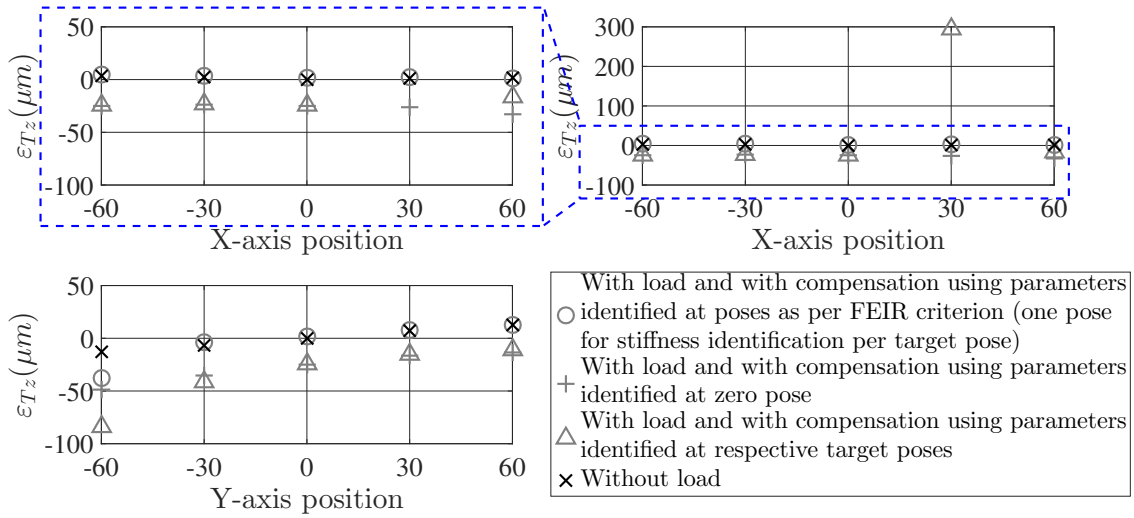

Figure 4.7: Measured errors in poses attained by the hexapod's platform, along its Tz axis, at poses listed in table 4.3

13. During stiffness identification.

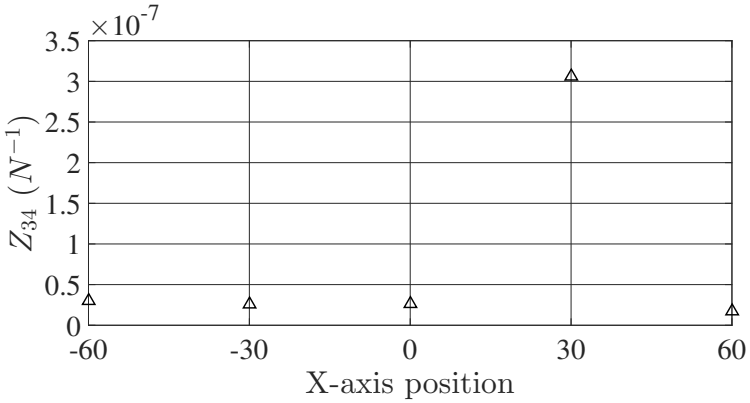

Figure 4.8: Values of ${}_{H2}Z_{34}$ for each of the poses along X-axis listed in table 4.3 when stiffness identification is performed at the respective poses for positioning at the same pose

4.5 Conclusion

This chapter presented experimental studies on elastostatic calibration of a high-precision positioning hexapod. The aims of these studies were to experimentally validate elastostatic calibration of the hexapod and to experimentally validate the FEIR criterion. Validation of DUIR criterion was not performed because it was not possible with the setup available. In the first experimental study, elastostatic calibration of hexapod was performed to achieve best possible positioning performance along all the axes of the platform and throughout its workspace. The estimated parameters were used to compensate the pose errors of the loaded hexapod at different poses. Results confirmed the efficacy of developed elastostatic calibration framework and the estimated stiffness parameters in compensating for positioning accuracy deteriorated due to load on the platform. In the second experimental study, stiffness identification experiments were performed at poses suggested by FEIR criterion and some other poses. Parameters estimated in these stiffness identification experiments were used to compensate the pose errors of the loaded hexapod at different poses. Results confirmed the efficacy of FEIR criterion in obtaining best compensation quality.

Conclusions

Here, general conclusions of this thesis are presented. The prime contributions of this thesis are highlighted first. This is followed by some recommendations for future work.

Contributions of this thesis

The contributions of this thesis can be summarized as follows:

1. A ***new approach to optimize stiffness identification*** for robot elastostatic calibration: This is a framework to formulate criteria to choose the best set of poses and forces/moments for stiffness identification of non-over-constrained robots in which compliance can be considered only in actuated joints. The parameters identified under experimental conditions (poses and forces/moments) suggested by these criteria ensure minimum impact of deflection measurement uncertainty and errors in forces/moments applied during stiffness identification on compensation quality. Furthermore, it also maximizes positioning accuracy at desired pose(s), along desired axe(s) of the end-effector/platform and with desired forces/moments on the end-effector/platform. Validation studies documented in this thesis confirm the efficacy of this framework. This stiffness identification optimization framework was developed to enable best possible compensation of positioning errors due to com-

pliance of robots in predefined applications. This aspect is very important in high-precision applications in which the robot's positioning specifications are predefined.

2. ***Elastostatic calibration of hexapod***: Elastostatic calibration of a high-precision hexapod positioning system was accomplished. The stiffness of this hexapod was modelled using a lumped stiffness model. The parameters of this model were identified at best poses and forces/moments as per the criteria formulated using the proposed stiffness identification optimization framework. The identified parameters were then used to compensate for the pose errors (due to compliance) of the loaded hexapod. Results showed that the loaded hexapod with compensation using identified stiffness parameters can achieve the level of accuracy of the unloaded hexapod. Elastostatic calibration of hexapod is necessary to facilitate high-accuracy 6-DOF positioning when a heavy payload is mounted on a high-precision positioning hexapod.
3. ***Thermal deflection decoupled 6-DOF pose measurement method for hexapods***: A method was developed to eliminate the influence of thermal deflection of a hexapod on the measured 6-DOF pose of its platform. This was validated experimentally using pose measurements of a high-precision hexapod using a CMM. This method is necessary to ensure that the thermal deflections of the hexapod do not impact pose measurement of hexapods. This was crucial in some tests that were performed to validate methods developed in this thesis. Furthermore, this method is also beneficial for robot geometric calibration which requires pose measurements at constant temperature, which is difficult and expensive to achieve.

Recommendations for future work

The work documented in this thesis solves many problems. Additionally, it also opens up new research directions that can be explored. Some of them are:

1. ***Using presented parameter identification optimization method for optimizing robot geometric calibration***: In this thesis, a framework for formulating criteria to choose best measurement conditions (poses and forces/moments) for stiffness iden-

tification is presented. The parametric calibration framework is similar for robot elastostatic and geometric calibrations. Also, one error source, uncertainty of deflection measurements performed, impacts parameter identification in both these calibration routines. Consequently, the framework for formulating criteria for minimizing the influence of this error on elastostatic calibration performance, the DUIR criterion, can also be used for minimizing the influence of this error on the performance of robot geometric calibration. Appendix I discusses this in further detail. Further investigations can be carried out on this.

2. ***Evaluating uncertainty of pose measurement***: Methods to evaluate the uncertainty of 6-DOF pose measurement methods, documented in appendixes A and H, must be developed. Alternatively, a new 6-DOF pose measurement method for hexapods can be developed in which the uncertainty of pose measurement can be evaluated easily. This is necessary to exploit the developed parameter identification optimization framework completely. Currently, the criterion to minimize the influence of deflection measurement uncertainty on compensation quality, DUIR criterion, can't be used with the pose measurement methods documented in appendices A and H. This is because, in order to use DUIR criterion, it is necessary to know the uncertainty of measured deflections. This, in turn, is dependent on the uncertainty of pose measurements performed.

3. ***Elastostatic calibration of large and heavy hexapods***: The method documented in this thesis to perform elastostatic calibration of hexapods must be tested for large and heavy hexapods. The stiffness modelling method for hexapod used in this thesis assumes that the legs are light enough to cause negligible deflections of the hexapod's components. In large and heavy hexapods, this assumption might not hold true [Klimchik et al., 2014]. If this assumption does indeed not hold true for large and heavy hexapods, the stiffness model needs to be amended.

Bibliography

Eberhard Abele, Matthias Weigold, and Stefan Rothenbücher. Modeling and identification of an industrial robot for machining applications. *CIRP annals*, 56(1):387–390, 2007. Cited pages 33 and 34.

Gürsel Alici and Bijan Shirinzadeh. Enhanced stiffness modeling, identification and characterization for robot manipulators. *IEEE transactions on robotics*, 21(4):554–564, 2005. Cited page 34.

H Alemi Ardakani and TJ Bridges. Review of the 3-2-1 euler angles: a yaw-pitch-roll sequence, 2010. Cited page 115.

K Somani Arun, Thomas S Huang, and Steven D Blostein. Least-squares fitting of two 3-d point sets. *IEEE Transactions on pattern analysis and machine intelligence*, (5):698–700, 1987. Cited page 147.

Anthony Atkinson, Alexander Donev, and Randall Tobias. *Optimum experimental designs, with SAS*, volume 34. Oxford University Press, 2007. Cited pages 47, 48, and 50.

Thomas Bonnemains, Hélène Chanal, Belhassen-Chedli Bouzgarrou, and Pascal Ray. Stiffness computation and identification of parallel kinematic machine tools. *Journal of manufacturing science and engineering*, 131(4):041013, 2009. Cited page 34.

J-H Borm and C-H Menq. Experimental study of observability of parameter errors in robot calibration. In *Proceedings, 1989 International Conference on Robotics and Automation*, pages 587–592. IEEE, 1989. Cited pages 50 and 52.

BC Bouzgarrou, JC Fauroux, G Gogu, and Y Heerah. Rigidity analysis of t3r1 parallel robot with uncoupled kinematics. In *Proceedings Of the 35th International Symposium on Robotics, Paris, France, 2004*. IFR, 2004. Cited page 35.

Giuseppe Carbone and Marco Ceccarelli. A procedure for experimental evaluation of cartesian stiffness matrix of multibody robotic systems. In *15th CISM-IFToMM Symposium on Robot Design, Dynamics and Control, Romansy*, 2006. Cited page 34.

Henry Carrillo, Oliver Birbach, Holger Täubig, Berthold Bäuml, Udo Frese, and José A Castellanos. On task-oriented criteria for configurations selection in robot calibration. In *2013 IEEE International Conference on Robotics and Automation*, pages 3653–3659. IEEE, 2013. Cited pages 50 and 54.

Joe Chalfoun, Catherine Bidard, Delphine Keller, and Yann Perrot. Calibration using generalized error matrices of a long reach articulated carrier. In *2007 IEEE International Conference on Automation Science and Engineering*, pages 777–782. IEEE, 2007. Cited pages 33 and 34.

J Chen and F Lan. Instantaneous stiffness analysis and simulation for hexapod machines. *Simulation Modelling Practice and Theory*, 16(4):419–428, 2008. Cited page 34.

Shih-Feng Chen and Imin Kao. Conservative congruence transformation for joint and cartesian stiffness matrices of robotic hands and fingers. *The International Journal of Robotics Research*, 19(9):835–847, 2000. Cited page 41.

Chen-Gang, Li-Tong, Chu-Ming, Jia-Qing Xuan, and Sun-Han Xu. Review on kinematics calibration technology of serial robots. *International Journal of Precision Engineering and Manufacturing*, 15(8):1759–1774, Aug 2014. ISSN 2005-4602. doi: 10.1007/s12541-014-0528-1. URL https://doi.org/10.1007/s12541-014-0528-1. Cited page 32.

Charles M Clinton, Guangming Zhang, and Albert J Wavering. Stiffness modeling of a stewart platform based milling machine. Technical report, 1997. Cited page 34.

Charles Corradini, Jean-Christophe Fauroux, Sébastien Krut, et al. Evaluation of a 4-degree of freedom parallel manipulator stiffness. In *Proceedings of the 11th World Congress in Mechanisms and Machine Science, Tianjin (China)*, 2003. Cited page 35.

Dominique Deblaise, Xavier Hernot, and Patrick Maurine. A systematic analytical method for pkm stiffness matrix calculation. In *Proceedings 2006 IEEE International Conference on Robotics and Automation, 2006. ICRA 2006.*, pages 4213–4219. IEEE, 2006. Cited pages 34 and 35.

Morris R Driels and Uday S Pathre. Significance of observation strategy on the design of robot calibration experiments. *Journal of Robotic Systems*, 7(2):197–223, 1990. Cited pages 48, 50, and 53.

Claire Dumas. *Development of methods for metal and composite parts trimming with a robot*. Theses, Université de Nantes, December 2011. URL https://tel.archives-ouvertes.fr/tel-00712458. Cited pages 21, 27, 33, and 34.

P Gangan. Tu delft spin-off ampelmann hits major milestone. https://www.delta.tudelft.nl/article/tu-delft-spin-ampelmann-hits-major-milestone. Cited pages 1 and 19.

Chunhe Gong, Jingxia Yuan, and Jun Ni. Nongeometric error identification and compensation for robotic system by inverse calibration. *International Journal of Machine Tools and Manufacture*, 40(14):2119 – 2137, 2000. ISSN 0890-6955. doi: https://doi.org/10.1016/S0890-6955(00)00023-7. URL http://www.sciencedirect.com/science/article/pii/S0890695500000237. Cited pages 27, 33, and 34.

Clement Gosselin. Stiffness mapping for parallel manipulators. *IEEE Transactions on Robotics and Automation*, 6(3):377–382, 1990. Cited pages 36 and 37.

M Griffis and J Duffy. Global stiffness modeling of a class of simple compliant couplings. *Mechanism and machine theory*, 28(2):207–224, 1993. Cited page 36.

Samad Hayati, Kam Tso, and Gerald Roston. Robot geometry calibration. In *Proceedings of IEEE International Conference on Robotics and Automation*, pages 947–951. IEEE, 1988. doi: 10.1109/ROBOT.1988.12181. Cited page 27.

Junichi Imoto, Yukio Takeda, Hidenobu Saito, and Ken Ichiryu. Optimal kinematic calibration of robots based on maximum positioning-error estimation (theory and application to a parallel-mechanism pipe bender). In *Computational Kinematics*, pages 133–140. Springer, 2009. Cited page 54.

ISO. Iso-10360-1:2000: Geometrical product specifications (gps)-acceptance and reverification tests for coordinate measuring machines (cmm), part 1: Vocabulary, 2000. Cited pages 111 and 177.

Ahmed Joubair and Ilian A Bonev. Comparison of the efficiency of five observability indices for robot calibration. *Mechanism and Machine Theory*, 70:254–265, 2013. Cited page 48.

Nolwenn Kammerer and Yann Perrot. High accuracy patient positioning system: geometric and elastic error calibration of a flexible model. In *2012 IEEE International Conference on Automation Science and Engineering (CASE)*, pages 1033–1039. IEEE, 2012. Cited pages 33 and 34.

Wisama Khalil and Sébastien Besnard. Geometric calibration of robots with flexible joints and links. *Journal of Intelligent and Robotic systems*, 34(4):357–379, 2002. Cited page 33.

Wisama Khalil and Etienne Dombre. *Modeling, identification and control of robots*. Butterworth-Heinemann, 2004. Cited page 41.

Alexandr Klimchik, Anatol Pashkevich, Yier Wu, Stéphane Caro, and Benoît Furet. Design of calibration experiments for identification of manipulator elastostatic parameters. *Journal of Mechanics Engineering and Automation*, 2:531–542, 2012. Cited page 45.

Alexandr Klimchik, Anatol Pashkevich, and Damien Chablat. Cad-based approach for identification of elasto-static parameters of robotic manipulators. *Finite Elements in Analysis and Design*, 75:19–30, 2013. Cited pages 34 and 35.

Alexandr Klimchik, Damien Chablat, and Anatol Pashkevich. Stiffness modeling for perfect and non-perfect parallel manipulators under internal and external loadings. *Mechanism and Machine Theory*, 79:1–28, 2014. Cited pages 35 and 135.

Yu-Wen Li, Jin-Song Wang, and Li-Ping Wang. Stiffness analysis of a stewart platform-based parallel kinematic machine. In *Proceedings 2002 IEEE International Conference on Robotics and Automation (Cat. No. 02CH37292)*, volume 4, pages 3672–3677. IEEE, 2002. Cited pages 34 and 35.

Chris Lightcap, Samuel Hamner, Tony Schmitz, and Scott Banks. Improved positioning accuracy of the pa10-6ce robot with geometric and flexibility calibration. *IEEE Transactions on Robotics*, 24(2):452–456, 2008. Cited pages 33 and 34.

Félix Majou, Clément Gosselin, Philippe Wenger, and Damien Chablat. Parametric stiffness analysis of the orthoglide. *Mechanism and machine theory*, 42(3):296–311, 2007. Cited page 34.

Marco A Meggiolaro, Steven Dubowsky, and Constantinos Mavroidis. Geometric and elastic error calibration of a high accuracy patient positioning system. *Mechanism and Machine Theory*, 40(4):415–427, 2005. Cited pages 33 and 34.

Chia-Hsiang Menq, Jin-Hwan Borm, and Jim Z Lai. Identification and observability measure of a basis set of error parameters in robot calibration. *Journal of Mechanisms, Transmissions, and Automation in Design*, 111(4):513–518, 1989. Cited page 48.

Jean-Pierre Merlet. *Parallel robots*, volume 128. Springer Science & Business Media, 2006. Cited page 40.

Kaisa Miettinen. *Nonlinear multiobjective optimization*. Kluwer Academic Publishers, 1999. Cited pages 101, 102, and 121.

Kiyoshi Nagai and Zhengyong Liu. A systematic approach to stiffness analysis of parallel mechanisms and its comparison with fem. In *SICE Annual Conference 2007*, pages 1087–1094. IEEE, 2007. Cited page 35.

Ali Nahvi and John M Hollerbach. The noise amplification index for optimal pose selection in robot calibration. In *Proceedings of IEEE International Conference on Robotics and Automation*, volume 1, pages 647–654. IEEE, 1996. Cited pages 50 and 53.

Ali Nahvi, John M Hollerbach, and Vincent Hayward. Calibration of a parallel robot using multiple kinematic closed loops. In *Proceedings of the 1994 IEEE International Conference on Robotics and Automation*, pages 407–412. IEEE, 1994. Cited pages 50 and 53.

Anatol Pashkevich, Alexandr Klimchik, and Damien Chablat. Enhanced stiffness modeling of manipulators with passive joints. *Mechanism and machine theory*, 46(5):662–679, 2011. Cited page 35.

Erik Rebeck and Guangming Zhang. A method for evaluating the stiffness of a hexapod machine tool support structure. *International Journal of Flexible Automation and Integrated Manufacturing*, 7(3/4):149–166, 1999. Cited page 34.

Renishaw. SP25M. https://www.renishaw.com/en/sp25m--6688. [Accessed: 2020-04-03]. Cited page 111.

ZVIS Roth, B Mooring, and Bahram Ravani. An overview of robot calibration. *IEEE Journal on Robotics and Automation*, 3(5):377–385, 1987. Cited page 27.

Serena Ruggeri, Angelo Vertuan, Giovanni Legnani, and Antonio Visioli. Kinetostatic calibration of a scara robot. In *XIX Congresso AIMETA, Associazione Italiana di meccanica teorica e applicata.–Ancona.–14-17 Settembre*, 2009. Cited page 34.

J Kenneth Salisbury. Active stiffness control of a manipulator in cartesian coordinates. In *1980 19th IEEE conference on decision and control including the symposium on adaptive processes*, pages 95–100. IEEE, 1980. Cited page 36.

Klaus Schröer. Theory of kinematic modelling and numerical procedures for robot calibration. *Robot Calibration*, 157196, 1993. Cited page 44.

George AF Seber and Alan J Lee. *Linear regression analysis*, volume 329. John Wiley & Sons, 2012. Cited pages 45, 51, and 78.

Jeff S Shamma and DE Whitney. A method for inverse robot calibration. *(Journal of Dynamic Systems, Measurement, and Control*, 1987. Cited page 33.

Bruno Siciliano and Oussama Khatib. *Springer handbook of robotics*. Springer-Verlag Berlin Heidelberg, 2008. Cited pages 40 and 44.

Alexander H Slocum. *Precision machine design*. Society of Manufacturing Engineers, 1992. Cited pages 1 and 20.

Herman Soemers. *Design principles for precision mechanisms*. T-Pointprint, 2011. Cited page 16.

Mark W Spong, Seth Hutchinson, Mathukumalli Vidyasagar, et al. *Robot modeling and control*. 2006. Cited page 147.

Doug Stewart. A platform with six degrees of freedom. *Proceedings of the institution of mechanical engineers*, 180(1):371–386, 1965. Cited pages 1, 16, and 17.

Yu Sun and John M Hollerbach. Observability index selection for robot calibration. In *2008 IEEE International Conference on Robotics and Automation*, pages 831–836. IEEE, 2008. Cited pages 50, 54, 87, and 182.

Symétrie. Vacuum mirror adjustment. https://www.symetrie.fr/en/applications-2/vacuum-mirror-adjustment/, a. Accessed: 2020-01-21. Cited pages 3 and 151.

Symétrie. Wave basin. https://www.symetrie.fr/en/applications-2/wave-basin/, b. Accessed: 2020-03-15. Cited pages 1 and 19.

Symétrie. Hexapods for synchrotrons. https://www.symetrie.fr/en/applications-2/synchrotrons/, c. Accessed: 2020-03-15. Cited pages 1 and 18.

Symétrie. Positioning Hexapods. https://www.symetrie.fr/en/products/positioning-hexapods/, d. [Accessed: 2020-03-04]. Cited page 111.

Symétrie. Telescope mirror adjustment. https://www.symetrie.fr/en/applications-2/telescope-mirror-adjustment/, e. Accessed: 2020-03-15. Cited pages 1 and 18.

TUDelft. Simona. http://cs.lr.tudelft.nl/simona/. Accessed: 2020-03-15. Cited pages 1 and 19.

Yier Wu. *Optimal pose selection for the identification of geometric and elastostatic parameters of machining robots*. Theses, Ecole des Mines de Nantes, January 2014. URL https://tel.archives-ouvertes.fr/tel-00983277. Cited pages 21, 27, 33, 34, 36, 50, and 54.

Jian Zhou and Hee-Jun Kang. A hybrid least-squares genetic algorithm–based algorithm for simultaneous identification of geometric and compliance errors in industrial robots. *Advances in Mechanical Engineering*, 7(6):1687814015590289, 2015. Cited pages 33 and 34.

APPENDIX

A

A method to measure the 6-DOF pose of hexapod's platform

Here, a method is presented which can be used to perform 6-DOF pose measurements of hexapod's platform using a coordinate measurement machine (CMM). Section A.1 provides the details of the measurement setup required for this measurement and section A.2 presents the measurement method.

A.1 Measurement setup

Figure A.1 shows the test setup required for this measurement. It consists of the hexapod fixed to the granite table of a CMM by means of an appropriate fixture. The platform of the hexapod have precision balls screwed to them. At least three precision balls must be used due to reasons stated in section A.2. The setup shown in figure A.1 contains three of these precision balls.

A.2 Measurement method

Pose measurements are always performed by measuring several points using a measurement system. Here, this measurement system is the CMM. Let M be the coordinate frame of the CMM. A coordinate frame fixed to the platform defines the pose of the plat-

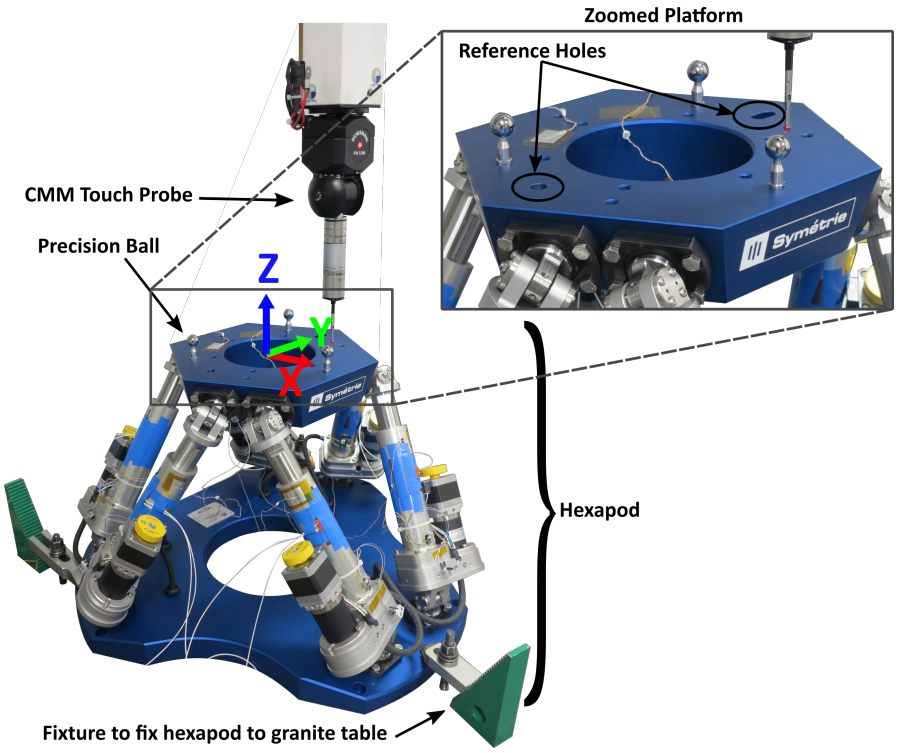

Figure A.1: Test setup used for pose measurement of hexapod

form. For Symétrie's hexapods, this is usually at the center of the platform as shown in figure A.1. The coordinate frame fixed to the platform of the hexapod is first measured with the hexapod commanded to be in zero pose [1]. All poses of the hexapod's platform are expressed with respect to this coordinate frame. This coordinate frame is identified by measuring several points in reference holes (see figure A.1) and on surfaces of the platform. Let this coordinate frame be called O (see figure A.2). The centers of the precision balls fixed to the platform ($p_{1,i}$ with $i = 1..3$) are then measured. To do this, several points on the surface of each precision ball are measured. The positions of the centers of these spheres are then expressed in the coordinate frame O. Let the position vectors of these points be called $p^{O}_{1,i}$ ($i = 1..3$). The platform can then be commanded to any desired pose. Consequently, the platform frame attains a new pose. Let this new coordinate frame be called S. With the platform in the new desired pose, the new positions of the precision

1. This is the pose of the platform in which all its pose parameters (defining the 3 translations and 3 rotations) are zero. In this pose, all the legs are locked at the center of their strokes and have the same length.

balls ($p_{2,i}$ with $i = 1..3$) are measured and expressed in the coordinate frame O. Let the position vectors of these points be called $p^O_{2,i}$ ($i = 1..3$).

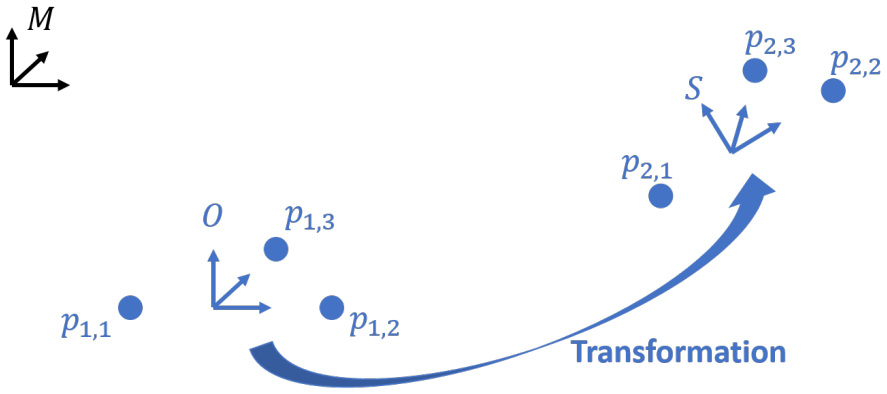

Figure A.2: Illustration of the measurement method

The task is then to obtain the pose parameters defining the transformation [Spong et al., 2006] between the coordinate frames O and S. In order to do this, the following relation is first considered:

$$p^S_{2,i} = p^O_{1,i} \; ; \; i = 1..3 \tag{A.1}$$

In equation A.1, $p^S_{2,i}$ are the points $p_{2,i}$ expressed in the coordinate frame S. Equation A.1 means that the positions of the centers of spheres do not change with respect to the platform frame when the platform moves and this is true. We then have,

$$\begin{bmatrix} p^O_{2,i} \\ 1 \end{bmatrix} = T^O_S \begin{bmatrix} p^S_{2,i} \\ 1 \end{bmatrix} \; ; \; i = 1..3 \tag{A.2}$$

In equation A.2, T^O_S is the transformation matrix that transforms the points expressed in the frame S to points expressed in the frame O. $p^O_{2,i}$ and $p^O_{2,i}$ are already known from measurements. T^O_S can then be obtained using the method outlined by [Arun et al., 1987]. This method requires i to be at least three. As a result, at least three precision balls are needed to perform pose measurement as per the method outlined here.

APPENDIX

B

Proof of $(G_C\ {}^{Du}\mathcal{E}_{\Delta X_M})$ being I.I.D and dimensionless

To prove that $(G_C\ {}^{Du}\mathcal{E}_{\Delta X_M})$ is independent and identically distributed, it needs to be shown that $Cov(\ {}_iS^{-1}\ {}^{Du}\mathcal{E}^i_{\Delta X_M})$ is a diagonal matrix containing same numbers along its diagonal (equal variances). Equations 1.23 and 1.24 give us

$$\begin{aligned} Cov(\ {}_iS^{-1}\ {}^{Du}\mathcal{E}^i_{\Delta X_M}) &= {}_iS^{-1}\ Cov({}^{Du}\mathcal{E}^i_{\Delta X_M})\ {}_iS^{-T} && \text{(B.1)} \\ &= {}_iS^{-1}\ {}_iS\ {}_iS^{T}\ {}_iS^{-T} && \text{(B.2)} \\ &= I && \text{(B.3)} \end{aligned}$$

It can be seen from equations B.1, B.2 and B.3 that $(G_C\ {}^{Du}\mathcal{E}_{\Delta X_M})$ is independent and identically distributed.

The elements of the j^{th} column of ${}_iS^{-1}$ possess a unit which is the inverse of that of the j^{th} element of ${}^{Du}\mathcal{E}^i_{\Delta X_M}$. Consequently, the resulting measurement vector after scaling, $G_C\ {}^{Du}\mathcal{E}_{\Delta X_M}$, is dimensionless. In order to check this, let us consider a simple case where ${}^{Du}\mathcal{E}^i_{\Delta X_M}$ has two coordinates, one translational and the other rotational. Matrices ${}_iV$ and ${}_iS$ (refer equation 1.24), in this case, will have the following structure and units:

$$
{}_iV = \begin{bmatrix} {}_iV_{11}\,(m^2) & {}_iV_{12}\,(mrad) \\ {}_iV_{21}\,(mrad) & {}_iV_{22}\,(rad^2) \end{bmatrix} \tag{B.4}
$$

$$
= \begin{bmatrix} {}_iS_{11}\,(m) & {}_iS_{12}\,(m) \\ {}_iS_{21}\,(rad) & {}_iS_{22}\,(rad) \end{bmatrix} \begin{bmatrix} {}_iS_{11}\,(m) & {}_iS_{21}\,(rad) \\ {}_iS_{12}\,(m) & {}_iS_{22}\,(rad) \end{bmatrix} = {}_iS\,{}_iS^T \tag{B.5}
$$

Here, ${}_iV_{pq}$ and ${}_iS_{pq}$ are the p^{th} elements the q^{th} column of matrices ${}_iV$ and ${}_iS$, respectively. ${}_iS^{-1}$, for this case, can be written as

$$
{}_iS^{-1} = \frac{1}{({}_iS_{11}\,{}_iS_{22} - {}_iS_{12}\,{}_iS_{21})}\,(mrad)^{-1} \begin{bmatrix} {}_iS_{22}\,(rad) & -{}_iS_{12}\,(m) \\ -{}_iS_{21}\,(rad) & {}_iS_{11}\,(m) \end{bmatrix} \tag{B.6}
$$

$$
= \begin{bmatrix} \frac{{}_iS_{22}}{{}_iS_{11}\,{}_iS_{22} - {}_iS_{12}\,{}_iS_{21}}\,(m^{-1}) & -\frac{{}_iS_{12}}{{}_iS_{11}\,{}_iS_{22} - {}_iS_{12}\,{}_iS_{21}}\,(rad^{-1}) \\ -\frac{{}_iS_{21}}{{}_iS_{11}\,{}_iS_{22} - {}_iS_{12}\,{}_iS_{21}}\,(m^{-1}) & \frac{{}_iS_{11}}{{}_iS_{11}\,{}_iS_{22} - {}_iS_{12}\,{}_iS_{21}}\,(rad^{-1}) \end{bmatrix} \tag{B.7}
$$

The resulting i^{th} measured deflection error vector is then given by

$$
{}_iS^{-1}\,{}^{Du}\mathcal{E}^i_{\Delta X_M} =
$$

$$
\begin{bmatrix} \frac{{}_iS_{22}}{{}_iS_{11}\,{}_iS_{22} - {}_iS_{12}\,{}_iS_{21}}\,(m^{-1}) & -\frac{{}_iS_{12}}{{}_iS_{11}\,{}_iS_{22} - {}_iS_{12}\,{}_iS_{21}}\,(rad^{-1}) \\ -\frac{{}_iS_{21}}{{}_iS_{11}\,{}_iS_{22} - {}_iS_{12}\,{}_iS_{21}}\,(m^{-1}) & \frac{{}_iS_{11}}{{}_iS_{11}\,{}_iS_{22} - {}_iS_{12}\,{}_iS_{21}}\,(rad^{-1}) \end{bmatrix} \begin{bmatrix} {}^{Du}\mathcal{E}^{i,1}_{\Delta X_M}\,(m) \\ {}^{Du}\mathcal{E}^{i,2}_{\Delta X_M}\,(rad) \end{bmatrix} \tag{B.8}
$$

${}^{Du}\mathcal{E}^{i,j}_{\Delta X_M}$ is the j^{th} element of ${}^{Du}\mathcal{E}^i_{\Delta X_M}$. As can be seen from equation B.8, ${}_iS^{-1}\,{}^{Du}\mathcal{E}^i_{\Delta X_M}$ is dimensionless. Consequently, $G_C\,{}^{Du}\mathcal{E}_{\Delta X_M}$ is also dimensionless. This can be seen in equation B.9.

$$
G_C\,{}^{Du}\mathcal{E}_{\Delta X_M} = \begin{bmatrix} {}_1S^{-1} & & 0 \\ & {}_2S^{-1} & \\ 0 & & \ddots \end{bmatrix} \begin{bmatrix} {}^{Du}\mathcal{E}^1_{\Delta X_M} \\ {}^{Du}\mathcal{E}^2_{\Delta X_M} \\ \vdots \end{bmatrix} = \begin{bmatrix} {}_1S^{-1}\,{}^{Du}\mathcal{E}^1_{\Delta X_M} \\ {}_2S^{-1}\,{}^{Du}\mathcal{E}^2_{\Delta X_M} \\ \vdots \end{bmatrix} \tag{B.9}
$$

APPENDIX

C

An example application requiring high positioning performance along selected axes of the robot's platform

Figure C.1 shows a 6-DOF hexapod developed by Symétrie [Symétrie, a] for positioning a mirror with high accuracy along its five axes. High accuracy was desired only along the three translations (Tx, Ty and Tz) and two rotations (Rx and Ry) of the platform. The mirror had to be positioned in order to integrate it on a satellite. Payload capacity of 250 kg was required. Furthermore, micrometer-level accuracy was needed along the mentioned high performance axes.

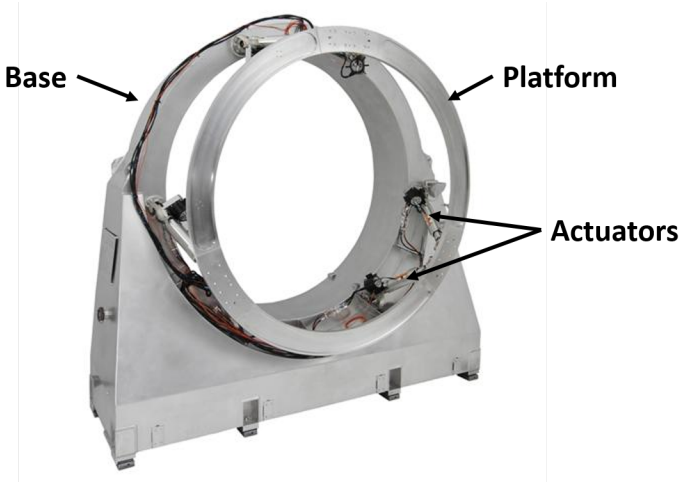

Figure C.1: Hexapod used for positioning a mirror with high accuracy along 5 axes (Tx, Ty, Tz, Rx and Ry) [Symétrie, a]

APPENDIX

D

Simulation study to assess the influence of error in applied force/moment during stiffness identification on compensation accuracy for a hexapod positioning system

Here, a simulation study is presented which was performed to assess the influence of error in applied force/moment during stiffness identification on compensation accuracy, for a high-precision hexapod positioning system. Section D.1 presents the details of this simulation study and section D.2 presents the results of this study.

D.1 Simulation description

This simulation study consists of a Monte-Carlo simulation in which elastostatic calibrations of a high-precision hexapod positioning system (shown in figure D.1) was simulated many times. These simulated elastostatic calibrations were assumed to be influenced by realistic errors in applied forces/moments during stiffness identification. The deflection measurement errors were assumed to be negligible in these simulations. These

elastostatic calibrations were simulated 10,000 times. Tx, Ty and Tz denote the translational coordinates of this hexapod's platform and this hexapod possesses a repeatability of 0.5 µm along these coordinates. Rx, Ry and Rz denote the rotational coordinates of this hexapod's platform and this hexapod possesses a repeatability of 2.5 µrad along these coordinates. These simulated realistic stiffness identification experiments are performed at the zero pose of the hexapod. Also, the desired pose to reach was the zero pose in the simulated positioning experiments. The load was assumed to be applied by placing a mass of 120 kg on the platform of this hexapod (as in figure D.1). This is similar to the manner in which stiffness identification is performed in the experimental study performed in chapter 4. The error in applied force/moment during identification experiments is due to the difference between the assumed position of the center of mass (CoM) and its real value. Realistic value of CoM position errors are assumed. These CoM position errors are assumed: (a) to be distributed normally (Gaussian distribution), and (b) to have maximum values of approximately 3mm along X-, Y- and Z-coordinates (99.7 % confidence interval). Also, the pose measurement system is assumed to be perfect, i.e., deflection measurement errors are assumed to be zero. The resulting compensation errors are, therefore, a consequence of the errors in applied forces/moments (during stiffness identification) only.

Figure D.2 shows the flowchart of the Monte-Carlo simulation performed. Firstly, 10,000 samples of errors in CoM position were generated. These CoM position errors had standard deviations of 1 mm and mean of 0 mm, along each coordinate (X, Y and Z). Using each sample of CoM position error, the resultant 6-DOF measured deflection was calculated. This calculation was done by using a stiffness model of the hexapod like the used in chapter 4. Realistic values were used as the actual stiffness parameters (10 N/µm for virtual spring in each leg). Stiffness parameters were then estimated using the said stiffness model and the simulated measured deflections (with errors due to applied force/moment errors). Subsequently, command pose [1] was generated such that the platform reaches the desired target pose (zero pose). The pose attained after compensation using estimated stiffness parameters was then computed and subsequently, the difference between the at-

1. *Command pose* is the pose entered in the control interface of a robot's controller that doesn't have the compliance error model embedded in it. When the robot's platform is commanded to reach this *command pose*, the robot's platform reaches (close to) the desired target pose due to the platform's deflection under the given load.

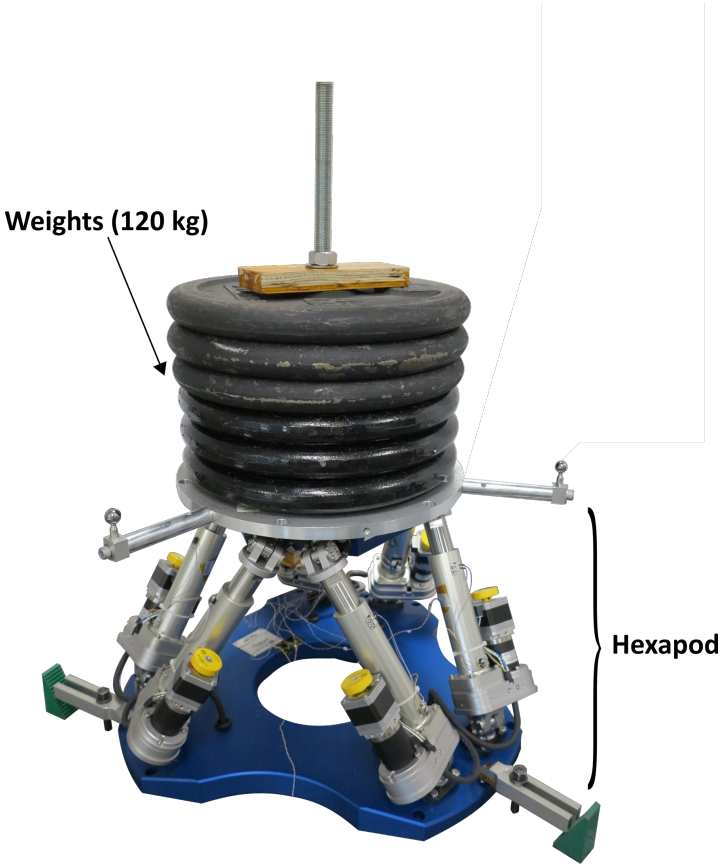

Figure D.1: Hexapod positioning system with 120 kg mass mounted on the platform

tained and the target poses was computed for this trial. After 10,000 trials of this simulation, the 10,000 samples of compensation errors were analysed to study their statistical properties. Section D.2 shows these results.

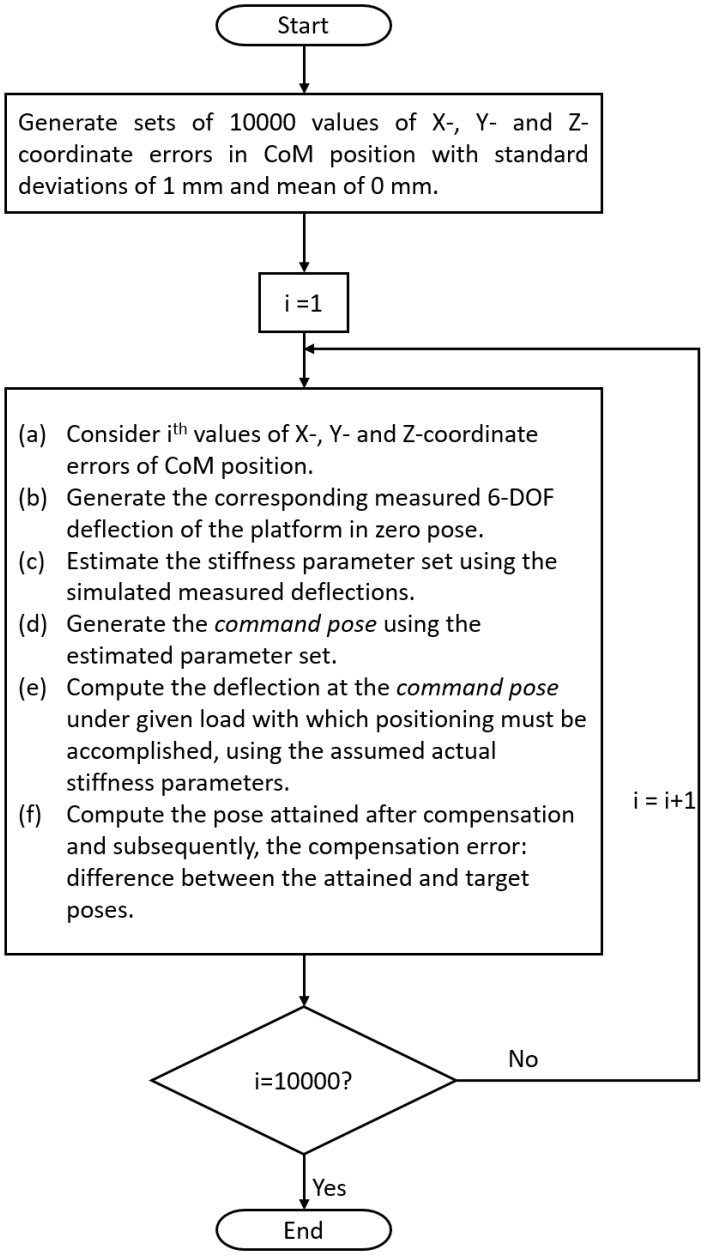

Figure D.2: Flowchart of Monte-Carlo simulations to assess the influence of error in applied force/moment during stiffness identification on compensation accuracy, for a hexapod positioning system

D.2 Results

Figure D.3 shows the probability density functions of the CoM position errors which are the input errors in the Monte-Carlo simulation. Figure D.4 shows the probability density functions of the resultant output, the compensation errors. The dotted lines in these figures show the corresponding 99.7% confidence intervals. As can be seen from the output probability functions, the 99.7% confidence interval boundaries of compensation errors along Rx and Ry axes are considerably more than the repeatability of this hexapod along the respective axes (2.5 µrad). Since, the goal is to reach the level of repeatability of the hexapod, these compensation errors are unacceptable. Hence, it can be seen in this example that the influence of errors in applied forces/moments during stiffness identification on compensation accuracy is indeed not negligible in a realistic case.

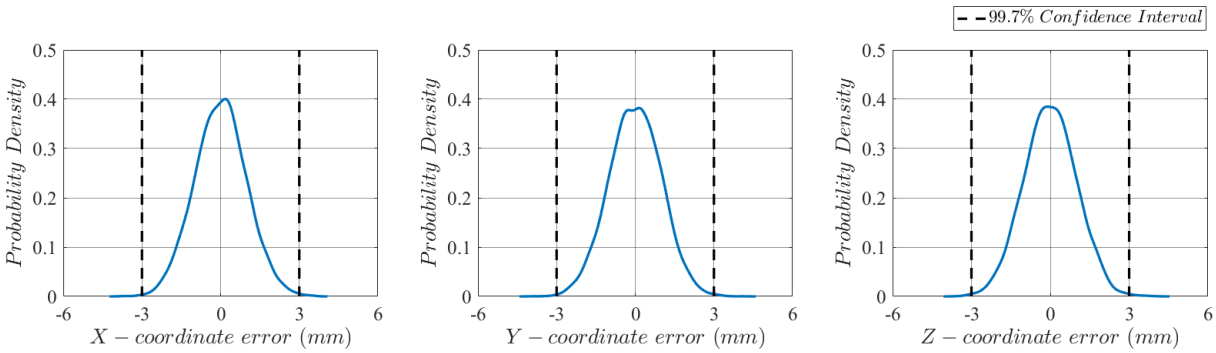

Figure D.3: Probability density functions of the input errors (CoM position errors)

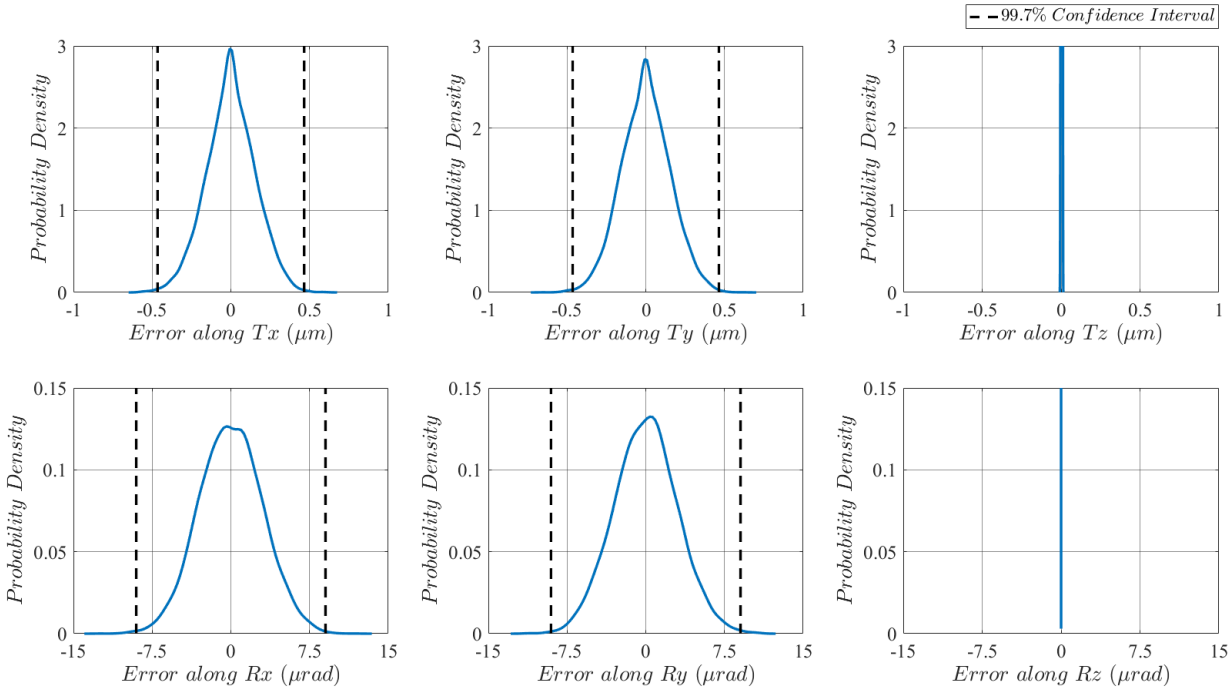

Figure D.4: Probability density functions of the output errors (compensation errors)

APPENDIX

E

Relation between $Cov(\,{}^{Du,t}\mathcal{E}_{X_A})$ and the RMS value of possible Euclidean norms of ${}^{Du,t}\mathcal{E}_{X_A}$

Here, the derivation of relationship between $Cov(\,{}^{Du,t}\mathcal{E}_{X_A})$ and the RMS value of possible Euclidean norms of ${}^{Du,t}\mathcal{E}_{X_A}$ is shown.

Firstly, using equation 2.27, the following can be written:

$$
\begin{aligned}
{}^{Du,t}\mathcal{E}_{X_A} &\approx -\,{}^{Du,t}\mathcal{E}_{\Delta X_C} && \text{(E.1)}\\
&\approx -\,{}^{t}A_C\,{}^{Du}\mathcal{E}_c && \text{(E.2)}\\
&\approx -\,{}^{t}A_D\,{}^{Du}\mathcal{E}_c && \text{(E.3)}
\end{aligned}
$$

In equation E.1, superscript t indicates that they are the translational components (or elements corresponding to translational components) of the respective array/matrix corresponding to them [1]. The following can then be written:

$$
E\left({}^{Du,t}\mathcal{E}_{X_A}{}^{T}\,{}^{Du,t}\mathcal{E}_{X_A}\right) = {}^{Du}\rho^2 = E\left(\left(-\,{}^{t}A_D\,{}^{Du}\mathcal{E}_c\right)^{T}\left(-\,{}^{t}A_D\,{}^{Du}\mathcal{E}_c\right)\right) \qquad \text{(E.4)}
$$

1. ${}^{Du,t}\mathcal{E}_{\Delta X_C}$ contains the translational components of ${}^{Du}\mathcal{E}_{\Delta X_C}$.

Here, $E(\mathfrak{e})$ denotes expectation of $\mathfrak{e}$. In equation E.4, ${}^{Du}\rho$ is the RMS value of possible Euclidean norms of translational components of ${}^{Du}\mathcal{E}_{X_A}$. This equation can be further expanded to get

$$\begin{aligned} {}^{Du}\rho^2 &= tr\Big(E\big((-{}^{t}A_D\,{}^{Du}\mathcal{E}_c)(-{}^{t}A_D\,{}^{Du}\mathcal{E}_c)^T\big)\Big) \\ &= tr\Big(E\Big({}^{t}A_D\,{}^{Du}\mathcal{E}_c\,{}^{Du}\mathcal{E}_c^T\,{}^{t}A_D{}^T\Big)\Big) \\ &= tr\Big({}^{t}A_D\,E\Big({}^{Du}\mathcal{E}_c\,{}^{Du}\mathcal{E}_c^T\Big)\,{}^{t}A_D{}^T\Big) \end{aligned} \tag{E.5}$$

Here, $tr(\mathfrak{W})$ denotes trace of matrix $\mathfrak{W}$. However, $E\Big({}^{Du}\mathcal{E}_c\,{}^{Du}\mathcal{E}_c^T\Big) = Cov({}^{Du}\mathcal{E}_c)$. Therefore, using equations 2.13 and E.5, the following can be written:

$${}^{Du}\rho^2 = ({}^{Du}\sigma_{\widetilde{\mathcal{E}}_{\Delta X_M}})^2 \overbrace{tr\Big({}^{t}A_D\,H\,({}^{as}\widetilde{A_M}^T\,{}^{as}\widetilde{A_M})^{-1}\,H^T\,{}^{t}A_D{}^T\Big)}^{{}^{Du}\Omega} \tag{E.6}$$

Comparing equations E.6 and 2.31, the following relationship can be obtained:

$${}^{Du}\rho^2 = tr\Big(Cov({}^{Du,t}\mathcal{E}_{X_A})\Big) \tag{E.7}$$

Equation E.7 describes the relationship between $Cov({}^{Du,t}\mathcal{E}_{X_A})$ and the RMS value of possible Euclidean norms of ${}^{Du,t}\mathcal{E}_{X_A}$, ${}^{Du}\rho$.

APPENDIX

F

Relation between $Cov({}^{FE,t}\varepsilon_{X_A})$ and the RMS value of possible Euclidean norms of ${}^{FE,t}\varepsilon_{X_A}$

Here, the derivation of relation between $Cov({}^{FE,t}\varepsilon_{X_A})$ and the RMS value of possible Euclidean norms of ${}^{FE,t}\varepsilon_{X_A}$ is shown.

Equation 2.54 can be used to get the following expression:

$$E\left({}^{FE,t}\varepsilon_{X_A}{}^{T}\,{}^{FE,t}\varepsilon_{X_A}\right) = {}^{FE}\rho^2 = E\left(({}^{t}Z\,\varepsilon_{\Delta F_M})^T({}^{t}Z\,\varepsilon_{\Delta F_M})\right) \tag{F.1}$$

Here, $E(\mathfrak{e})$ denotes expectation of $\mathfrak{e}$. In equation F.1, ${}^{FE}\rho$ is the RMS value of possible Euclidean norms of translational components of ${}^{FE}\varepsilon_{X_A}$, ${}^{FE,t}\varepsilon_{X_A}$. Equation F.1 can be further expanded to get

$$\begin{aligned} {}^{FE}\rho^2 &= tr\left(E\left(({}^{t}Z\,\varepsilon_{\Delta F_M})({}^{t}Z\,\varepsilon_{\Delta F_M})^{T}\right)\right) \\ &= tr\left(E\left({}^{t}Z\,\varepsilon_{\Delta F_M}\,\varepsilon_{\Delta F_M}{}^{T}\,{}^{t}Z^{T}\right)\right) \\ &= tr\left({}^{t}Z\,E(\varepsilon_{\Delta F_M}\,\varepsilon_{\Delta F_M}{}^{T})\,{}^{t}Z^{T}\right) \end{aligned} \tag{F.2}$$

Here, $\mathrm{tr}(\mathfrak{W})$ denotes trace of matrix $\mathfrak{W}$. However, $\mathrm{E}(\mathcal{E}_{\Delta F_M}\ \mathcal{E}_{\Delta F_M}{}^{\mathsf{T}}) = \mathrm{Cov}(\mathcal{E}_{\Delta F_M})$. Consequently, equation F.2 can be written as

$$^{\mathrm{FE}}\rho^2 = \mathrm{tr}\Big(\ ^{\mathrm{t}}Z\ \mathrm{Cov}(\mathcal{E}_{\Delta F_M})\ ^{\mathrm{t}}Z^{\mathsf{T}}\Big) \tag{F.3}$$

Finally equations 2.56 and F.3 give the following expression:

$$^{\mathrm{FE}}\rho^2 = \mathrm{tr}\Big(\mathrm{Cov}(\ ^{\mathrm{FE,t}}\mathcal{E}_{X_A})\Big) \tag{F.4}$$

Equation F.4 describes the relationship between $\mathrm{Cov}(\ ^{\mathrm{FE,t}}\mathcal{E}_{X_A})$ and the RMS value of possible Euclidean norms of $^{\mathrm{FE,t}}\mathcal{E}_{X_A}$, $^{\mathrm{FE}}\rho$.

APPENDIX

G

Preliminary results of stiffness identification of a hexapod using the stiffness model presented in chapter 4

Here, the details and results of a preliminary study performed to validate the efficacy of stiffness model for hexapods, presented in section 4.2 of chapter 4, is presented. In this study, stiffness identification of a hexapod was performed using the said stiffness model. Following this, the estimated stiffness parameters of this stiffness model were used to predict the deflections of the loaded hexapod. These predictions were compared with the measured deflections to study the efficacy of this stiffness model and the estimated parameters. This study was performed on another high-precision positioning hexapod [1] from Symétrie and this is shown in figures G.1 and G.2. The setup available for performing pose measurements and for applying force/moment on the platform were same as described in section 4.1 of chapter 4.

Section G.1 presents the details and results of stiffness identification performed on this hexapod. This is followed by details and results of the study performed to validate the efficacy of the stiffness model and its estimated parameters in section G.2.

1. Different from the one used for experimental study in chapter 4.

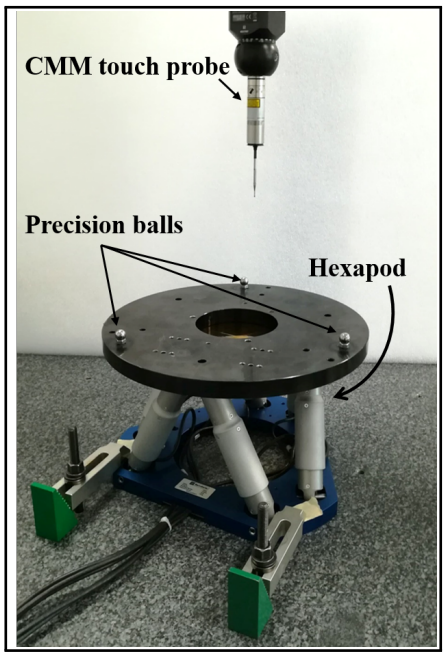

Figure G.1: Hexapod (without mass mounted on the platform) along with the pose measurement apparatus, used in this study

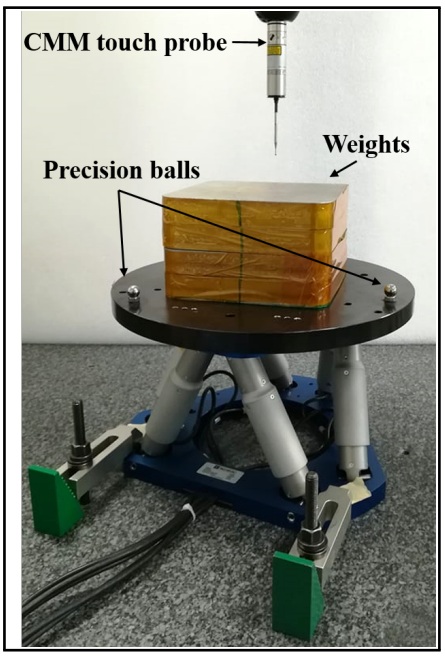

Figure G.2: Hexapod (with mass mounted on the platform) along with the pose measurement apparatus, used in this study

G.1 Stiffness identification

Figure G.3 shows the kinematic scheme and the stiffness model of the SPS (spherical-prismatic-spherical) hexapod used for this study. Note that this stiffness model is the same as the one shown in section 4.2 of chapter 4. Consequently, the equations pertaining to stiffness modelling of this hexapod are also same (as in section 4.2) in this case.

Before performing loading experiments for stiffness identification, practical constraints needed to be taken into account. This constraint was a result of the loading setup available. This loading setup consisted of weights that could be placed on the platform of the hexapod (see figure G.2). This setup demanded the platform to not be rotated about its X and Y axes. This constraint was incorporated to make sure that the mounted mass does not slide off of the platform. Furthermore, using this setup for loading also came with the constraint that the force could only be applied along the Z axis of the platform.

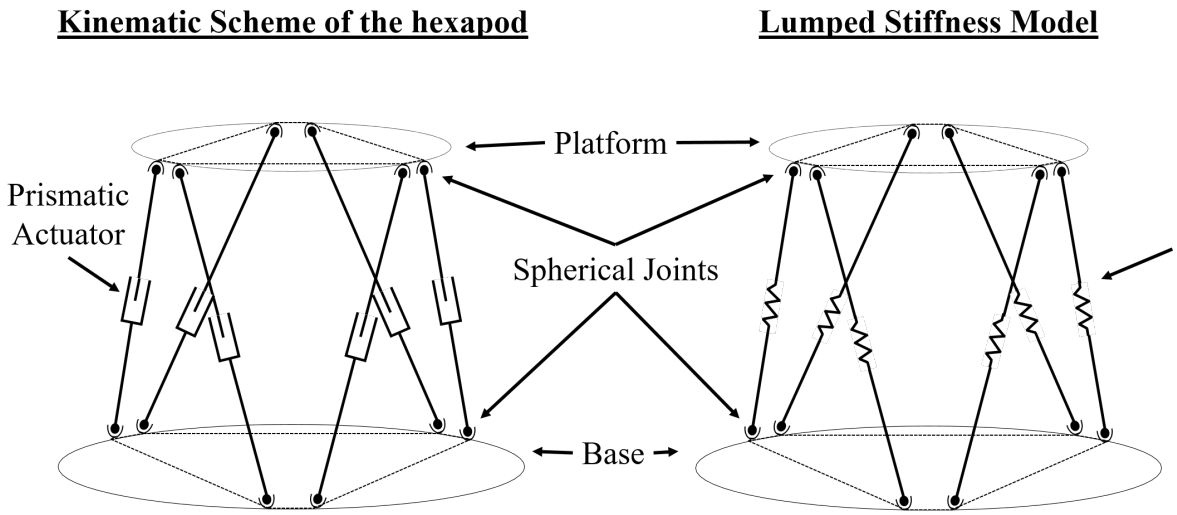

Figure G.3: Kinematic scheme and the lumped stiffness model of the hexapod under study

The number of poses and number of deflection measurements per pose also had to be chosen. High number of measurements leads to better accuracy of identified parameters but time limits the number of measurements. Hence, compromising between time-efficiency and accuracy, three poses and three measurements per pose were chosen. Furthermore, it is also assumed that the legs of the hexapod exhibit linear stiffness behavior. Consequently, just one load vector should be enough to identify the stiffness in each leg. Figure G.4 shows the the results of an experiment that shows the hexapod's linear stiffness behavior. Also, it is best to apply maximum possible force/moment for better identifiability of parameters [2]. Due to the above reasons, choice was made to use just one load vector of maximum possible magnitude. This was 34.5 kg in the given case. Also, it was necessary to place an initial load of 12.2 kg on the platform to suppress the play in actuators. Hence, the effective force using which the platform deflection was to be measured was 22.3 kg along the Z-axis of the platform.

Considering the choices listed above, it was necessary to choose three poses at which stiffness identification had to be performed. Since the goal here was only to validate the stiffness model, these three identification poses were chosen arbitrarily. The chosen iden-

2. More force/moment leads to more deflection of the platform and this is good for identifiability of parameters. This is because the errors in deflection measurements have less impact on the identified parameters when the magnitude of platform deflections are high.

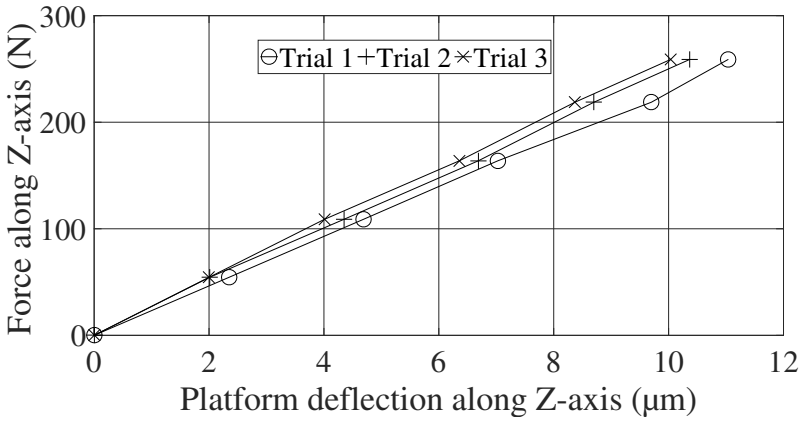

Figure G.4: Plot showing the deflection of the hexapod's platform along its Z-axis when a series of pure forces along its Z-axis were applied

tification poses respected the workspace constraints due to joint & actuator limits of the hexapod. Additionally, these poses didn't have rotations about X and Y axes to prevent the mounted load from sliding off of the platform. The hexapod's platform was loaded in these poses and the platform deflections were measured [3]. Least squares estimation, as outlined in chapter 2, was employed to get the stiffness parameters which are tabulated in table G.1.

Table G.1: Estimated stiffness parameters

Stiffness parameter value $(N/\mu m)$					
k_1	k_2	k_3	k_4	k_5	k_6
4.1981	3.7898	2.7503	4.3200	3.6716	3.7288

G.2 Validation of stiffness model efficacy

To validate the efficacy of the stiffness model and the estimated parameters, platform deflection measurements were performed at different poses along the X and Y axes of the hexapod's platform. The poses at which these pose measurements were performed are

3. Pose measurement method presented in appendix A was used in this case.

listed in table G.2. The load applied during these deflection measurements was same as the one used for for stiffness identification.

Table G.2: Poses used for experimental validation

Pose along	Pose parameters					
	Tx(mm)	Ty(mm)	Tz(mm)	Rx(deg)	Ry(deg)	Rz(deg)
X-axis	-30	0	0	0	0	0
	-15					
	0					
	15					
	30					
Y-axis	0	-30	0	0	0	0
		-15				
		0				
		15				
		30				

Figures G.5 and G.6 show the comparison between the predicted and measured 6-DOF deflections of the platform at different poses along the X and Y axes of the hexapod, respectively. Table G.3 shows the RMS values of errors in prediction of these 6-DOF deflections. These results show that the predicted and measured deflections of the platform are very close. As seen in table G.3, the RMS values of prediction errors are under 3.1 μm for translational deflections and 8.8 μrad for rotational deflections. Therefore, it can be concluded that the stiffness model and its estimated parameters are effective in predicting the deflections of the loaded hexapod.

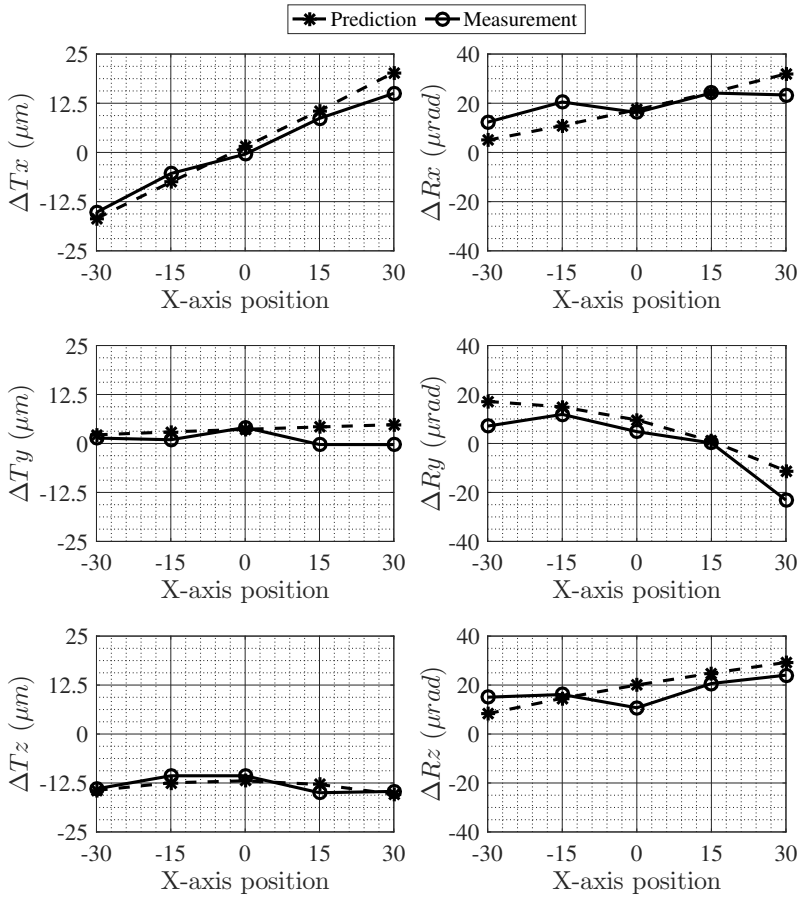

Figure G.5: Plot of predicted and measured 6-DOF deflections of the loaded hexapod at poses along X-axis

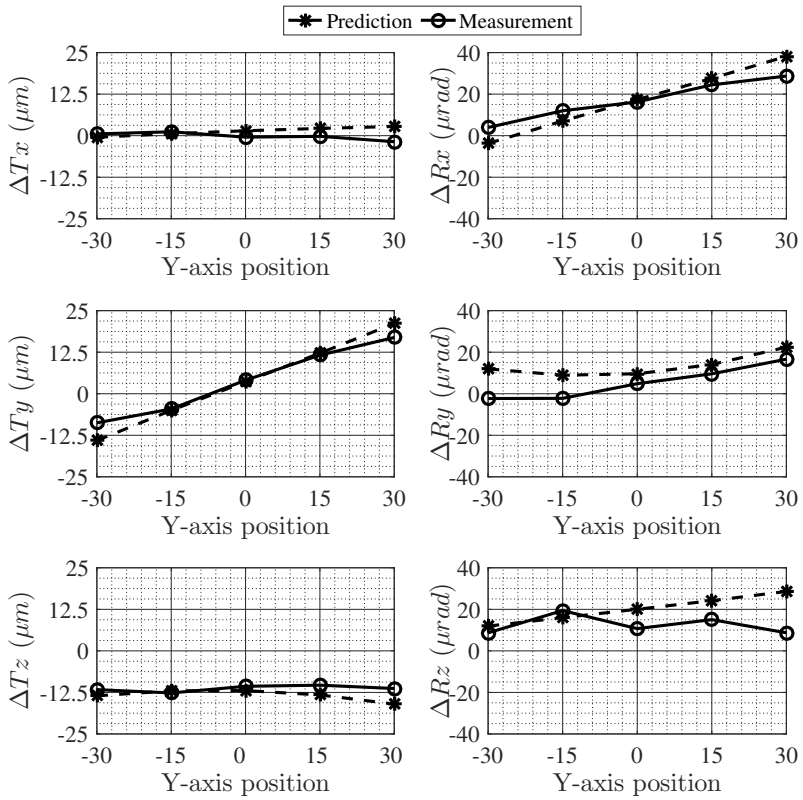

Figure G.6: Plot of predicted and measured 6-DOF deflections of the loaded hexapod at poses along Y-axis

Table G.3: Error in deflection prediction (RMS values)

$\epsilon_{\Delta Tx}$	2.7 µm
$\epsilon_{\Delta Ty}$	3.1 µm
$\epsilon_{\Delta Tz}$	2.2 µm
$\epsilon_{\Delta Rx}$	6.4 µrad
$\epsilon_{\Delta Ry}$	8.3 µrad
$\epsilon_{\Delta Rz}$	8.8 µrad

APPENDIX

H Thermal defection decoupled 6-DOF pose measurement method for hexapods

The method presented in appendix A for 6-DOF pose measurement of hexapods is susceptible to thermal deflections of the hexapod. In this appendix, a new method is presented which is not susceptible to thermal deflections of the hexapod. Section H.1 presents a deeper understanding of the aforementioned problem with the conventional pose measurement method (like the one on appendix A). Section H.2 presents the thermal deflection decoupled pose measurement method. This is followed by details and results of an experimental study performed to validate the presented method in section H.3.

H.1 Conventional pose measurement method and its drawback

Pose measurements are always performed by measuring points using a measurement system which has a coordinate frame (M) attached to it. All the points are measured with respect to this coordinate frame. The requirement in 6-DOF pose measurement of a hexapods is to measure the coordinate frame fixed to the platform (platform frame), S_i, when the hexapod is in any i^{th} arbitrary configuration with respect to another coordinate

frame O. For the case of hexapods studied in this paper, coordinate frame O is the platform frame when the hexapod's platform is in zero pose [1].

The conventional method to measure the 6-DOF pose of the platform frame of an arbitrary pose S_1 with respect to frame O is illustrated in figure H.1. The frame O is measured [2] with respect to M first. This coordinate frame is measured with the legs having a temperature set $t_1 = [t_{11}, t_{12}, .., t_{16}]$, where t_{1i} is the temperature of the i^{th} leg during this measurement. Let this measured frame be called O^{t_1}. The platform is then commanded to the arbitrary pose at which the pose measurement needs to be performed. The transformation (translation and rotation) between the frame O^{t_1} and the platform frame S_1 is then measured as described in appendix A. However, this measurement happens with the legs having a temperature set $t_2 = [t_{21}, t_{22}, .., t_{26}]$. Let the coordinate frame with the legs have temperature set t_2 be called $S_1^{t_2}$. Therefore, the actual transformation measured is the one between O^{t_1} and $S_1^{t_2}$, written as $T_{O^{t_1}}^{S_1^{t_2}}$. Let the corresponding measured pose be denoted as $X_{S_1^{t_2}}^{O^{t_1}}$.

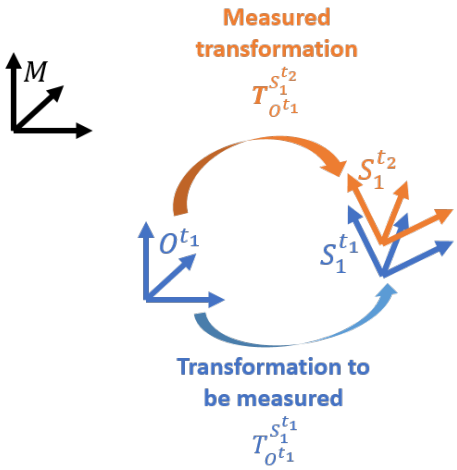

Figure H.1: Illustration of the conventional pose measurement method to measure the pose of an arbitrary coordinate frame S_1 with respect to a coordinate frame O

1. This is the pose of the platform in which all the pose parameters are zero. In this pose, all the legs have the same length.

2. O is measured with respect to M by measuring different points on the platform of the hexapod. Check appendix A for more description where a similar measurement is described.

From the description presented above, it can be easily seen that the measured transformation would have been different if the legs of the hexapod would have had the temperature set t_1. The platform frame in this case ($S_1^{t_1}$) would have a different pose vector $X_{S_1^{t_1}}^{O^{t_1}}$. This is due to the thermal deflection of the legs of the hexapod with the change in their temperatures from set t_1 to set t_2. Temperature change also affects other dimensions of the hexapod. However, for most hexapods, the thermal deflection of legs is much higher than that of the other parts because: (a) the legs generally have larger dimensions (length) as compared to the other parts, and (b) driving motors are mounted on/near the legs which heat the legs more than the other parts.

To understand the drawback of this measurement method, consider a case in which pose measurements need to be performed for a long duration of time[3]. When conventional pose measurement is used in this case, different platform poses will be measured with legs at different temperatures. This can happen due to heating supplied by motors or the surrounding air. Consequently, different measured poses have the influence of different magnitudes of thermal deflections of legs. This can be problematic, for example, in the case of pose measurements performed in the experimental studies in sections 4.3.2 and 4.4.2. In these cases, the accuracy of positioning of the unloaded robot and the loaded robot with error compensation are compared to evaluate the efficiency of compensation. These two measurements are made with legs possibly at different temperatures. The thermal deflections in the legs due to the aforementioned temperature difference can cause considerable thermal deflections, thereby making it difficult to evaluate the efficiency of compensation. Therefore, a new pose measurement method is necessary that is insusceptible to thermal deflections of the hexapod.

H.2 Thermal deflection decoupled pose measurement method

Figure H.2 illustrates the proposed method to measure the 6-DOF pose of the platform frame with the platform at an arbitrary pose S_1, with respect to frame O. In this method,

3. Like in pose measurements needed in validation studies described in sections 4.3.2 and 4.4.2

frame O^{t_1} must be measured first (with the legs having temperature set t_1). Immediately after this, the platform must be moved to a reference pose R. The transformation between the platform frame R and O^{t_1} must be measured quickly such that the measurement happens with the legs having the temperature set t_1. Let this measured frame be called R^{t_1}. The platform can then be moved to any arbitrary pose (frame S_1). The transformation between this frame and O^{t_1} can be measured with the legs having a temperature set t_2. This measured frame is $S_1^{t_2}$. An additional measurement, transformation between frames R and O^{t_1}, must be performed quickly before/after measuring $S_1^{t_2}$. This measurement must be performed with the hexapod's legs having the temperature set t_2 (measured coordinate frame: R^{t_2}).

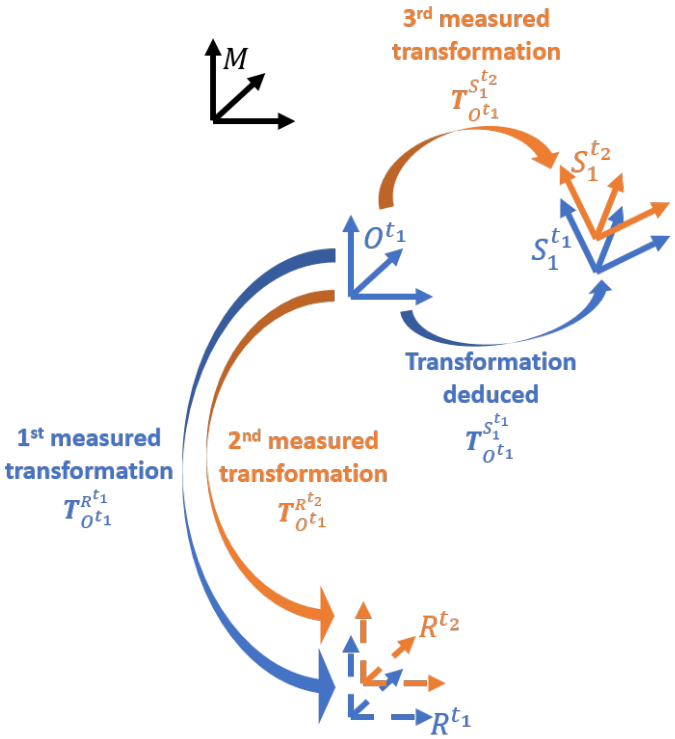

Figure H.2: Illustration of the thermal deflection decoupled pose measurement method to measure the pose of an arbitrary coordinate frame S_1 with respect to a coordinate frame O

Figure H.3 illustrates the method to obtain the necessary pose vector $X_{S_1^{t_1}}^{O^{t_1}}$ using the measurement data obtained from the measurements outlined above. The measurement procedure described can be used to obtain three transformations: $T_{O^{t_1}}^{R^{t_1}}$, $T_{O^{t_1}}^{R^{t_2}}$ and $T_{O^{t_1}}^{S_1^{t_2}}$.

Consequently, the corresponding 6-DOF pose vectors, $X_{R^{t_1}}^{O^{t_1}}$, $X_{R^{t_2}}^{O^{t_1}}$ and $X_{S_1^{t_2}}^{O^{t_1}}$ can be obtained. These pose vectors can be used to get the corresponding leg lengths of the hexapod by using the inverse geometric model (*IGM*) of the hexapod. $q_{R^{t_1}}$, $q_{R^{t_2}}$ and $q_{S_1^{t_2}}$ are the arrays containing the leg lengths of the hexapod corresponding to pose vectors $X_{R^{t_1}}^{O^{t_1}}$, $X_{R^{t_2}}^{O^{t_1}}$ and $X_{S_1^{t_2}}^{O^{t_1}}$, respectively. $q_{R^{t_1}}$ and $q_{R^{t_2}}$ can then be used to compute the thermal deflection the hexapod's legs corresponding to temperature change from set t_1 to set t_2, with the platform at reference pose R. Let the array containing these leg deflections be called $\Delta q_{R^{t_1}-R^{t_2}}$ and let $\Delta q^i_{R^{t_1}-R^{t_2}}$ be the deflection of the i^{th} leg. The thermal deflection due to temperature change of legs from set t_1 to set t_2 of the i^{th} leg of the hexapod at the arbitrary pose S_1, $\Delta q^i_{S_1^{t_1}-S_1^{t_2}}$, can then be estimated easily. The task here is to find the thermal deflection of the legs with lengths $q_{S_1{}^{t_2}}$, when the temperature of these legs change from set t_1 to set t_2, when the thermal deflection of the same legs with lengths $q_{R^{t_1}}$ are known. The method to perform this computation must respect the dimensions and material properties of the components of the leg assembly. $\Delta q_{S_1^{t_1}-S_1^{t_2}}$ can then be subtracted from $q_{S_1{}^{t_2}}$ to obtain $q_{S_1{}^{t_1}}$. $q_{S_1{}^{t_1}}$ is the array containing the leg lengths when the platform is at the arbitrary pose S_1 and the legs have temperature set t_1. Finally, the necessary pose vector $X_{S_1^{t_1}}^{O^{t_1}}$ can be obtained by using forward geometric model (*FGM*) of the hexapod corresponding to $q_{S_1{}^{t_1}}$. When multiple platform poses shall be measured using this method while leg temperatures change, the measured poses will not have the influence of different magnitudes of thermal deflections of legs. Hence, the drawback of the conventional method can be overcome using this method.

H.3 Experimental validation of the proposed pose measurement method

This section presents the details of an experimental study performed to compare the conventional and proposed methods for 6-DOF pose measurement of hexapods. The legs of the hexapod were heated during this experiment to control and slightly exaggerate heating in legs.This was done to clearly show the advantage of the proposed pose measurement method over the conventional method. Figure H.4 shows the test setup used for this exper-

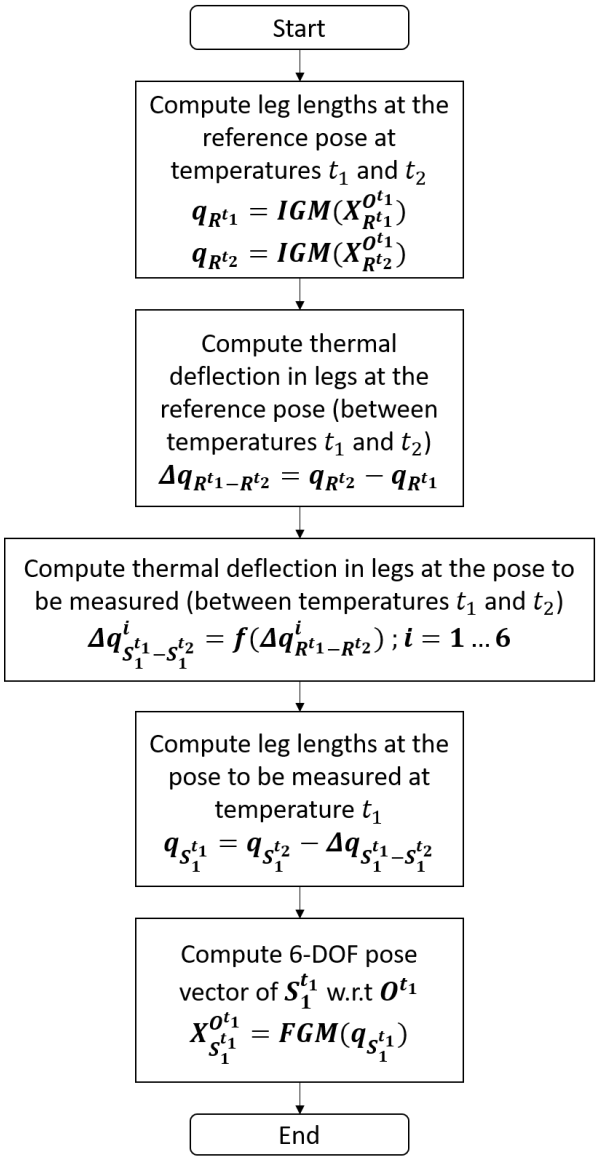

Figure H.3: Flowchart of procedure to post-process the measured data to obtain the required pose vector in the thermal deflection decoupled pose measurement method

imental study. The hexapod used in this study is the same as the one used for experimental studies in chapter 4. A flexible electric heating mat was fixed to each leg to facilitate heating. Thermocouples were used to measure the temperature of each leg and the surrounding air. Precision balls were fixed to the hexapod's platform which were used for measuring the coordinate frame fixed to the platform. The measurements were performed using a LK-

METRIS CMM equipped with a RENISHAW SP25 touch probe. The uncertainty of points measured using this CMM, quantified using the MPE_P value [ISO, 2000], is about $\pm 2\ \mu m$.

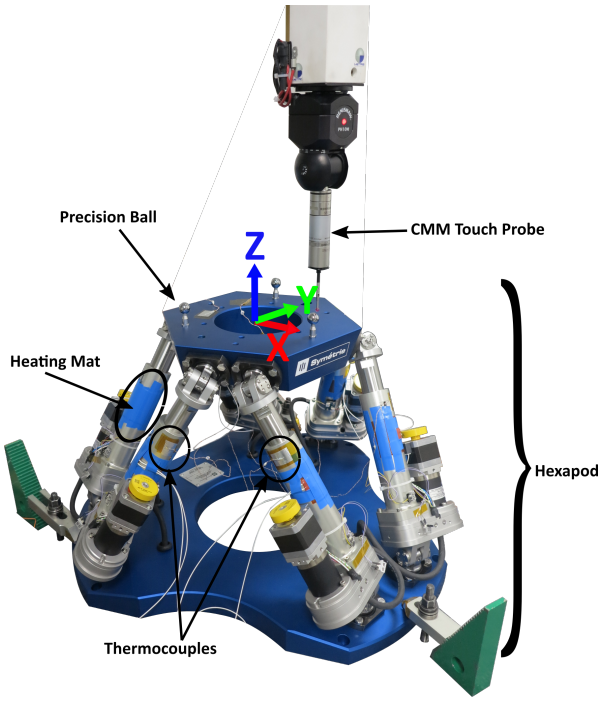

Figure H.4: Test setup

Poses of the platform of the hexapod used in this study are defined by a coordinate frame fixed to the platform at its center. The position and orientation of this platform frame is predefined using holes and planes which are precisely machined on the platform in the manufacturing phase (see sppendix A for more details). The coordinate frame with respect to which any pose of the platform is defined (O) is the platform frame with the hexapod in zero pose configuration [4] (see figure H.5).

In this experimental study, the pose to be measured (refered to as measurement pose from here), called S_1 in sections H.1 and H.2, was the zero pose. This pose was chosen to be measured in order to facilitate the ease of understanding results as the hexapod is symmetrical in this configuration (see figure H.5). The reference pose R to be used in the proposed pose measurement method had the pose vector $[0\ mm\ 0\ mm\ -40\ mm\ 0°\ 0°\ 0°]$. The

4. This is the configuration of the hexapod in which all of the platform pose parameters are zero. In this configuration, all the legs have the same length.

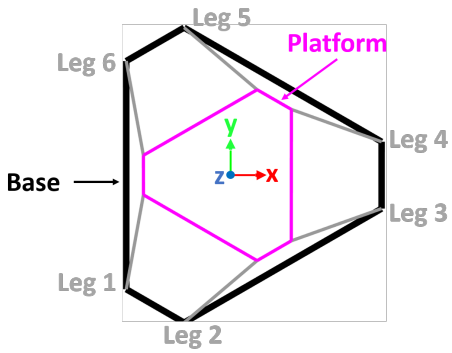

Figure H.5: Hexapod with platform in [0 mm 0 mm 0 mm 0° 0° 0°] pose (top view)

necessary measurements were made to perform the pose measurement as per the thermal deflection decoupled method (see section H.2). Note that (a part of) these measurements can also be used for performing pose measurements as per the conventional method of appendix A. Ten trials of measurements were performed and the hexapod's legs were heated during this using the electric heating mats. The measurements were then post-processed as per the conventional (appendix A) and proposed (section H.2) methods.

In the proposed pose measurement method, the thermal expansion of the legs with the platform in measurement pose had to be predicted. This had to be done using the measured thermal expansions of the legs at the reference pose (see section H.2). The following logic was used for this: the legs of the hexapod used in this study could be divided lengthwise into an Aluminium part of fixed length and a Steel part of variable length. When the platform is moved from one pose to another, the Steel parts of legs change their lengths to achieve the new required lengths. When the thermal expansion of legs at the reference pose were measured, the corresponding thermal expansions of the Aluminium and the Steel parts could be determined. This could be done because the lengths and the thermal expansion coefficients of the two parts were known. The length of each leg and the corresponding length of the Steel part, with the hexapod in the measurement pose, were also known. The thermal expansion of the Steel part of each leg measured in reference pose was then appropriately scaled to estimate the thermal expansion of the Steel part of each leg in measurement pose. The thermal expansion of the Aluminium part was same for the reference and measurement poses as this part does not change its length. The total

thermal expansion of each leg at the measurement pose was then obtained by adding the corresponding thermal expansions of the Steel and Aluminium parts.

Figure H.6 shows the pose parameters of the measurement pose measured by using the conventional and proposed methods. $\mathrm{Tx}_{\mathrm{mes}}$, $\mathrm{Ty}_{\mathrm{mes}}$ and $\mathrm{Tz}_{\mathrm{mes}}$ are the components of measured pose vector corresponding to translations along X, Y and Z axes of the hexapod, respectively. $\mathrm{Rx}_{\mathrm{mes}}$, $\mathrm{Ry}_{\mathrm{mes}}$ and $\mathrm{Rz}_{\mathrm{mes}}$ are the components of measured pose vector corresponding to rotations about X, Y and Z axes of the hexapod, respectively. Figure H.7 shows the temperatures measured at different locations during this test.

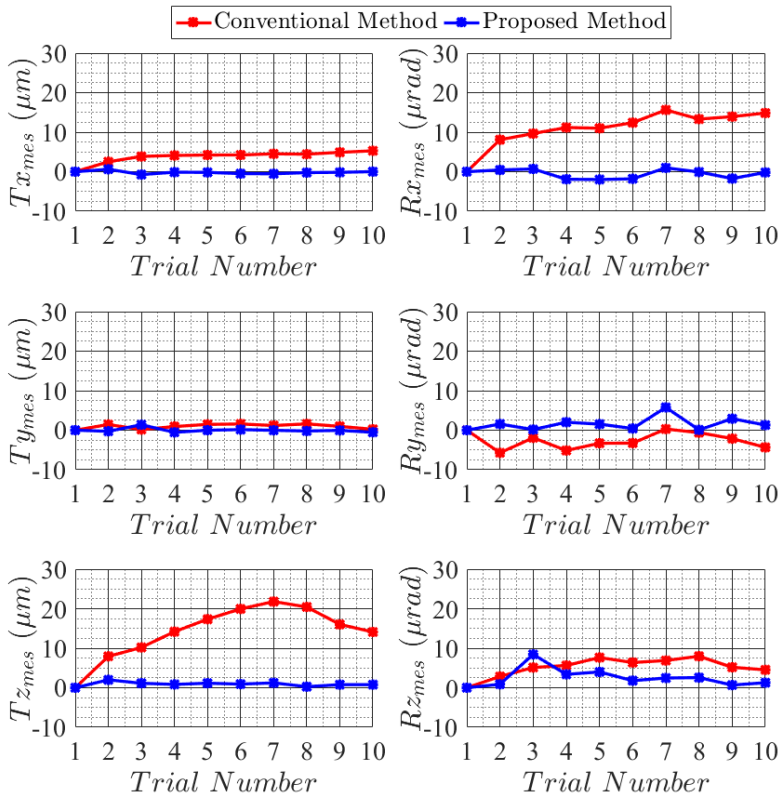

Figure H.6: Measured pose parameters using conventional and thermal deflection decoupled methods with the platform in zero pose

It can be seen in figure H.6 that the measured pose parameters obtained using the conventional method deviates significantly with every trial. These observed deviations can be

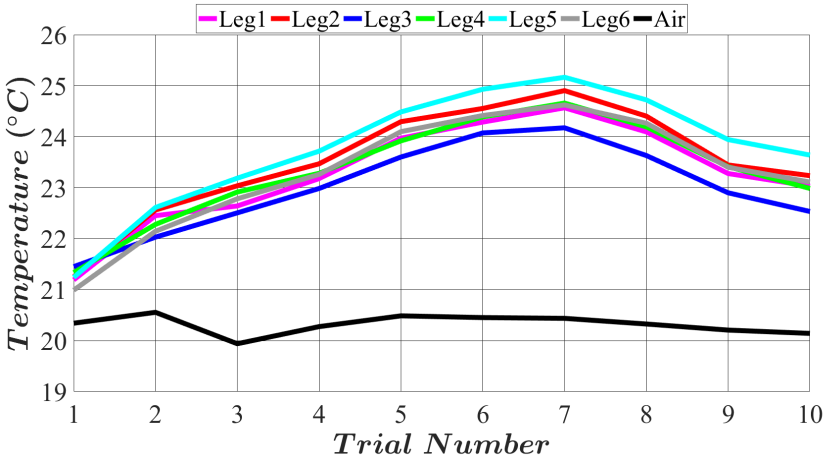

Figure H.7: Measured temperatures

correlated with the change in leg temperatures between trials. The trend of deviation of Tz_{mes} using the conventional method is similar to the trend of the change in temperature of all legs. This behaviour is logical given the orientation of all legs in zero pose. Also, deviation seen in Tx_{mes} using conventional method increases with every consecutive trial until the end. This can be explained by the temperatures measured in legs 2, 3, 4 and 5. The temperatures of legs 2 and 5 are higher than those of legs 3 and 4 during the test and this difference increases with every consecutive trial until the end. Consequently, legs 2 and 5 push the platform more in positive X-direction as compared to legs 3 and 4 pushing it in the opposite direction. Furthermore, deviation seen in Rx_{mes} using conventional method also increases with every consecutive trial until the end. This can be explained by the difference in temperatures of legs 3 and 5 (with leg 5 heating more than leg 3) which follows a similar trend. Consequently, leg 5 pushes the platform more about the X-axis as compared to leg 3 and results in a positive rotational deviation about the X-axis with every consecutive trial. The pose parameters measured using the proposed method do not deviate with change in temperature of hexapod's legs, unlike the ones measured using conventional method. It is, therefore, clear that the proposed method is effective in eliminating the influence of thermal deflection of the hexapod on the measured pose parameters.

APPENDIX

I

Formulating DUIR criterion for optimizing geometric parameter identification in robot geometric calibration

This thesis presented a framework for formulating criteria for choosing the best set of poses and forces/moments for stiffness identification. These formulated criteria minimize the impact of errors influencing stiffness identification [1] on the poses attained after positioning compensation. As was mentioned in section 1.3.2, the parametric calibration framework used for robot elastostatic calibration is similar to the one used for robot geometric calibration. Furthermore, one error source impacts parameter identification in both these robot calibrations: uncertainty of deflection measurements performed. As a result, the framework for formulating criterion for minimizing the influence of this error on elastostatic calibration performance, the DUIR criterion, can also be used for minimizing the influence of this error on the performance of robot geometric calibration. The manner of formulating DUIR criterion for optimizing geometric parameter identification in robot geometric calibration is discussed below.

1. Deflection measurement uncertainty and errors in forces/moments applied during stiffness identification experiment.

Equation 1.17 can be rewritten for the case of geometric calibration as

$$W\,\mathrm{p} = \Delta X \tag{I.1}$$

In equation I.1, A and c from equation 1.17 are replaced by W and p, respectively. W and p are the equivalents of A and c in the case of geometric calibration, respectively. W is a function of actuator positions and the assumed geometric parameter set while p contains the difference between the actual and assumed geometric parameters' values [Sun and Hollerbach, 2008]. ΔX in this case is the difference between the measured and expected poses. Let all variables have the same names in the case of geometric calibration, except for the ones related to A and c (A_M, A_D,.. etc replaced by W_M, W_D,.. etc and $\widehat{c}$, ${}^{Du}\mathcal{E}_c$,...etc replaced by $\widehat{\mathrm{p}}$, ${}^{Du}\mathcal{E}_\mathrm{p}$,...etc).

Equation 2.30, which is used for formulating DUIR criterion in the case of robot elastostatic calibration, can be written for the case of geometric calibration as

$$Cov({}^{Du}\mathcal{E}_{X_A}) \approx ({}^{Du}\sigma_{\widetilde{\mathcal{E}}_{\Delta X_M}})^2 \underbrace{W_D\,H\,({}^{as}\widetilde{W_M}^T\,{}^{as}\widetilde{W_M})^{-1}\,H^T\,W_D^T}_{U_g} \tag{I.2}$$

Here, U_g is a function of poses used for geometric parameter identification. It controls the propagation of uncertainty in measured pose deflections to uncertainty of resultant errors in poses attained after compensation. Equation I.2 can be used in ways similar to the ways described in section 2.3.2 to find best poses for geometric parameter identification.

List of publications

1. **V. J. Kalas**, A. Vissière, T. Roux, O. Company, S. Krut and F. Pierrot, *A new efficient stiffness evaluation method to improve accuracy of hexapods*, Proceedings of ASME IDETC/CIE (2018).
2. **V. J. Kalas**, A. Vissière, O. Company, S. Krut, P. Noire, T. Roux and F. Pierrot, *Thermal deflection decoupled 6-DOF pose measurement of hexapods*, Proceedings of euspen's 20^{th} International Conference & Exhibition (2020).
3. **V. J. Kalas**, A. Vissière, O. Company, S. Krut, P. Noire, T. Roux and F. Pierrot, *Application-oriented selection of poses and forces for robot elastostatic calibration*, Mechanism and Machine Theory.(*under review*)

Abstract

Hexapods are increasingly being used for high-precision 6-DOF positioning applications such as for positioning mirrors in telescopes and for positioning samples in synchrotrons. These robots are designed and controlled to be very repeatable and accurate. However, structural compliance of these positioning systems limits their positioning accuracy. As accuracy requirements become more stringent in emerging applications, compensating for inaccuracy due to structural compliance becomes necessary.

In this regard, firstly, a method for elastostatic calibration of hexapods is presented. This method uses a lumped stiffness parameter model to parametrize the relationship between the platform deflections and the force/moment applied on it. These parameters can be estimated using deflection measurements performed using known forces/moments applied on the platform. The estimated parameters can then be used to predict and correct hexapod's positioning errors due to compliance.

Secondly, a new approach is presented to optimize stiffness identification for robot elastostatic calibration. In this, a framework is proposed to formulate criteria to choose best set of poses and forces for stiffness identification experiment. The parameters identified under experimental conditions (poses and forces) suggested by these criteria ensure minimum impact of errors influencing stiffness identification (uncertainty of deflection measurements and errors in forces applied) on compensation quality. Additionally, it also maximizes accuracy after compensation at desired pose(s), along desired axe(s) of the platform and with desired forces/moments on the platform. This stiffness identification optimization framework ensures best compensation for positioning errors due to compliance as per the positioning requirements of the application at hand.

Lastly, a method is presented to eliminate the influence of thermal deflection of a hexapod on the measured 6-DOF pose of its platform. This method is necessary when thermal deflections of the hexapod are large enough to impact results of a study, which was the case with some tests performed to validate methods developed in this thesis.

The efficacy of presented methods have been validated by means of simulation studies on a bipod and experimental studies on a high-precision hexapod positioning system.

Keywords: *hexapod, elastostatic calibration, stiffness identification, parameter identification, design of experiments, observability index, pose measurement*

Résumé

Les hexapodes sont de plus en plus utilisés pour des applications de positionnement de haute précision à 6 degrés de liberté, comme pour le positionnement des miroirs des télescopes ou pour le positionnement des échantillons dans les synchrotrons. Ces robots sont conçus et commandés pour faire preuve de grande répétabilité et de grande justesse. Cependant, la souplesse structurelle de ces systèmes de positionnement limite leur précision de positionnement. Comme les exigences de précision deviennent de plus en plus strictes dans les applications émergentes, il devient nécessaire de compenser ces déformations.

À cet égard, tout d'abord, une méthode d'étalonnage élastostatique des hexapodes est présentée. Cette méthode utilise un modèle de paramètre de rigidité forfaitaire pour paramétrer la relation entre les flèches de la plate-forme et la force / le moment qui lui est appliqué. Ces paramètres peuvent être estimés à l'aide de mesures de déflexion effectuées en utilisant des forces / moments connus appliqués sur la plate-forme. Les paramètres estimés peuvent ensuite être utilisés pour prévoir et corriger les erreurs de positionnement des hexapodes dues à la conformité.

Deuxièmement, une nouvelle approche est présentée pour optimiser le processus d'identification des paramètres de raideur de l'étalonnage élastostatique. Cette approche repose sur l'utilisation de critères qui permettent de déterminer le meilleur ensemble de poses et de forces pour identifier les paramètres de raideur. Les paramètres identifiés dans les conditions expérimentales (poses et forces) suggérées par ces critères permettent une contribution minimum des erreurs influençant l'identification des raideurs (incertitude des mesures des déflections et erreurs des forces appliquées) sur la qualité de la compensation. De plus, suivre cette approche maximise également la précision après compensation aux poses souhaitées, le long des axes souhaités, et avec les combinaisons force/moment souhaitées sur la plateforme. Ce cadre d'optimisation pour l'identification des raideurs assure la meilleure compensation des erreurs de positionnement dues à la souplesse structurelle, selon les exigences de positionnement de l'application en question.

Enfin, une méthode est présentée qui permet de s'affranchir des effets dues à la thermique sur la mesure des 6 degrés de liberté de la pose de la plateforme d'un hexapode. Cette méthode est nécessaire lorsque les déflections dues à la thermique de l'hexapode sont suffi-

samment importantes pour avoir un impact sur les résultats d'une étude, ce qui était le cas avec certains des tests effectués pour valider les méthodes développées dans cette thèse. L'efficacité des méthodes présentées a été validée au moyen d'études en simulation sur un bipède, et d'études expérimentales sur un système de positionnement hexapode de haute précision.

Mots clefs : *hexapode, étalonnage élastostatique, identification de la rigidité, identification des paramètres, plan expérience, indice d'observabilité, mesure de la pose*

LIRMM — 161, rue Ada — 34095 Montpellier cedex 5 — France